Advanced Casting Research Center (ACRC) Consortium Meeting

May 15, 2001

Report 01 - #1

METAL PROCESSING INSTITUTE
WPI, Worcester, MA 01609 USA
www.wpi.edu/+mpi

EXECUTIVE SUMMARY OF MATH MODELING ACTIVITIES (A.ALEXANDROU)

Mathematical modeling and simulations of semisolid filling processes remains a critical issue in understanding and optimizing the process. Semisolid slurries are non-Newtonian materials that exhibit complex rheological behavior. Therefore, the way these slurries flow in cavities is very different from the way liquid in classical casting fills cavities. Actually filling in semisolid processing is often counterintuitive.

The modeling work of the semisolid consortium is focused on three distinct areas as described below:

1. The understanding of the SSM rheology from a fundamental point of view and the mathematical description of the observed macroscopic constitutive behavior. Current understanding of the rheology of SSM suspensions indicates that the slurries are characterized by a finite yield stress, and by material properties that are time and shear rate dependent. Mathematically, the observed behavior fits well a generalized time-dependent Herschel-Bulkley fluid model. Computationally the model was modified from the ideal Herschel-Bulkley model to avoid the mathematical singularity inherent in the original model. The theory we developed has been incorporated into a number of two- and three-dimensional computer codes.

2. The understanding and a mapping of flow instabilities distinct to semisolid processing. During filling semisolid slurries exhibit flow behaviors not observed in liquid casting. For instance, semisolid slurries fill cavities in a preferential way i.e. filling in one direction may halt while filling proceeds in other parts of the cavity. Due to the unique rheology of semisolid suspensions and depending on the slurry properties dies fill in very distinct patterns. Also, due to flow instabilities during filling, final parts are found to have unacceptable variability in their mechanical properties. This of course increases the scrap rate, and consequently the cost of the process. The dominant instability responsible for this variability in the properties in known as the "toothpaste instability."

   In our modeling we managed to reproduce the above mentioned behaviors. In the case of preferential filling, we concluded that the behavior is due to the finite yield stress of the slurry. The same is true for the distinct filling patterns obtained in the filling of simple cavities. In our work we identified five patterns with which SSM slurries may fill a simple two-dimensional cavity: (i) shell, (ii) disc, (iii) mound, (iv) bubble and (v) transition pattern-- a pattern between that of the disc and the bubble filling patterns.

The toothpaste instability is due to fluid column buckling. This behavior is likely to happen at distinct combinations of the Reynolds and Bingham numbers. In our work we identified the parameter space where unstable behavior is more likely to occur in a simple rectangular two-dimensional cavity. We concluded that the most unstable pattern is that of bubble, and to a lesser degree that of the transition pattern.

3. The simulation of filling o real parts. In parallel to tasks (a) and (b), we initiated a number of simulation studies to simulate filling of real die cavities used by our industrial partners to produce real parts. The simulations were performed using the simulation package PAM-CAST offered for consortium use by ESI and Pechiney aluminum company. The simulation packaged was modified to include the Herschel-Bulkley flow behavior.

The attached paper gives the processing map which is needed to avoid instabilities. This emanated from Philippe Le Menn's Master Thesis and Dr. Pan's work on yield stress measurements.

TABLE OF CONTENTS

A. Modeling of Rheology in Semi-Solid Alloys

On the Reliability of the Semisolid Metal Processing: Effects of the Yield Stress

Andreas N. Alexandrou[a,1], Philippe Le Menn[a], Diran Apelian[a], Quinyue Pan[a] and George C. Georgiou[b]

[a] *Advanced Casting Research Center (ACRC), Worcester Polytechnic Institute Worcester, MA 01609, USA*

[b] *Department of Mathematics, University of Cyprus CY 1618, Nicosia, Cyprus*

Abstract

The purpose of this work is to address lingering concerns about the reliability of the semisolid metal process (SSMP) and its inability to produce consistently high quality parts. In this paper we provide evidence of experimental results that are typical of those that lead to questions about the consistency of the process. While the rheology of SSM suspensions is not fully understood, we demonstrate that the inconsistent results can be explained by considering the finite yield stress of the slurries. This implies that by controlling the process parameters the instabilities can be avoided. We also provide stability maps to indicate the parameter space where unstable behavior is more likely to occur in a simple rectangular 2-D cavity.

1 Introduction

Traditionally, metal alloys are cast in their fully liquid state using processes such as sand casting, high pressure casting or squeeze casting. Sand

[1] Corresponding author. Currently at the Department of Mechanical Engineering, University of Cyprus, Nicosia, Cyprus.

casting produces parts with large dimensional tolerances that require extra-machining; moreover, due to porosity caused by air entrapment, they have inferior strength. High-pressure casting significantly reduces porosity, allowing the production of much thinner parts. However, the low ductility of the final products remains an important handicap. Squeeze casting is designed to operate at higher-than-usual pressures. The increased pressure reduces porosity, but the process is hampered by tool wear and manufacturing costs.

Shaping aluminum alloys in the semisolid state by thixoforming produces complex parts with better metallurgical quality when compared to parts produced by the aforementioned liquid casting methods. Thixoformed parts can have thinner sections than in squeeze casting and have mechanical properties independent of the local cooling rate [1]. In contrast to liquid casting, in semisolid metal casting the material is processed from a slurry kept at a temperature between the solidus and the liquidus isotherms. Therefore, it can be applied only to materials that have a wide solidification range. Since pure aluminum and eutectic alloys solidify at a single temperature, they are not suitable for semisolid processing. Non-eutectic alloys, however, over a given range of temperature and composition are thermodynamically stable in the semisolid state, which makes them suitable for the process. Since SSMP combines the advantages of both liquid metal casting and solid metal forging, it is gaining interest very rapidly within the casting industry.

Thixoforming of aluminum alloys is fast and allows for high production rates with enhanced mechanical properties. Therefore, the automotive, aircraft and aerospace industries represent a large market for this technology [2]. The automotive industry already makes use of thixoforming for a number of different components that require a high degree of tightness such as fuel rails [3], master brake cylinders [4], ABS bodies and air-conditioner compressor housings. Other examples include high-strength parts such as engine mounts, knuckles, suspension components, wheels, and wear-resistant parts requiring hyper-eutectic alloys, such as unanodized master cylinders, brake drums and gearshift forks [5]. These examples show that thixoformed parts are attractive replacements for permanent mold or forged aluminum components, as well as substitutions for cast iron parts, in which weight saving is especially important [6].

However, despite the attractive features of the process, its implementation to industrial applications is hampered by technical issues. One outstanding

problem that limits the spread of the process is the fact that many casters report significant scrap rates associated with problems in filling. These rates are often high enough to label the process as unpredictable. While there are still many unresolved technical issues related to the semisolid process, it is the belief of the authors that many problems associated with filling can be explained by considering properly the complex rheology of the slurries. The main objective of this paper then is to address concerns about the reproducibility of the results in semisolid processing. This is achieved through numerical simulations by considering the basic rheology of the slurries.

Figure 1 shows three filling patterns obtained experimentally by Paradies and Rappaz [7] for semisolid aluminum alloy A356 filling a simple cavity. Filling patterns were obtained by interrupting metal injection during die filling. These three filling profiles, respectively named "mound" (a), "disk" (b) and "shell" (c), were obtained for slightly different process conditions. This is a clear demonstration that filling can be significantly different when process conditions change, even by a small amount. Interestingly, this behavior is not restricted to semisolid materials. Experimental results obtained by Koke et al. [8] show that filling a die with substances such as chocolate cream, calcium-carbonate/oil suspension, tomato paste, ultrasonic gel and Newtonian silicone oil lead to similar flow patterns. As a matter of fact, these model substances have a rheology similar to semisolid alloys which shows that semisolid slurry behavior is not unique and, hence, can be presented by some general framework. Typical "shell' and "mound" patterns were obtained and are shown in Fig. 2. The three aforementioned flow patterns ("mound," "disk" and "shell") have been clearly identified and observed for both Newtonian fluids and semisolid materials. In a recent experimental study, Midson et al. [9] filled a rectangular plate shaped cavity with semisolid aluminum alloy A357. For given geometrical dimensions and process parameters, a very unique filling behavior has been observed, as shown in Fig. 3. Quite clearly, the metal (injected from the left) appears to initially flow down the center of the die. The main filling then proceeds from the entrance of the cavity as a growing bubble. This flow pattern strengthens the idea that filling in semisolid processing may be very counterintuitive.

Other experimental observations [10] clearly established the importance of controlling parameters such as inlet velocity, temperature (i.e., viscosity and yield stress of the material) and geometrical dimensions of the die. Figure

4 shows an experimental observation of the "toothpaste" behavior which is a typical fluid instability observed in semisolid metal processing during die filling. As shown, even though the part is symmetric, the left arm presents a wavelike instability. A similar irregular filling profile is also shown in Fig. 5. Investigations by Midson et al. [9, 10] provide other illustrations of irregular fillings. Figure 6 shows photographs of the filling progession for castings produced with various gate dimensions. Quite clearly, once the stream of metal hits the end-wall, the remainder of the cavity is filled by the stream bending and folding upon itself. Such unpredictable behaviors are believed to be caused by flow instabilities. The folding provides numerous opportunities for air entrapment and a casting produced under such conditions would most likely have inferior mechanical properties. These experimental observations provide evidence of unpredictable flow behavior. Consequently, the stability of the process for various critical parameters deserves to be qualitatively and quantitatively investigated.

2 Rheology of Semisolid Materials

Typically, the solid fraction for SSMP varies between 0.3 and 0.6. Therefore, the slurry behaves neither as a fully solid material (Hookean solid), nor as a fully liquid material (Newtonian liquid). The semisolid material is considered as a two-phase body composed of a solid porous medium with an interstitial liquid phase. As a solid the semisolid metal maintains its structural integrity, and as a liquid it flows with relative ease. In this state, individual solid particles begin to agglomerate and form a skeleton that can sustain a finite shear stress without deforming. During the injection process the microstruture of the semisolid material is a function of the local temperature and the applied shear rate. Therefore, its rheology varies during processing.

The "yield stress" (τ_o) is a key property of semisolid slurries. Below a finite level of stress, the slurry behaves and reacts as a solid. Above this level, it exhibits flow characteristics and can be described by rheological properties. This minimum shear stress for deformation is known as the yield stress and is a property of the material. In the "core" regions where the local shear stress is below the finite yield stress of the material, the velocity gradient is

essentially zero. Once the yield stress is exceeded, the material behaves as a liquid and is characterized by a non-linear stress-strain relationship.

Whether the yield stress is a true property or an apparent physical quantity has been questioned by several investigators. Barnes and Walters [11] concluded that, given accurate measurements, no yield stress exists but what appears to be so is simply creep. However, this was disputed by Harnett and Hu [12] using a fiber-reinforced polymer material. Currently, the concept of yield stress is generally accepted as a standard term to characterize materials such as semisolid slurries which exhibit this particular behavior.

For semisolid aluminum slurries it is easily understood that the finite yield stress of the material strongly depends on its solid fraction, i.e., on its temperature. At very low solid fractions the yield stress is close to zero and the slurry is mainly liquid. At high solid fractions the yield stress is significant and the material becomes a porous solid that can no longer be considered as a liquid.

Pan and Apelian [13] investigated yielding behavior of commercial semisolid aluminum alloys A356 and 357 fabricated by both magnetohydrodynamic (MHD) and grain-refined (GR) methods. In the study, a plate compression method was used to measure yield stress of semi-solid slurries at high solid fractions (≥ 0.5), while a cone penetration method was used to measure yield stress at intermediate and low solid fractions (< 0.5) [13]. Their results show that the yield stress of aluminum alloys is a strong function of temperature (solid fraction) in the semi-solid state, as shown in Figs. 7 and 8. In the two phase region, with increasing temperature the yield stress decreases dramatically. A significant variation in yield stress was found to occur in the temperature range between $570 - 580°C$ for A356 alloy, and between $570 - 585°C$ for 357 alloy.

Pan and Apelian have also shown [13] that for a given solid fraction, the GR alloy has a higher yield stress than MHD processed alloy in the solid fraction range between 0.5-1. Once the solid fraction is less than 0.5, however, there is no difference in yield stress values between MHD and GR alloys (see Figs. 9 and 10). Their detailed metallographic and image analysis shows that the relatively high yield stress value of GR alloy can be attributed to the entrapped liquid and the shape factor of the primary Al particles, as summarized in Figs. 11 and 12. Compared to the MHD processed alloy, GR

two-phase model is currently available (although some developments are in progress [18, 19, 20]). Consequently, models dealing with the bulk behavior of the material are being used. Although less rigorous, they provide sufficient information for the design of the process.

The most commonly used model is the Bingham model [21, 22, 23]. It is expressed in tensorial form as:

$$\underline{\underline{\dot{\gamma}}} = 0 \quad \text{for} \quad \tau \leq \tau_o, \tag{1}$$

$$\underline{\underline{\tau}} = \left(\eta + \frac{\tau_o}{\dot{\gamma}}\right) \underline{\underline{\dot{\gamma}}} \quad \text{for} \quad \tau > \tau_o, \tag{2}$$

where $\underline{\underline{\dot{\gamma}}} = \left(\nabla \mathbf{u} + \nabla \mathbf{u}^{\mathbf{T}}\right)$ represents the rate of strain tensor, $\underline{\underline{\tau}}$ the extra stress tensor, τ_o the yield stress and η the viscosity of the deformed material. τ and $\dot{\gamma}$ are respectively the second invariants of the extra stress and rate of strain tensors, defined as:

$$\tau = \left[\frac{1}{2}\tau_{ij}\tau_{jk}\right]^{1/2} \quad \text{and} \quad \dot{\gamma} = \left[\frac{1}{2}\dot{\gamma}_{ij}\dot{\gamma}_{jk}\right]^{1/2}. \tag{3}$$

The rheological behavior of a Bingham fluid is characterized by two different flow regimes: if $\tau \leq \tau_o$ the material behaves as a rigid solid. If $\tau \geq \tau_o$ it flows with the apparent viscosity $\eta_{app} = \eta + \frac{\tau_o}{\dot{\gamma}}$.

The Herschel-Bulkley model is a generalization of the Bingham model. It takes into account changes in the effective viscosity with the applied shear rate (shear-thinning and shear-thickening behaviors). The Herschel-Bulkley model assumes the following power-law expression for the effective viscosity of the deformed material:

$$\eta = \kappa \dot{\gamma}^{n-1}, \tag{4}$$

where n and κ are the power-law and consistency indices, respectively. The fluid behavior is shear-thickening for $n > 1$ and shear-thinning for $n < 1$. For $n = 1$ the Herschel-Bulkley model reduces to the Bingham model with the consistency index equivalent to the viscosity.

The yielded ($\tau > \tau_o$) and unyielded ($\tau < \tau_o$) regions of the fluid are separated by the "yield surface" defined as the surface where the local stress

is equal to the yield stress. In numerical modeling, in addition to the non-linearities in the governing equations, an inherent difficulty is the discontinuity in the constitutive relation. Due to the presence of $\dot{\gamma}$ in the denominator of Eq. (2), the apparent viscosity becomes unbounded at vanishing shear rates. Also, while calculating the velocity field the shape and location of the yield surface are unknown. Although this does not constitute any limitation in analytic solutions in simple cases such as flow in tubes [24], it introduces significant difficulties in more complicated problems that are only amenable to numerical analysis. To overcome these issues, several modified versions of Eqs. (1) and (2) have been proposed [25, 26, 27, 28]. A common approach is to approximate the rheological behavior of the fluid to be valid uniformly at all levels of stress. Papanastasiou [25] introduced a regularization parameter m that controls the exponential rise in the stress at low rates of strain:

$$\underline{\underline{\tau}} = \left[\eta + \tau_\circ \frac{1 - exp\,(-m\dot{\gamma})}{\dot{\gamma}}\right] \underline{\underline{\dot{\gamma}}}. \tag{5}$$

The parameter m has dimensions of time. This constitutive relation is expressed in terms of three independent material parameters, τ_o, κ, and n, which are determined from experimental data. The Herschel-Bulkley behavior is approximated for relatively large m values. According to Eq. (5), for $\dot{\gamma} \approx 0$ the apparent viscosity is finite and given by $\eta_{app} \approx (\eta + m\tau_o)$. The constitutive relation is then expressed as $\underline{\underline{\tau}} \approx (\eta + m\tau_o)\underline{\underline{\dot{\gamma}}}$. Papanastasiou [25] validated this model on several simple flows such as one-dimensional channel flow, two-dimensional boundary layer flow and extrusion flow. The accuracy and effectiveness of this model in studying Herschel-Bulkley fluids has also been demonstrated by Elwood et al. [29], Mitsoulis and Abdali [30], Tsamopoulos et al. [31], Blackery and Mitsoulis [32] and Burgos et al. [28, 33].

4 Mathematical and Computational Model

The schematic of the problem considered here is shown in Fig. 14. The 2-D geometry is characterized by the inlet section (length l and height H). The material is injected in the die from the left side and hits the vertical solid surface at a distance L away.

The flow was modeled using the conservation of mass and momentum for an incompressible fluid. The set of governing equations were non-dimensionalized using:

$$x_i^* = \frac{x_i}{H};\ \ t^* = \frac{t}{H/U_o};\ \ \mathbf{u}^* = \frac{\mathbf{u}}{U_o};\ \ P^* = \frac{P}{\tau_o};\ \ \underline{\underline{\tau}}^* = \frac{1}{\tau_o}\underline{\underline{\tau}};\ \ \underline{\underline{\sigma}}^* = \frac{1}{\tau_o}\underline{\underline{\sigma}}, \tag{6}$$

where H is taken as the inlet height and U_o the average inlet velocity. Due to the non-dimensionalization the imposed volumetric flow rate is $Q^* = 1$.

Using the dimensionless groups introduced in Eq. (6) we can rewrite the governing equations in a dimensionless form:

$$\nabla \cdot \mathbf{u}^* = 0, \tag{7}$$

$$Re\left[\frac{\partial \mathbf{u}^*}{\partial t^*} + \mathbf{u}^* \cdot \nabla \mathbf{u}^*\right] = Bi \nabla \cdot \underline{\underline{\sigma}}^*. \tag{8}$$

Here, $\underline{\underline{\sigma}}^* = -P^*\underline{\underline{I}} + \underline{\underline{\tau}}^*$, is the total non-dimensional stress tensor. According to Eqs. (7) and (8) the fluid behavior depends on two dimensionless parameters, the Reynolds (Re) and Bingham (Bi) numbers, defined respectively as:

$$Re = \frac{\rho U_o H}{\eta_{eff}} \quad and \quad Bi = \frac{\tau_o H}{\eta_{eff} U_o}. \tag{9}$$

The effective viscosity η_{eff} is obtained from the one-dimensional analog of the constitutive equation (Eq. (5)):

$$\tau = \tau_o + \kappa \dot{\gamma}^n = \tau_o + \kappa \mid \dot{\gamma} \mid^{n-1} \dot{\gamma}, \tag{10}$$

where $\dot{\gamma}$ is the shear rate, and $\eta_{eff} = \kappa \mid \dot{\gamma} \mid^{n-1}$ is the effective viscosity.

Therefore, the Reynolds and Bingham numbers are generalized as:

$$Re = \frac{\rho U_o^{(2-n)} H^n}{\kappa}, \quad and \quad Bi = \frac{\tau_o H^n}{\kappa U_o^n}. \tag{11}$$

The Herschel-Bulkley constitutive relation (Eq. (5)) can thus be rewritten in a dimensionless form:

$$\underline{\underline{\tau}}^* = \left[\frac{1}{Bi}\dot{\gamma}^{*(n-1)} + \frac{[1 - exp\,(-m^*\dot{\gamma}^*)]}{\dot{\gamma}^*}\right]\underline{\underline{\dot{\gamma}}}^*, \tag{12}$$

where $\underline{\underline{\dot{\gamma}}}^*$ is the dimensionless rate of strain tensor, $\dot{\gamma}^*$ its second invariant, and m^* the dimensionless growth exponent, which are respectively defined as

$$\underline{\underline{\dot{\gamma}}}^* = \frac{1}{U_o/H}\underline{\underline{\dot{\gamma}}} \quad \dot{\gamma}^* = \frac{\dot{\gamma}}{(U_o/H)^2} \quad m^* = \frac{mU_o}{H}. \tag{13}$$

Equation (12) has only two independent material parameters (Bi and n), whereas Eq. (5) had three (κ, τ_o, and n).

The governing equations and constitutive relation were discretized using the classical mixed-Galerkin finite element method with nine-node rectangular elements. The resulting non-linear system of equations was linearized using a Newton-Raphson iteration procedure. For converged results in the Newton-Raphson iterative scheme, usually three to four iterations were necessary at each time step. More details can be found on the method of solution in [34, 35].

5 Results

In this section we examine semisolid filling behavior in a simple 2-D cavity (or an equivalent flow arrangement). As shown below, the filling patterns and flow instabilities observed experimentally can be reproduced using the most basic characteristic of the slurry rheology, i.e., the finite yield stress.

In a recent study, Alexandrou et al. [36] investigated filling of a 2-D cavity by Bingham fluids using the simulation package PAM-CAST/Simulor by examining the relative importance of inertial, viscous and yield stress effects on the filling profiles. They identified not only the filling patterns shown in Fig. 1, but also a pattern identified as "bubble", as well as a "transition" pattern between that of "mound" and "bubble" patterns. These numerical results were obtained using a finite-volume code and a fixed mesh. For the purpose of the present study, we simulated the cases considered in [36] using finite-element simulations along with a moving mesh scheme. In this case, the simulations can be classified as "exact" since the mesh follows the motion of the fluid and the boundary conditions are applied exactly. Figure 15 shows the results for similar conditions as in [36]. The five typical flow behaviors reported by Alexandrou et al. have been reproduced here as well, providing thus further evidence on the existence of these patterns.

It is postulated that the inconsistent filling of SSM slurries is the result of flow instabilities during processing. A common defect observed in SSM processing is a behavior known as toothpaste (Figs. 4 and 5). The name "toothpaste" comes from the similarity between this instability and the toothpaste behavior when forced out of its tube. When reaching the end-wall, the jet bends due to local increase in pressure. From a practical point of view such instabilities are undesirable and can lead to non-uniformities in the final component. This of course increases the scrap rate and consequently the cost of the process. Analysis of experimental results clearly demonstrates that the way semisolid materials fill a cavity is strongly dependent on the flow conditions and rheological parameters [9, 10]. Therefore there is a need to control the influence of these parameters on the stability of the injection process. Uncontrolled filling would indeed result in an important amount of folding and inferior mechanical properties. Moreover, the toothpaste instability is believed to be caused by fluid column buckling which is a direct consequence of the yield stress effect. Therefore, this behavior needs to be documented.

In this work, we concentrate on the interaction of a Herschel-Bulkley fluid jet and a vertical surface at a distance L from the die exit and we study the interplay between inertia, viscous drag and yield stress, or as expressed in terms of force per unit depth, $F_i \equiv \rho U_o^2 H$, $F_v \equiv \eta U_o$, and $F_{\tau_o} \equiv \tau_o H$ respectively. This problem reproduces the filling at the early stages when the filling front first reaches the closed-end of the die. Non-dimensional analysis shows that the flow depends on two dimensionless parameters: the Reynolds (Re) and Bingham (Bi) numbers.

In numerical simulations, flows that in real life are stable, may fail to reveal instabilities. This is due to the almost perfect symmetry of the numerical flow field and the fact that numerical errors take a long time to initiate instabilities. Therefore, it is customary to introduce an artificial disturbance in the flow to disrupt its symmetry. This artificial instability is typically small and it is applied for a short duration. Here, a small disturbance is introduced in the flow by imposing an asymmetric velocity profile at the inlet for a short time Δt, beginning at the moment (defined as $t = 0$ in the following) the jet of fluid reaches the vertical wall. For $t > \Delta t$, the inlet velocity was kept constant and symmetric. In both the symmetric and asymmetric cases the volumetric flow rate was kept constant. The flow field and the jet stability are found to be independent of the magnitude and the duration of the

asymmetry.

The finite-element mesh used in the simulations is refined around zones which are sensitive to flow singularities (die exit and end-wall). The power-law index n and parameter m are fixed at values $n = 1$ and $m = 1000$ (Bingham case). The unsteady simulation begins at the time where the jet hits the vertical wall ($t = 0$). The initial conditions were taken from the steady solution of the problem for the configuration when the jet is about to touch the wall. The geometry we used includes an inlet section ($H = 1$, $l = 5$), and a vertical wall at a distance L from the exit of the die. The results shown are for variable values of L. Typical jet-wall interactions are shown in Figs. 16 and 17, as sequences of 'snapshots' of the jet profile, where t is the non-dimensional time.

Figure 16 shows the jet behavior for the $L = 10$ geometry at a low Reynolds number, $Re = 1$, and a moderate Bingham number, $Bi = 3$. For a symmetric velocity profile at the inlet (i.e., no disturbance), these conditions lead to a "bubble" pattern. Here, when the jet emanating from the inlet section reaches the vertical wall, it grows as a "bubble" pattern up to a dimensionless time $t \approx 7$. When the disturbance is introduced from the start of the flow ($t = 0$) until $t = \Delta t = 1.5$, it triggers an instability which forces the jet to bend, very much like the buckling of a slender solid column. The fluid starts to flow sideways leading to an unstable jet profile. This flow behavior is very similar to what is observed experimentally and described as the toothpaste effect.

The flow shown in Fig. 17 is obtained for $Re = 5$ and $Bi = 1$. For both symmetric and asymmetric flow conditions the jet grows in a manner consistent with a transition pattern. Therefore, the initial disturbance has no impact on the stability of the jet, and no noticeable difference can be observed between the symmetric and asymmetric cases.

A complete map of the jet profiles as a function of the Reynolds and Bingham numbers was developed in the range $0.5 \leq Re \leq 50$, $0 < Bi \leq 40$. The map presented in Fig. 18 clearly shows the regions where "stable" and "unstable" patterns occur. The estimated boundary between these two zones has been sketched in in order to demarcate the range of Re and Bi which they correspond to. On this map, the symbols ▲, •, ■, ▼ represent respectively the "mound," "disk," "bubble" and "transition" patterns. The

hollow symbols ($\square$, and $\triangledown$) represent the cases discussed in detail (Figs. 16 and 17). The estimated boundary between stable and unstable behaviors has been sketched in. As speculated, while "bubble" pattern leads to unstable jet behavior, "shell," "disk" and "mound" patterns remain stable. Most of the "transition" cases lead to stable jet profiles. These numerical results explain why experimental observations of the "bubble" pattern are not common, as the pattern is very sensitive to flow instabilities.

So far the length L was kept constant. However, the stability characteristics depend also on the length of the die L. The effect of the distance between the die exit and the vertical wall was studied using three different lengths $L = 10$, 15 and 20. The map shown in Fig. 19 summarizes these results. The solid line represents the $L = 10$ case while the dashed line and the dashdotted line stand for the $L = 15$ and $L = 20$ cases, respectively. From that figure, the overall jet stability is confirmed: the longer L, the more likely it is to observe toothpaste-like instabilities.

Experimental observations by Midson et al. [9] are a good illustration on the way the maps developed in this study could be used to control process parameters. Figure 6 shows a photograph of a series of castings (A357) produced when filling a rectangular cavity (150 mm long, 100 mm wide and 9 mm thick) through a 19 mm by 9 mm gate. This gives a ratio $L/H = 7.5 \approx 10$. The metal appears to initially flow down the center of the die to the top of the cavity, before it starts to flow sideways. Folds can be clearly observed in some of the castings. The process conditions and geometrical parameters make these castings fall into the unstable regions of the stability maps shown in Fig. 18. So as to obtain a stable filling, process parameters have to be modified. Considering the stability map and the definition for the Reynolds and Bingham numbers, a solution would be to change the gate velocity U_o. Starting from a state in the unstable region, we increase U_o. This will increase Re and reduce Bi. On the map, this will move our process state in diagonal toward the bottom right of the map, i.e., within the stable region. Another possibility is to modify the temperature of the slurry. As demonstrated earlier, the viscosity and the yield stress are functions of the material temperature. Therefore, by controlling the temperature parameter, we are able to control the Reynolds and Bingham numbers and to shift the process state within the stable region.

6 Conclusions

Due to the unique rheology of semisolid suspensions and depending on the slurry properties, dies fill in very distinct ways. Eventually, the various filling patterns have direct implications on the quality and mechanical properties of the produced parts. In this study, we presented numerical simulations and experimental measurements that highlight the significant role of the finite yield stress in semisolid metal processing. The simulations confirm experimentally observed flow patterns in filling of simple cavities. This paper also addresses concerns about the reproducibility of the process. In actual SSMP, filling patterns are often irregular and unpredictable, pointing to the existence of flow instabilities. The yield stress of semisolid metals is believed to be responsible for these instabilities. In this study, stability maps are drawn as a function of the process parameters in filling of 2-D cavities. The results highlight the way process parameters should be controlled in order to obtain high quality castings.

References

[1] Loué W. R., Brimont M., Pluchon C., Menet P. Y., and Garat M. Metallurgical aspects of thixoforming of A356.0 and 357.0 alloys. In *Conference Proceedings: North American Die Casting Association*, Indianapolis, IN, October 2-5 1995.

[2] Duc E. Die filling of Bingham fluids. Master's thesis, Worcester Polytechnic Institute, Worcester, MA, 1999.

[3] Moschini R. Mass production of fuel rails by pressure die casting in the semi-liquid state. In *Proceedings 3rd International Conference on Semisolid Processing of Alloys and Composites*, Tokyo, Japan, June 1994.

[4] Kenney M. P., Courtois J. A., Evans R. D., Farrior G. M., Kyonka C. P., Koch A. A. and Young K. P. *Metals Handbook*, volume 15-Casting. ASM, 1989.

[5] Loué W. R., and Garat M. Recent industrial developments in the field of thixocasting. Technical report, Aluminium Pechiney, Casting Alloys Division, Voreppe, France, 1997.

[6] Young K. P. and Fitze R. Semisolid metal cast aluminium automotive components. In *Proceedings 3rd International Conference on Semisolid Processing of Alloys and Composites*, Tokyo, Japan, June 1994.

[7] Paradies C. J. and Rappaz M. Modeling the rheology of semisolid metal alloys during die casting. In *Modeling of Casting, Welding and Advanced Solidification Processes VIII. Proceedings of the 8th International Conference on Modeling of Casting and Welding Processes*, pages 933–940, San Diego, CA, June 7-12 1998. The Minerals, Metals and Materials Society, Edited by Thomas B. G. and Beckermann C.

[8] Koke J., Modigell M., Hufschmidt M., and Alexandrou A. A study on the die filling behavior with semisolid fluids. In *6th International Conference on Semisolid Processing of Alloys and Composites, Conference Proceedings*, pages 635–639, Turin, Italy, 27-29 September 2000.

[9] Midson S. P., Minkler R. B., and Brucher H. B. Gating of semisolid aluminum castings. In *6th International Conference on Semisolid Processing of Alloys and Composites, Conference Proceedings*, pages 67–71, Turin, Italy, 27-29 September 2000.

[10] Midson S. P., Thornhill L. E., and Young K. P. Influence of key process parameters on the quality of semisolid metal cast aluminum components. In *5th International Conference on Semisolid Processing of Alloys and Composites, Conference Proceedings*, pages 181–188, Golden, CO, 23-25 June 1998.

[11] Barnes H. A., and Walters K. The yield stress myth? *Rheologica Acta*, 24:323–326, 1985.

[12] Hartnett J. P. and Hu R. Y. Z. Technical note: the yield stress - An engineering reality. *Journal of Rheology*, 33:671–679, 1989.

[13] Pan Q. Y., Apelian D. Yield stress of commercial Al alloys in the semisolid state. *Metall. & Mater. Trans. B*, to be submitted.

[14] Joly P. A. and Mehrabian R. The rheology of a partially solid alloy. *Journal of Material Science*, 11:1393–1418, 1976.

[15] Kattamis T. Z. and Picone T. J. Rheology of semisolid Al-4.5%Cu-1.5%Mg alloy. *Materials Science and Engineering*, A131:265–272, 1991.

[16] Brown S., Kumar P., and Martin C. L. Shear rate thickening behavior of semisolid slurries. *Metallurgical Transactions*, 24:1107–1116, 1993.

[17] Burgos G. R., Alexandrou A. N., and Entov V. M. Time-dependent rheology of semisolid metal suspensions. In *Synthesis of Light Metals III, Proceedings of the Symposium Sponsored by the LMD and SMD Divisions of the TMS*, San Diego, CA, February 28-March 4 1999. Edited by Froes F. H., Ward-Close C. M., McCormick P. G., and Eliezer D. Also published in Light Metals 1999, Proceedings of the technical sessions presented by the TMS Aluminum Committee at the 128th TMS Annual Meeting, San Diego, CA, February 28-March 4, 1999, Edited by Eckert C. E.

[18] Suéry M., Martin C. L., and Salvo L. Overview of the rheological behavior of globular and dendritic slurries. In *4th International Conference on Semi-Solid Processing of Alloys and Composites, Conference Proceedings*, pages 21–29, Sheffield, England, 19-21 June 1996.

[19] Zavaliangos A., Tzimas E., Lawley A., and Pumpberger C. Physical mechanisms of the flow resistance of semisolid materials at high volume fraction of solid. In *4th International Conference on Semisolid Processing of Alloys and Composites, Conference Proceedings*, pages 40–46, Sheffield, England, 19-21 June 1996.

[20] Alexandrou A.N. and Entov V. Two-phase macroscopic model for semisolid material processing. *Metallurgical Transactions*. To be submitted.

[21] Bingham E. C. *Fluidity and Plasticity*. McGraw-Hill, 1922.

[22] Oldroyd J. G. A rational formulation of the equations of plastic flow for a Bingham solid. *Proceedings of the Cambridge Philosophical Society*, 43:100–105, 1947.

[23] Bird R. B., Dai G. C., and Yarusso B. J. The rheology and flow of viscoplastic materials. *Rev. Chemical Engineering*, 1:1–70, 1983.

[24] Bird R. B. and Armstrong R. C. *Dynamics of polymeric liquids.* John Wiley and Sons, New-York, NY, 1977.

[25] Papanastasiou T. C. Flows of materials with yield. *Journal of Rheology*, 31:385–404, 1987.

[26] Bercovier M. and Engelman M. A finite element method for incompressible non-Newtonian flows. *Journal of Computational Physics*, 36:313–326, 1980.

[27] O'Donovan E. J. and Tanner, R. I. Numerical study of the Bingham squeeze film problem. *Journal of Non-Newtonian Fluid Mechanics*, 15:75–83, 1984.

[28] Burgos G. R., Alexandrou A. N., and Entov V. On the determination of yield surfaces in Herschel-Bulkley fluids. *Journal of Rheology*, 43:463–483, 1999.

[29] Ellwood K. R. J., Georgiou G. C., Papanastasiou T. C., and Wilkes J. O. Laminar jets of Bingham-plastic liquids. *Journal of Rheology*, 34:787–811, 1990.

[30] Mitsoulis E., Abdali S. S., and Markatos N. C. Flow simulation of Herschel-Bulkley fluids through extrusion dies. *The Canadian Journal of Chemical Engineering*, 71:147–160, 1993.

[31] Tsamopoulos J. A., Chen M. F., and Borkar A. V. On the spin coating of viscoplastic fluids. *Rheologica Acta*, 35:597–615, 1996.

[32] Blackery J. and Mitsoulis E. Creeping motion of a sphere in tubes filled with a Bingham plastic material. *Journal of Non-Newtonian Fluid Mechanics*, 70:59–77, 1997.

[33] Burgos G. R. and Alexandrou A. N. Flow development of Herschel-Bulkley fluids in a sudden 3-D square expansion. *Journal of Rheology*, 43:485–498, 1999.

[34] Le Menn P.. Flow instabilities in Herschel-Bulkley fluids. Master's thesis, Worcester Polytechnic Institute, Worcester, MA, 2000.

[35] Alexandrou A. N., Le Menn P., Entov V. and Georgiou G. C. Flow instabilities in Herschel-Bulkley fluids. *Journal of Non-Newtonian Fluid Mechanics*, under review.

[36] Alexandrou A. N., Duc E., and Entov V. Inertial, viscous and yield stress effects in Bingham fluid filling of a 2-D cavity. *Journal of Non-Newtonian Fluid Mechanics*, 96:383–403, 2001.

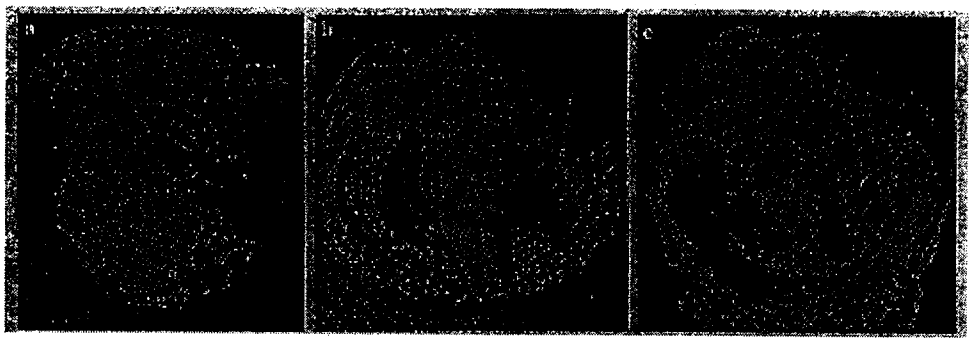

Figure 1: Photographs of the metal removed from the reservoir following experiments on a die with a 20 mm tube diameter, in order of increasing velocity (a) mound and disk, (b) disk and (c) disk & shell [7].

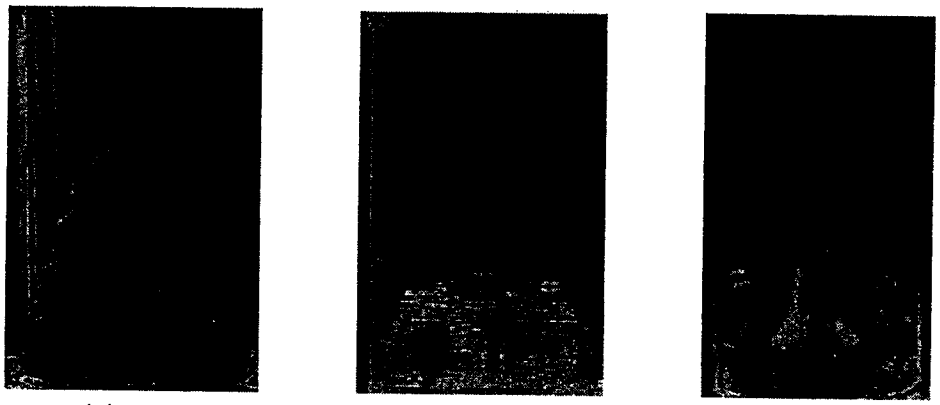

(a) (b) (c)

Figure 2: Experimental results on die filling for (a) Nutella ($Re = 6.51$, $Bi = 0.00311$), (b) ultrasonic gel ($Re = 158$, $Bi = 0.0377$) and (c) $\eta = 12.5$ Pa.s silicone oil ($Re = 3.19$, $Bi = 0$) [8].

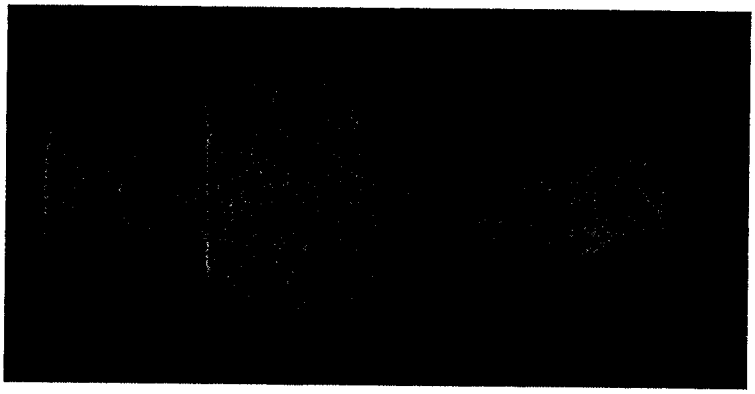

Figure 3: Experimental observation of a "bubble" pattern [9]. A rectangular plate shaped cavity is filled with semisolid aluminum alloy.

Figure 4: Toothpaste behavior (Courtesy of Aluminium Pechiney).

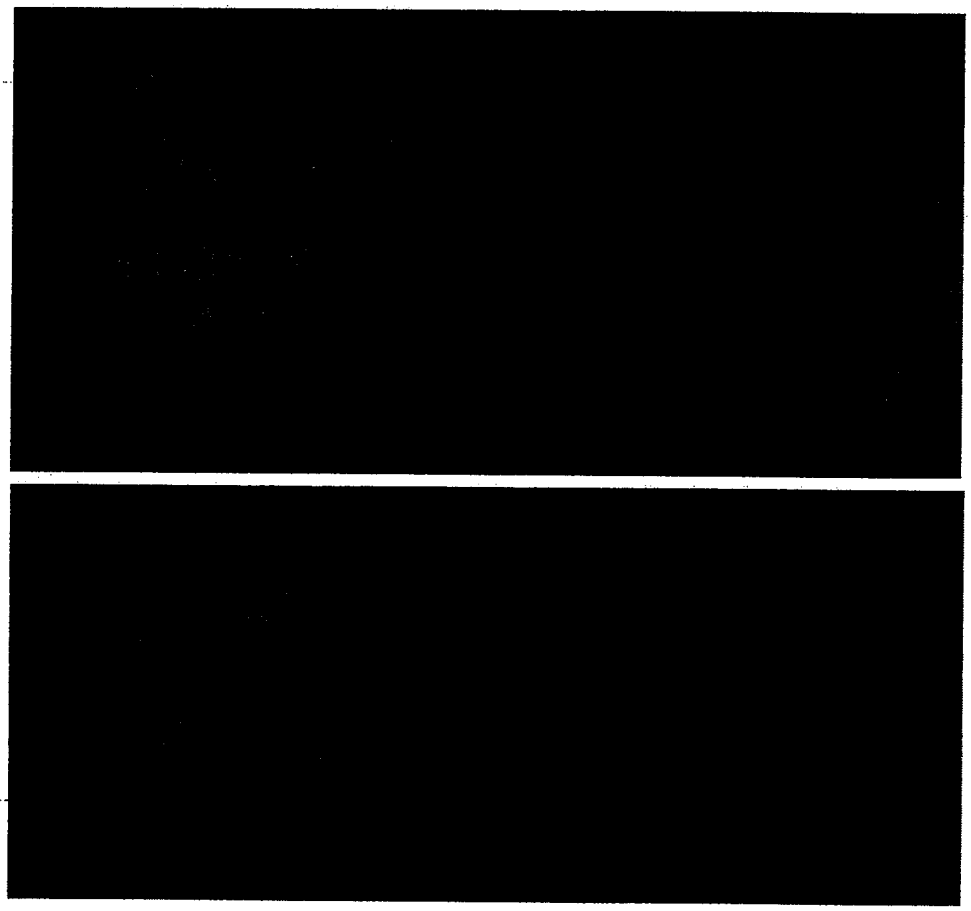

Figure 5: Toothpaste behavior (Courtesy of Aluminium Pechiney).

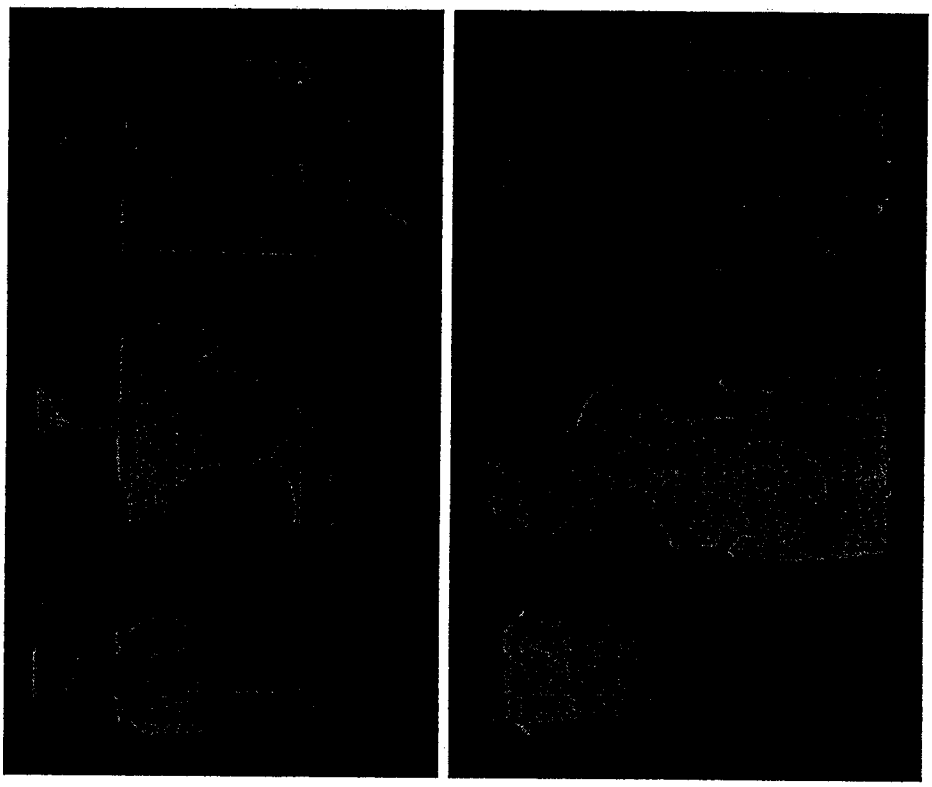

(a) (b)

Figure 6: Photographs of a series of castings made with (a) a 19 mm by 9 mm gate and (b) a 50 mm by 4.5 mm gate [9].

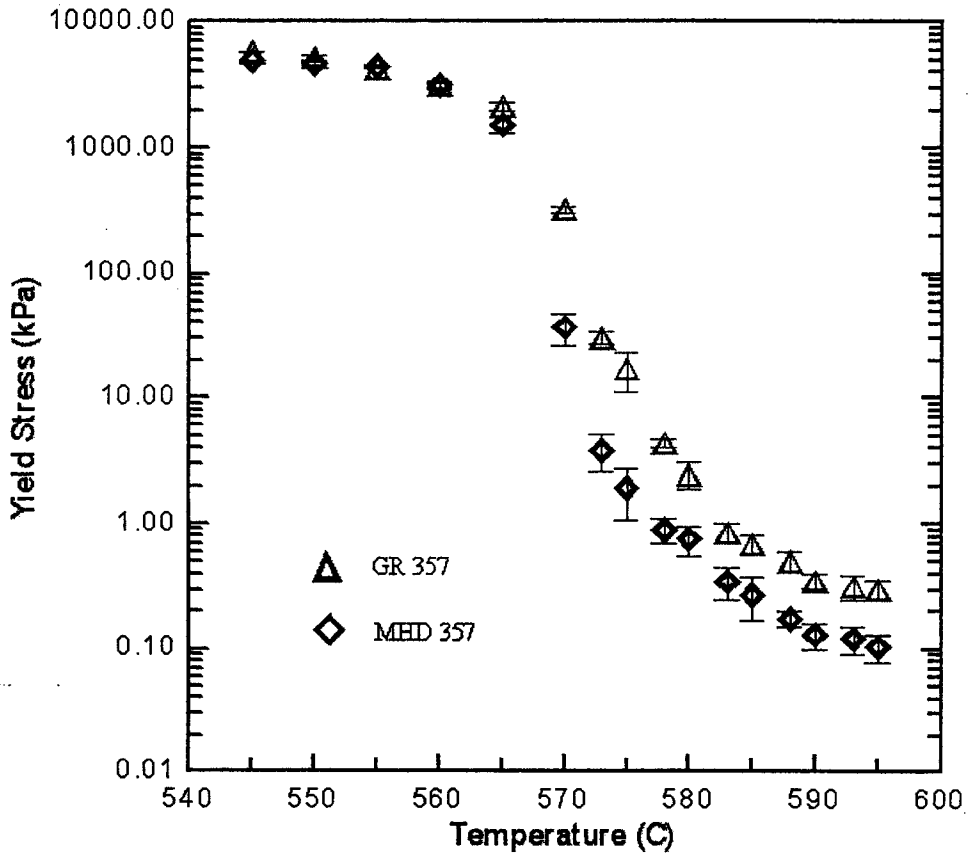

Figure 7: Yield stress of 357 alloy as a function of temperature [13].

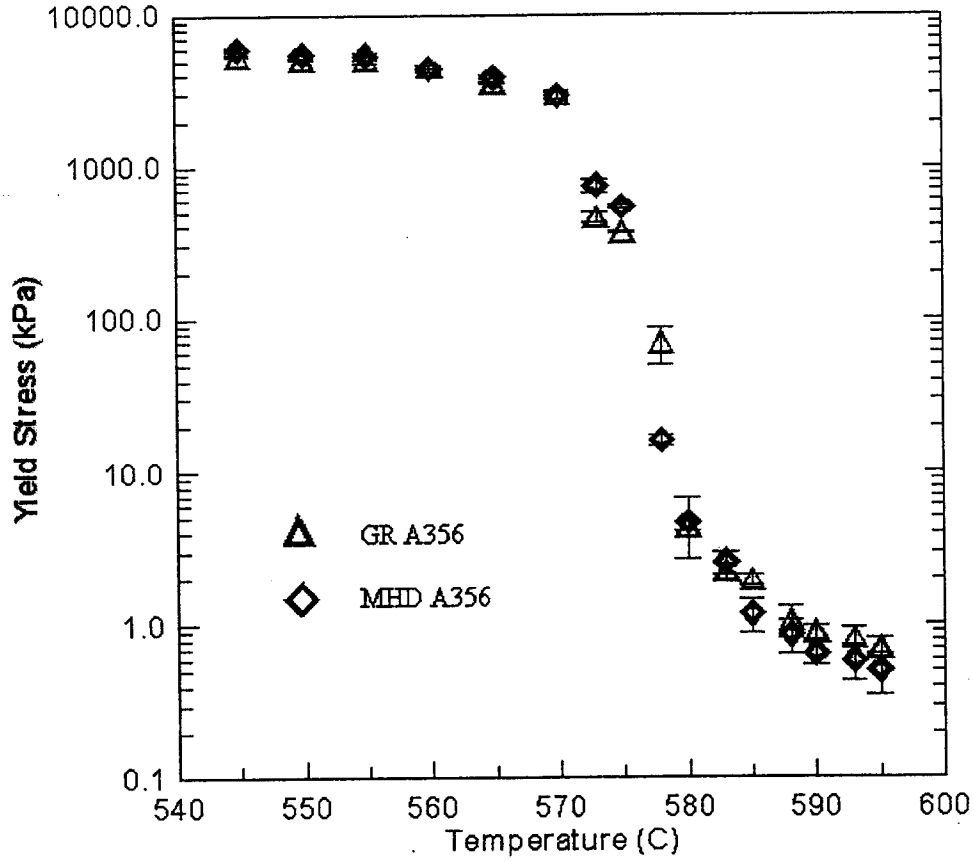

Figure 8: Yield stress of 356 alloy as a function of temperature [13].

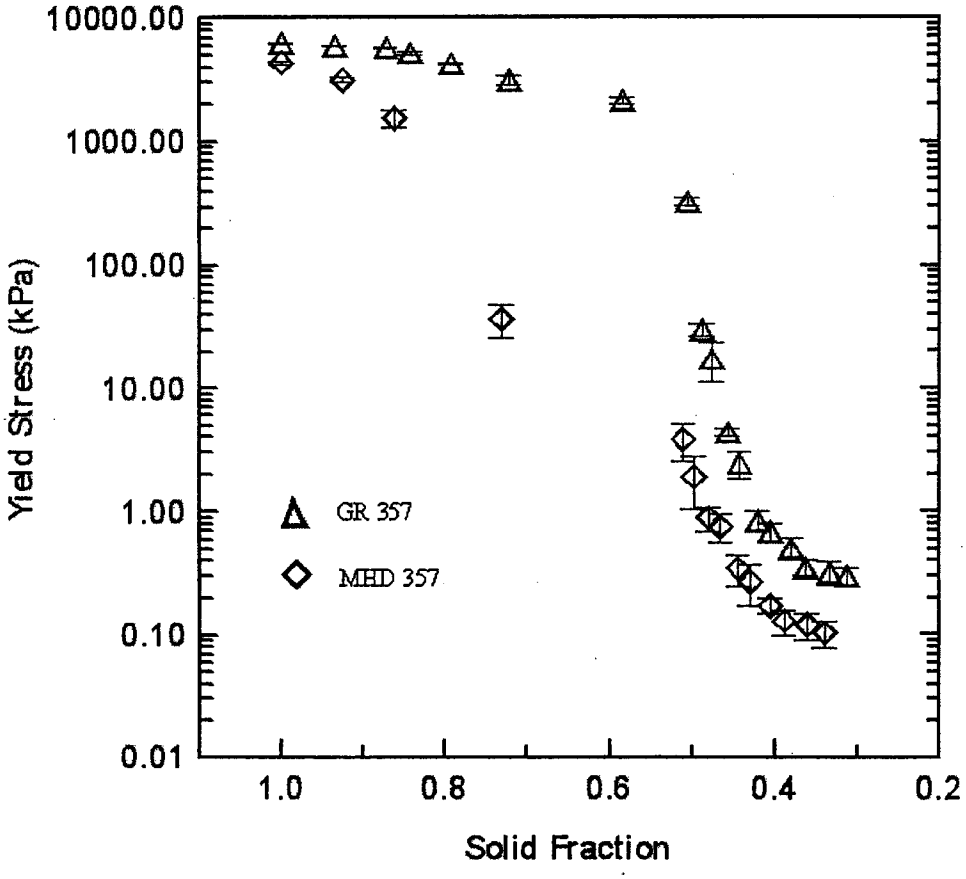

Figure 9: Yield stress of 357 alloy as a function of solid fraction [13].

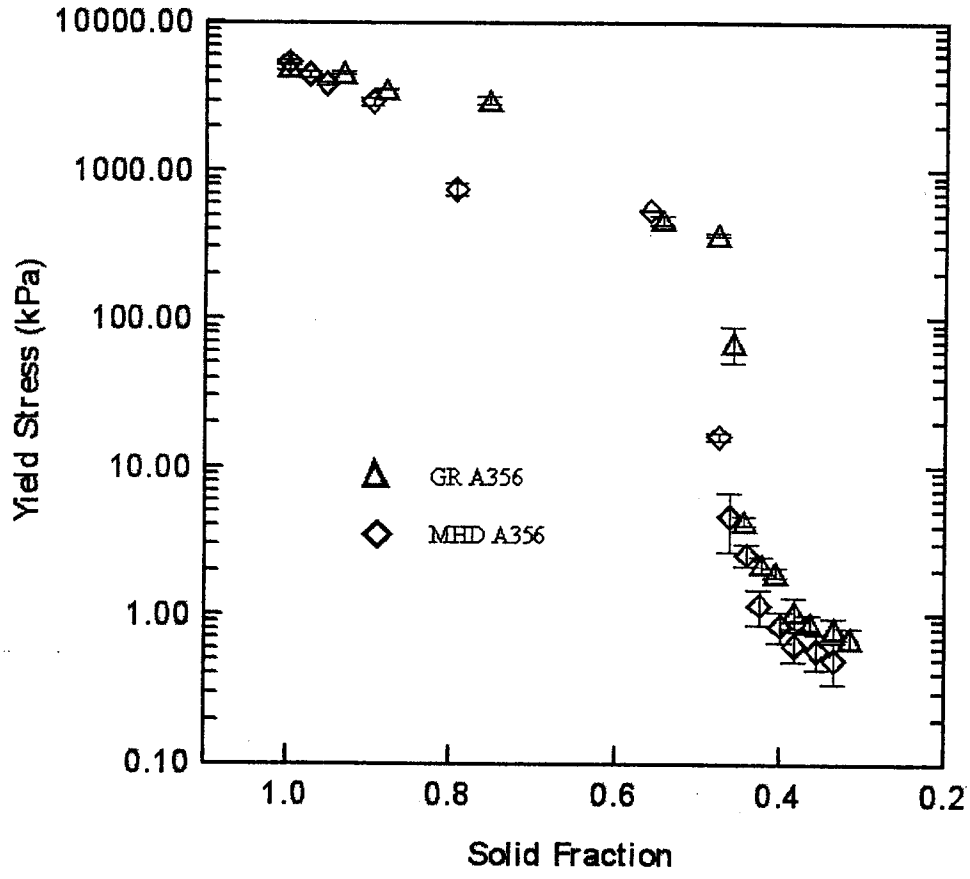

Figure 10: Yield stress of 356 alloy as a function of solid fraction [13].

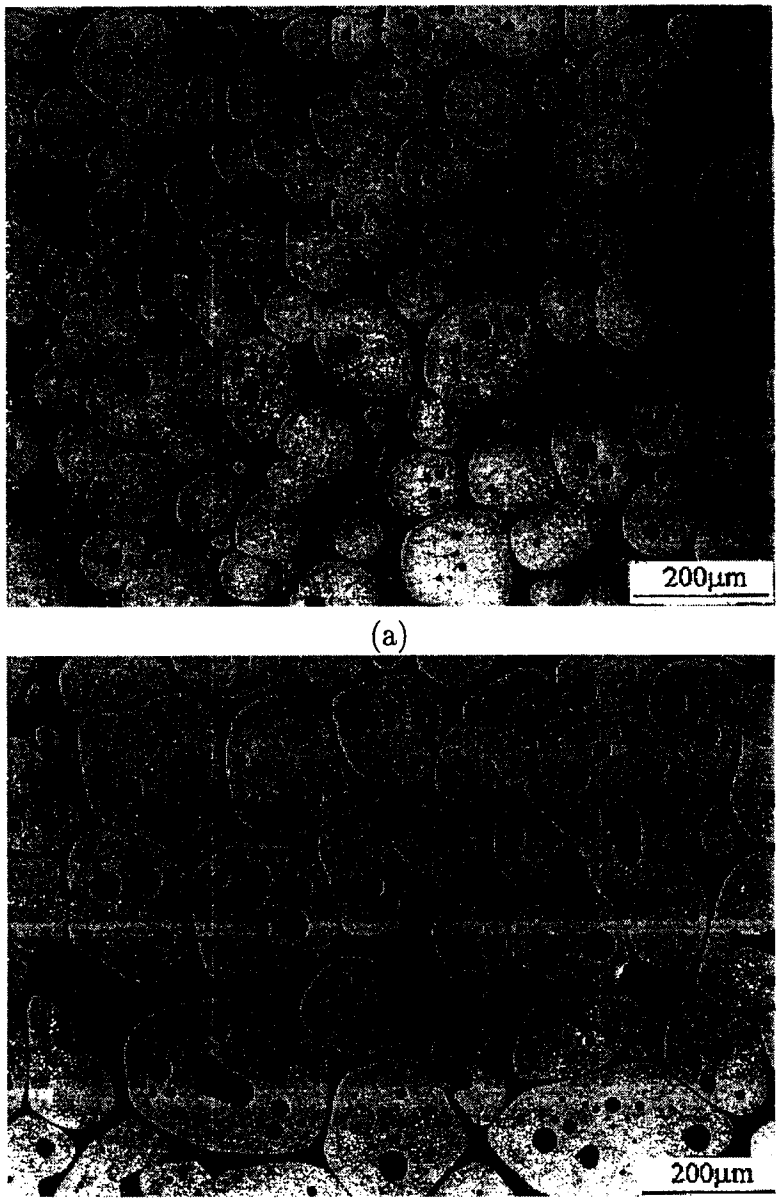

(a)

(b)

Figure 11: Microstructure of MHD 357 (a), and GR 357 (b) at 578°C.

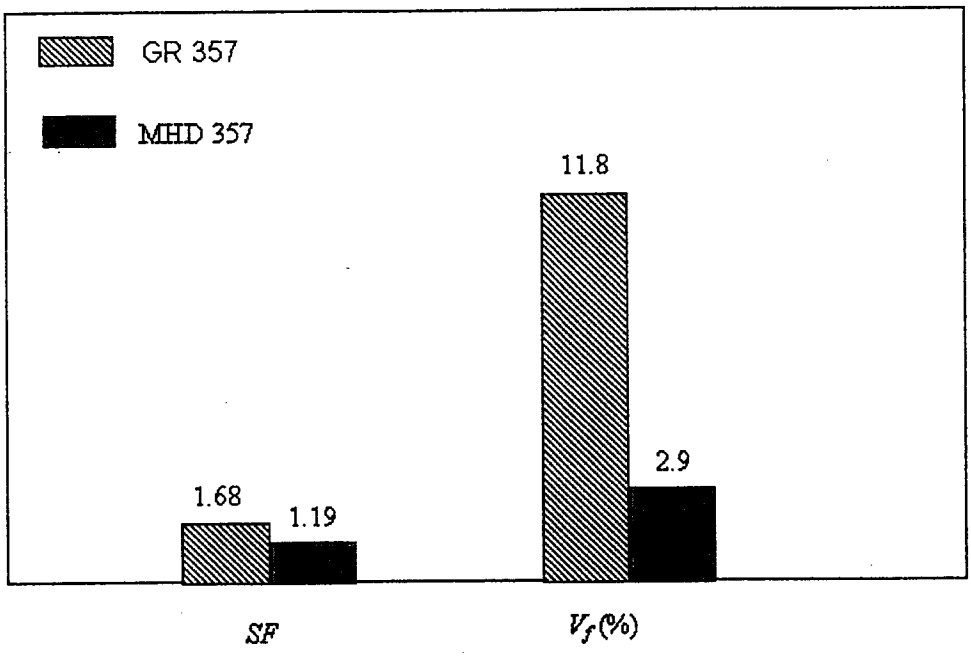

Figure 12: Image analysis results of MHD and GR 357 alloys evaluated. SF is the shape factor, V_f is the volume fraction of entrapped liquid.

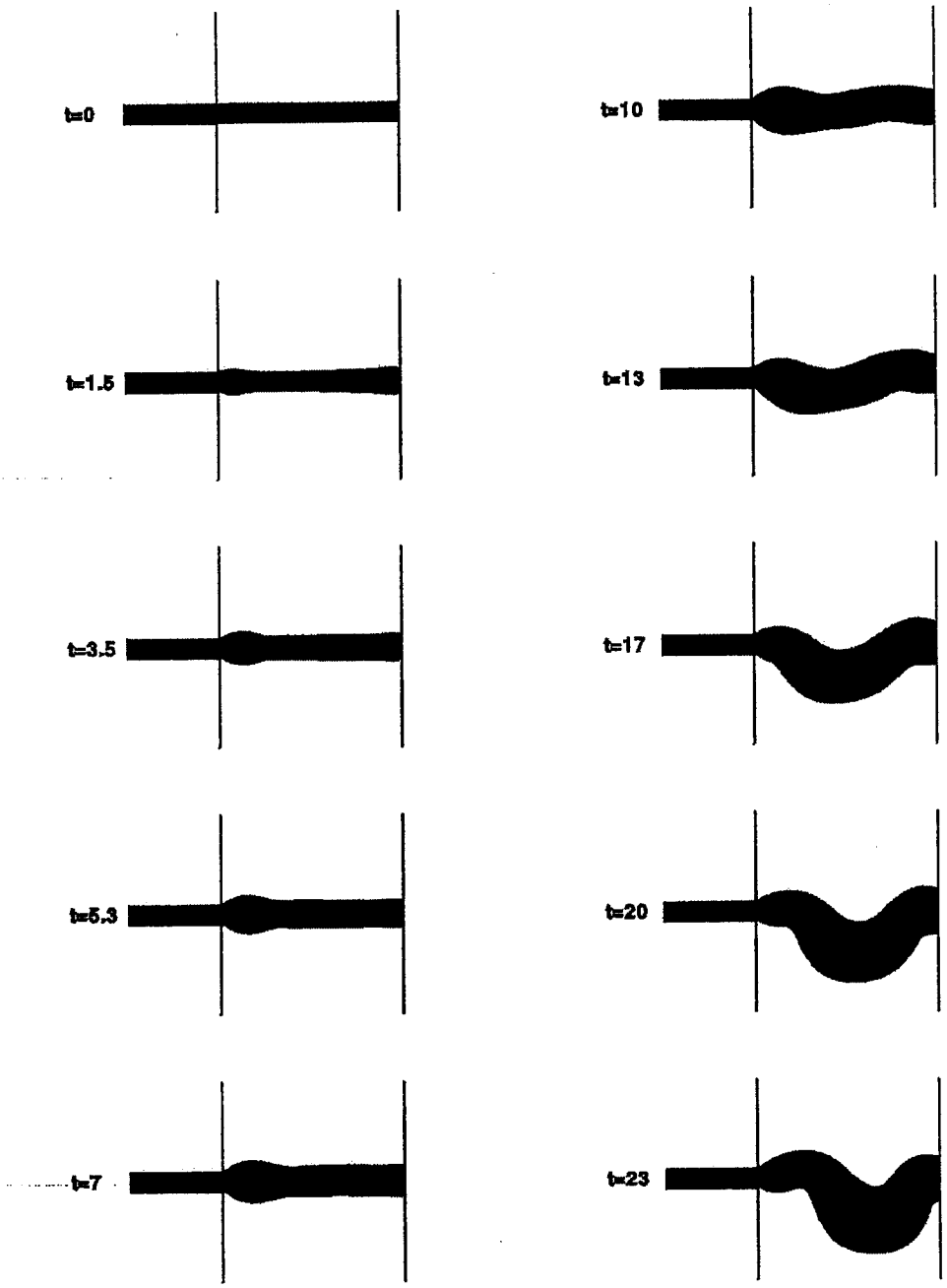

Figure 16: Toothpaste behavior, $Re = 1$, $Bi = 3$, $L = 10$. The disturbance is imposed from $t = 0$ until $t = 1.5$.

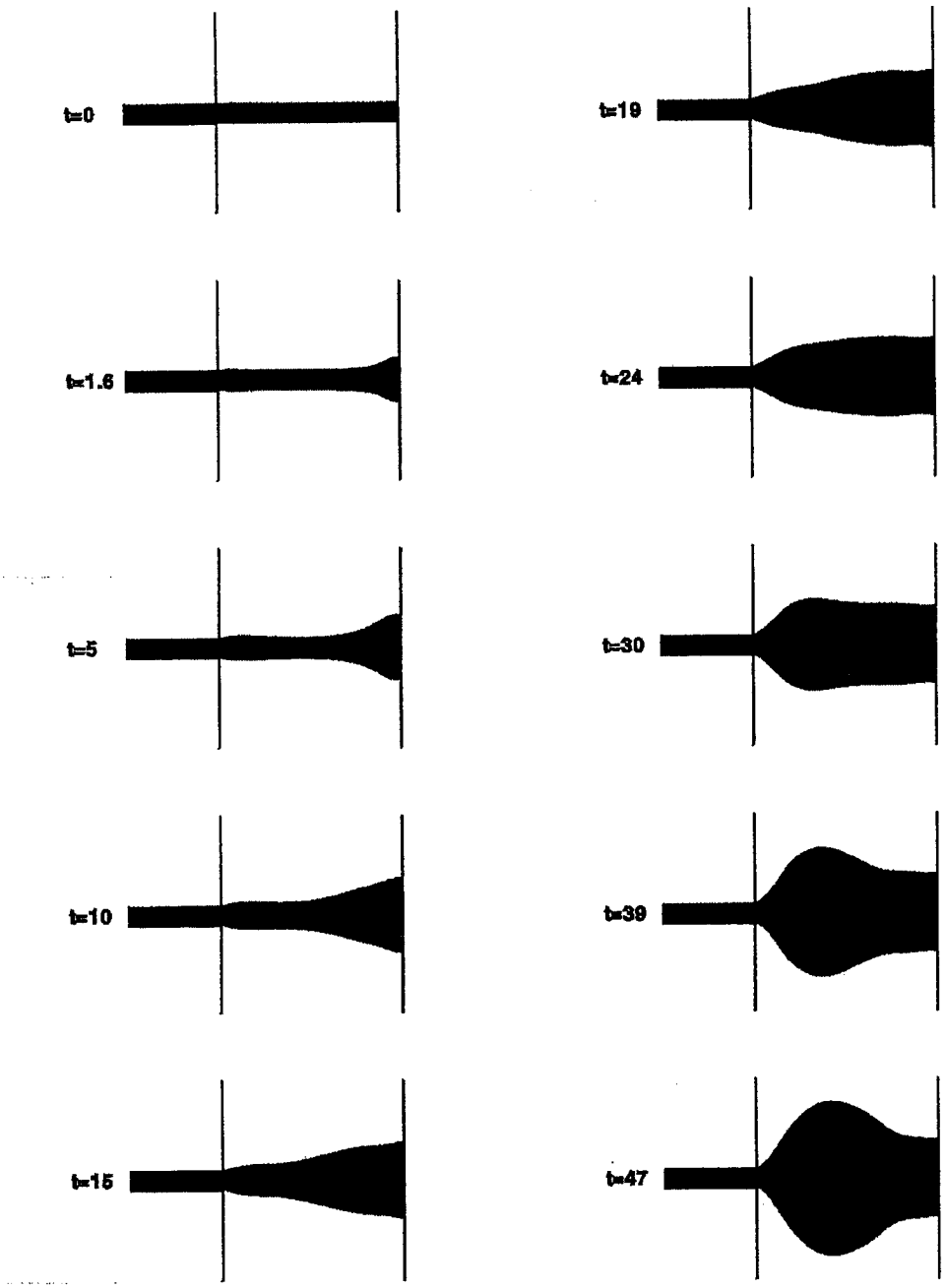

Figure 17: Stable filling behavior, $Re = 5$, $Bi = 1$, $L = 10$. The disturbance is imposed from $t = 0$ until $t = 1.5$.

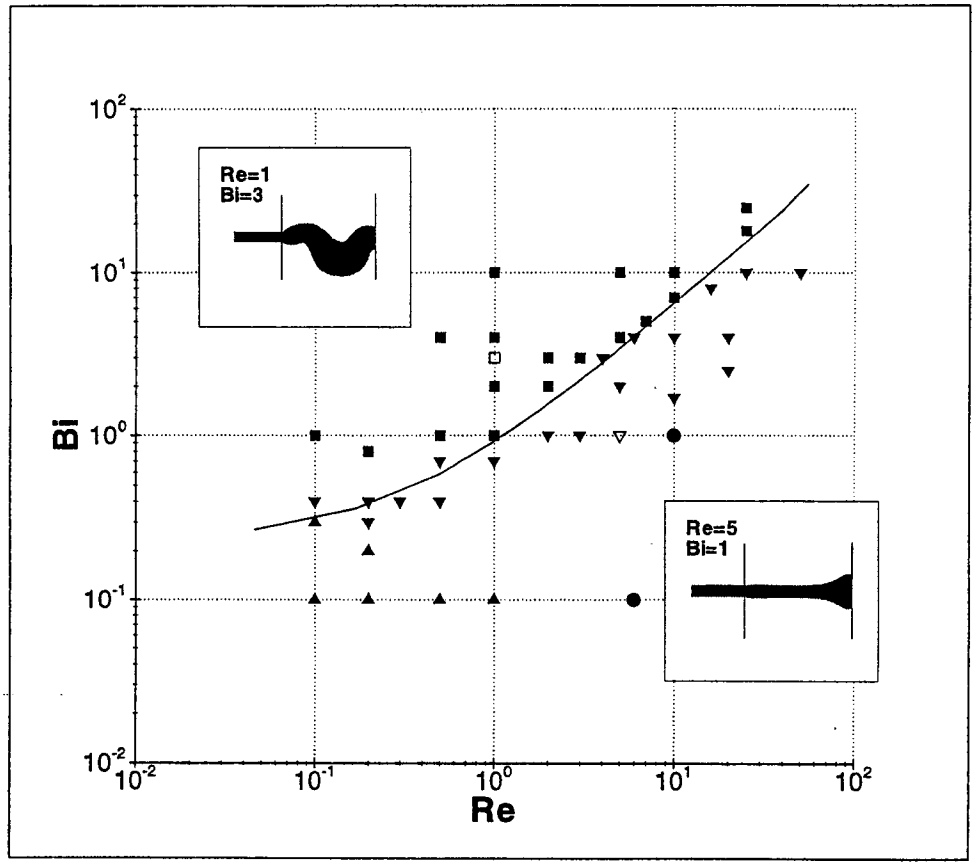

Figure 18: Stability of the jet when hitting a vertical suface ($L = 10$), the Reynolds and Bingham numbers being the control parameters. ▲-mound pattern; •-disk pattern; ■-bubble pattern; ▼-transition pattern. The hollow symbols (□, and ▽) represent the cases discussed in detail and pictured on the map. The estimated boundary between the stable and unstable behaviors has been sketched in. Stable and unstable behaviors are respectively below and above this limiting line.

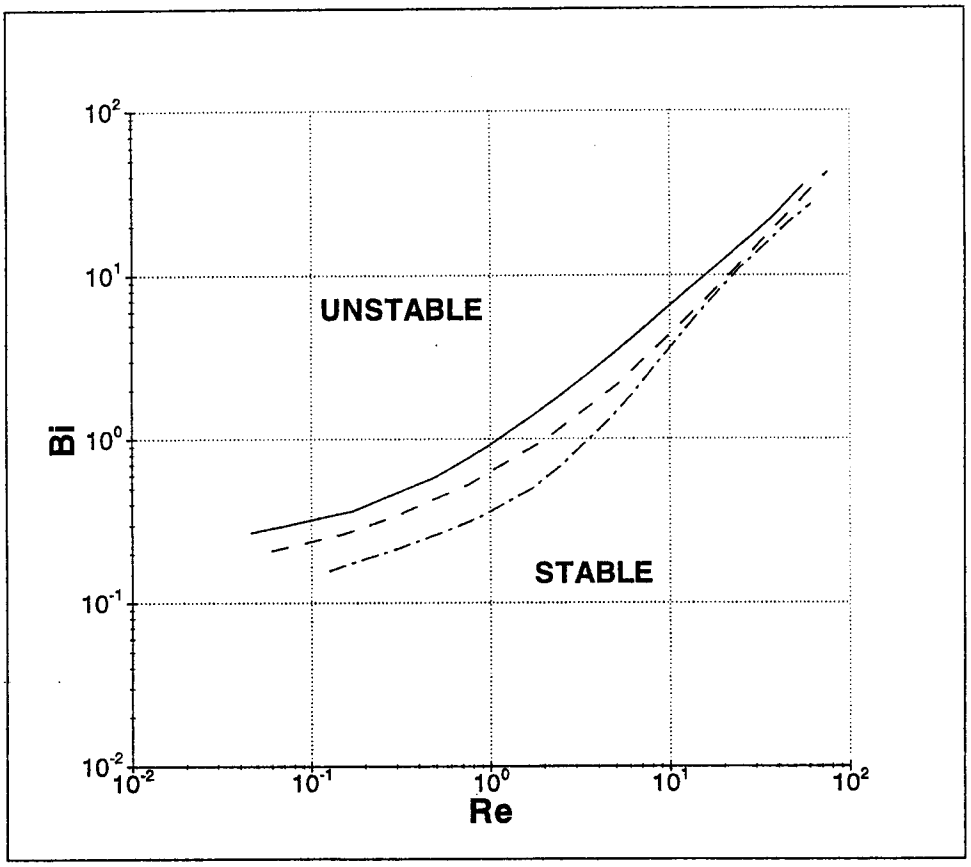

Figure 19: Estimated stability limits for different jet lengths. $L = 10$ (solid line), $L = 15$ (dashed line) and $L = 20$ (dashdotted line).

B. Quantitative Microstructure Characterization of Commercial Semi-Solid Aluminum Alloys

QUANTITATIVE MICROSTRUCTURE CHARACTERIZATION OF COMMERCIAL SEMI-SOLID ALUMINUM ALLOYS

Report PR-01-#1

Research Team:	Qingyue Pan	(508) 831 5790	qypan@wpi.edu
	Diran Apelian	(508) 831 5992	dapelian@wpi.edu
	A.Figueredo	(508) 831 6157	amf@wpi.edu
	Carsten Afrath	49 241 9800521	
		Carsten.Afrath@post.rwth-aachen.de	
Focus Group:	John Miller		
	Craig Bergsma	(Northwest Aluminum)	
	Stig Brusethaug	(Hydro Aluminum A.S.)	
	Karuppa Chinnathamba	(Citation Aluminum)	
	Vincent Genise	(Citation Aluminum)	
	Tom DeJohn	(Superior Industries International)	
	Michel Garat	(Aluminum Pechiney)	
	Alain Charbonnier	(Aluminum Pechiney)	
	John Jorstad	(JLJ Technologies)	
	Rod Riek	(Harley-Davidson Motor)	
	Jim Van Wert	(Amcast)	

PROJECT STATEMENT

Objectives

- Determine effect of heating rate and processing temperature on microstructural evolution of semi-solid A356 alloy during reheating.
- Determine effect of isothermal hold on microstructure evolution in the semi-solid state.
- Characterize differences in microstructure evolution of commercial semi-solid billets at different locations throughout the billet.
- Investigate mechanism on the formation of entrapped liquid.
- Provide quantatitive data for optimization of industrial practice.

Strategy

- The rheological behavior and flow properties of commercial semi-solid alloys depend on their microstructure developed during reheating. Thus an accurate understanding of microstructure evolution at commercial processing conditions is critical for optimization and control of semi-solid processing.

- Both chemically grain refined and MHD A356 commercial billets were used in this study. Processing conditions investigated include different heating rates, different shearing rates, as well as isothermal hold at commercial forming temperatures.

- Image analysis was carried out to quantify the semi-solid microstructure. Three important characteristic parameters-shape factor, particle size of Alpha particles, as well as the amount of entrapped liquid were measured in this study.

- Specifically, due to the significant difference in as-cast microstructure of commercial billet at different locations (for example, at the center or surface of an individual billet), extensive image analysis were performed on samples along cross section of the billet to identify differences in microstructure at different locations.

ACHIEVEMENTS THIS QUARTER

During this quarter, extensive sample preparation and image analysis were carried out to quantify microstructure of samples obtained at different commercial processing conditions. Detailed results are given as follows.

1. The microstructural evolution of MHD and GR billets during reheating is quite different. GR billets tend to have higher shape factor values, larger particle size, and much more entrapped liquid than MHD billets.

2. Heating rate does not alter microstructure evolution of both MHD and GR billets significantly. Rather, processing temperature has a much more of an influence on microstructure evolution of both billets. Higher temperature results in faster spheroidization, and a significant decease of entrapped liquid of GR billets.

3. Isothermal holding at 580°C leads to rapid spheroidization throughout MHD billet, and the periphery of GR billet, but has little effect on the microstructures at the center of GR billet. Coarsening during isothermal hold is most evident.

4. Semi-solid microstructure has a strong structural "heredity" resulting from the as-cast microstructure. It is difficult to eliminate the heredity to obtain an optimal spherical morphology through subsequent thermal treatments if the scale of the as-cast microstructure is above a certain threshold level. Our analysis of quantitative data points out that the control of cooling rate is critical in manufacturing high quality, commercial SSM feedstock.

Appendix A is a detailed report on the quantitative microstructural characterization of commercial A356 alloy.

CHANGES IN PROJECT STATEMENTS

None

WORK PLANNED FOR NEXT QUARTER

- Complete remaining image analysis work to identify mechanism of formation of the entrapped liquid.
- Complete yield stress measurement of SiBloy, grain refined SSM alloys.
- Documentation of all microstructural work to date.

OPERATIONAL SCHEDULE

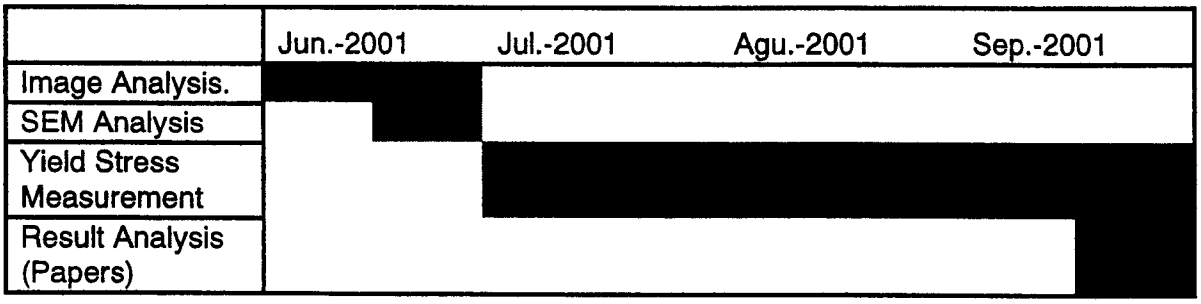

Appendix A

QUANTITATIVE MICROSTRUCTURE CHARACTERIZATION OF COMMERCIAL SEMI-SOLID ALUMINUM ALLOYS

PR-01-#1

Qingyue Pan, Diran Apelian, Anacleto de Figueredo

Advanced Casting Research Center (ACRC)
Metal Processing Institute
WPI, Worcester, MA 01609

Carsten Afrath

Aachen University of Technology
52072 Aachen, Germany

ABSTRACT

Extensive microstructure observations and image analysis were performed to quantitatively characterize microstructural evolution of semi-solid A356 alloy billets during reheating. In this study, commercial billets fabricated by both magnetohydrodynamic (MHD) and chemically grain refined (GR) methods were used. Processing parameters evaluated include different heating rates, temperatures, isothermal hold time as well as different shear rates. It has been found that the microstructural evolution of MHD in contrast to GR billets during reheating is quite different. GR billets tend to have higher shape factor values, larger particle size, and much more entrapped liquid than MHD billets. Heating rate has little effect on the microstructural evolution of both types of billets, while processing temperature has a significant influence on microstructure evolution. Higher temperature results in a faster spheroidization, and a significant decease of entrapped liquid of GR billets. Isothermal holding at 580 ℃ leads to a rapid spheroidization throughout MHD billets, and the periphery of GR billets, however, it has little effect on the microstructures at the center of GR billets. Specifically, we found that semi-solid microstructure has a distinct structural "heredity" resulting from precursor material, which implies that once the scale of the as-cast microstructure is beyond a certain level, it is difficult to obtain the expected spherical morphology through subsequent thermal treatments. Our analysis of quantitative data points out that the control of cooling rate is critical in manufacturing high quality commercial semi-solid billets, particularly for GR feedstock.

1. INTRODUCTION

Thixoforming aluminum alloys is a relatively new casting technology offering distinct advantages over conventional casting and forging processes. Thixoformed parts can have thinner sections than in squeeze cast parts with improved mechanical properties. Moreover, due to laminar flow during mold filling, thixoforming ensures casting quality, including absence of inclusions, possibility of heat treatment and welding, high strength and elongation. Though we have witnessed several successful commercial launches with SSM, and even through much progress has been made during the last few years in our understanding, the fact remains that predictive and fundamental knowledge in SSM rheological properties as well as microstructural evolution is still incomplete.

Process robustness and quality assurance measures are based on our accurate understanding of the rheological behavior of semi-solid metal slurries. Thixofoming involves three distinct stages: (1) casting of billet with microstructure suitable for thixoforming; (2) reheating of slugs cut from these billets into semi-solid state; and (3) injecting the semi-solid slurry into a die. Commercially, semi-solid billets are manufactured either by magnetohydrodynamic (MHD) or chemically grain refined (GR) methods to ensure development of proper semi-solid structures. Figures 1 and 2 give the typical as-cast microstructures of both MHD and GR billets. It can be seen that MHD and GR materials exhibit significant microstructural differences. The microstructure of GR billets has a dendritic structure with a very fine scale; while the microstructure of MHD billets has a non-dendritic, rosette-like structure with agglomerated Alpha particles. Specifically, comparing microstructures of an individual billet at different locations (center or periphery), one can find that microstructures near the billet surface are much finer than those at the billet center due to relatively high cooling rates during billet casting .

It is well known that the rheological behavior of semi-solid metal slurries is strongly dependent on microstructure. To elucidate the complex rheological behavior of SSM slurries, it is important to understand how the precursor microstructure evolves during reheating of the billet into the semi-solid range. The relevant questions we have posed are:

1) How do the observed differences in as-cast microstructures affect the microstructure evolution during reheating?
2) What is the effect of a billet genealogy (MHD, GR, etc.) on the slurry structure?
3) What metrics are used to design heating procedures to ensure the required rheological properties?

Kopper and Apelian [1-2] investigated microstructure evolution of 357 aluminum alloy during reheating and its effect on the flow properties. Their work pointed out that the semi-solid microstructure is very much path dependent. For a given billet stock, factors such as heating rate, soak temperature, and soak time are critical variables affecting the resultant microstructure, and thus the flow properties. Pan and Apelian [3-4] investigated

the yielding behavior of commercial aluminum alloys A356 and 357 in the semi-solid state. Their work indicated that the yield stress of the semi-solid slurry is a strong function of temperature/solid fraction. For a given solid fraction, some characteristic parameters of semi-solid microstructure such as the amount of entrapped liquid, shape factor of the Alpha particles have a significant influence on yield stress and flow properties.

In this work we have taken on the task to quantitatively characterize microstructural evolution of commercial A356 semi-solid billets during commercial forming conditions. Effects such as heating rate, isothermal hold, shear rate on slurry structure have been evaluated. This report presents recent results on microstructure evolution of A356 alloy as a function of different thermal histories. Specifically, much attention will be paid to identify differences in microstructural evolution throughout a given semi-solid billet.

2. EXPERIMENTAL

2.1 Materials

Commercial A356 semisolid billets fabricated by both magneto hydrodynamic (MHD) and grain-refined (GR) methods were used in this study. Table I gives the chemical composition of the alloys used. Samples with 3 inches in diameter and 0.25 inch in thickness were cut directly from commercial MHD and GR billets.

Table I: Chemical composition of the alloys investigated

Alloy	Composition, %				
	Si	Fe	Cu	Man	Mg
A356 (MHD)	6.92	0.10	0.09	0.05	0.18
A356 (GR)	6.85	0.10	0.11	0.05	0.33

2.2 Apparatus

An Inston high temperature chamber was used with an accurately controlled environment; a convection fan ensures even distribution of the atmosphere, maintaining the desired temperature. The temperature variation in a sample during an experimental run was kept within ± 1°C in the temperature range investigated (577°C-590°C). The sample was placed in a copper container, and a thermocouple was inserted into the sample to monitor temperature variations (see Figure 3).

2.3 Processing Conditions

Processing conditions investigated in this study include different heating rates and temperatures, isothermal hold time, as well as different shear rates, as illustrated in Figure 4.

The ***first series*** of experiments dealt with the effect of heating rate on microstructure evolution during continuous heating in the semi-solid state. Two heating rates were examined

- Rapid heating (49^0C/min.)
- Slow heating (4^0C/min.)

The ***second series*** of experiments was designed to investigate the effect of isothermal hold on microstructural evolution at a temperature commonly used in commercial forming operations (580°C). Holding time varied from 1 to 64 minutes.

The ***third series*** of experiments focused on the effect of deformation by shear on the semi-solid microstructure. Two shear rates were examined. The high shear rate ($10^3 s^{-1}$) experiments were performed using MIT's forging apparatus, and the low shearing rate ($5\times10^{-3} s^{-1}$) experiments were carried out using parallel plate compression set-up reported before [4]. Liquid microsegregation due to the applied deformation was investigated.

2.4 Microstructure Characterization

Metallographic observations were made on water-quenched samples. The specimens were etched with Keller's reagent after mounting, grinding, and finally polishing.

Microstructure characterization was performed using optical microscopy and image analysis (microGOP2000/S). Three specific microstructural parameters were measured to quantitatively characterize semisolid microstructures:

(i) particle size, D
(ii) shape factor, SF
(iii) entrapped liquid in the primary particles, V_f

The particle size (D) is determined by

$$D = 2 \times \sqrt{\frac{A}{\pi}} \qquad (1)$$

Where A is the area of the particle. The average particle size is the mean value of the total numbers of particles measured. The shape factor (SF) is defined as

alloy has more entrapped liquid. As the entrapped liquid does not participate in the deformation during filling, it has the effect of decreasing the "effective" liquid fraction, and causes an increase in the deformation force (yield stress). On the other hand, the higher shape factor of GR alloy leads to a larger flow resistance of the intergranular liquid, and as a result, the deformation force (yield stress) of GR alloy is increased. Specifically, their analysis of the experimental data points out that the contribution of yield stress to the apparent viscosity value is dominant during commercial forming condition. Thus the inclusion of yield stress in modeling the rheological behavior of semi-solid metals is critical.

Once the yield stress is exceeded, the material flows following a non-linear stress-strain relationship, either as a shear-thickening or shear-thinning fluid. The shear rate can be understood as the speed at which the slurry is deformed. If the effective viscosity of the material increases with increasing shear rate, it is said to be shear-thickening. On the other hand, if the effective viscosity of the material decreases with increasing shear rate, it is called shear-thinning. These two typical fluid behaviors are shown in Fig. 13. Under steady shear and temperature (steady-state conditions), a semisolid alloy behaves as a shear-thinning material [14, 15]. However, in rapid processing conditions (short-term transient behavior), semisolid slurries tend to exhibit a shear-thickening behavior [16]. This shows that the immediate response of a semisolid slurry is radically different from the steady-state one. Additionally, whether the shear rate is suddenly increased or decreased makes a difference in the reaction time of the slurry. This means that agglomeration and de-agglomeration of solid networks do not happen at the same velocities. In other words, the rheological fluid properties are time-dependent or thixotropic. This time-dependence has already been studied by Burgos et al. [17] and we will not consider it in the present investigation.

3 Material modeling

To accurately describe the rheological behavior of semisolid materials, a two-phase model is required. Indeed, since particles interact with both solid and liquid phases during deformation, a one-phase model does not seem sufficient to describe the semisolid behavior. However, no accurate and effective

$$SF = \frac{P^2}{4\pi A} \qquad (2)$$

Where P is the perimeter of the particle. For a perfectly globular shape, SF is equal to 1. The shape factor values reported here are the mean values of the total numbers of particles measured.

In order to obtain results of statistical significance, more than twelve images were analyzed for each sample. Specifically, measurements along the sample radius were performed to identify differences in microstructure throughout the billet.

3. RESULTS & ANALYSIS

Microstructural evolution of A356 alloy as a function of temperature and heating rate is presented below in section 3.1. Microstructure evolution during isothermal holding at 580°C is presented in section 3.2. This is followed by the microstructural characterization of samples deformed at different shear rates.

3.1 Microstructural Evolution during Continuous Reheating

3.1.1 High heating rate (49^{0}C/min.)

Figures 5 and 6 detail microstructure evolution of both MHD and GR billets as a function of forming temperature in the semi-solid state. Significant differences in microstructure evolution can be observed between the two kinds of materials. Upon reheating, the dendritic structure in the as-cast GR billet is no longer evident. Rather, large asymmetrical globules with large amount of entrapped liquid dominate the GR microstructure; while for the MHD billet, its microstructure is characterized by round spheroid particles in a eutectic matrix. Although entrapped liquid is apparent, it is much less severe than what is seen in the GR billet.

Specifically, comparing microstructures at different locations of the same billet, one can find that significant differences exist throughout the GR billet. In all cases, the microstructure near billet surface has a much smaller, and more spherical Alpha particles than those at the billet center. While for MHD billet, it is not the case. The only noticeable difference is the degree of agglomeration of Alpha particles. The Alpha particles at the billet center tend to have a higher degree of agglomeration.

From a rheological standpoint, an "ideal" semi-solid microstructure is composed by small, round alpha particles containing no entrapped liquid and homogeneously distributed in a eutectic phase. The small size of the alpha particles is beneficial for the casting of thin-walled parts, while a more spherical shape, and the absence of the

entrapped liquid are critical for the improvement of the slurry flow properties during filling.

We believe that the semisolid microstructure can be fully characterized by three characteristic parameters. They are

- Shape factor
- Particle size
- The amount of entrapped liquid

Figure 7 shows the image analysis results of the evolution of the shape factor as a function of temperature. It can be seen that with increasing temperature, the shape factor of both MHD and GR billets decreases. This is expected because higher temperature provides additional activation energy for mass transport. The driving force for spheriodization becomes stronger as the surface energy is increased. It should be pointed out that although both MHD and GR billets show a similar tendency, the microstructures at the billet center have higher shape factor values, indicating that the spheroidization process is relatively slow. This is consistent with direct microstructure observations.

Figure 8 gives the evolution of particle size as a function of temperature. It can be seen that in the temperature range between 577and 585°C, the particle size of both MHD and GR billets tends to a constant value. A significant increase in particle size starts only at temperature above 588°C. In most cases, the particle size of MHD alloy is below 100 μm, and the distribution of particle size is homogeneous throughout the billet. Whereas the particle size of GR alloy is much larger, falling in the range of 100-180 μm, moreover, the particles size distribution is quite different throughout the GR billet. Particles around the billet center are about 30% larger than those near the billet surface.

Figure 9 gives the evolution of entrapped liquid as a function of temperature. It can be seen that a significant difference exists between MHD and GR alloy. The amount of entrapped liquid in GR alloy is 3-4 times higher than in MHD alloy in the temperature range between 580-585°C. Specifically, temperature has a strong effect on the entrapped liquid of the GR alloy. With increasing temperature, the amount of entrapped liquid of GR alloy decreases dramatically, whereas temperature has little effect on the entrapped liquid of MHD alloy.

3.1.2 Low heating rate (4^0C/min.)

Figures 10 and 11 depict microstructural evolution of both MHD and GR billets as a function of temperature at low heating rate (4^0C/min.). Visually, the microstructure evolution is very similar to the high cooling rate samples (Figures 5-6). However, detailed image analysis identified the following differences:

- For both slow and rapid heating rates, the forming temperature has a similar effect on the shape factor. However, a comparison of the slope of shape factor vs.

temperature curves at both conditions shows that slow heating leads to a faster spheroidization process (see Figure 12).

- Slow heating has a similar effect on the Alpha particle size as found during rapid heating, however, a minimum value in globule size is seen for both the GR and the MHD samples at about 582°C. This can be explained as a result of the competition between melting and coarsening processes, which did not manifest itself clearly when the specimens were subjected to continuous heating at a higher rate (see Figure 13).

3.2 Isothermal Hold at 580 ℃

Figure 15 shows the microstructure evolution of GR billets as a function of isothermal hold time at 580°C. A rapid evolution of Alpha particles towards a globular structure is clearly seen throughout the MHD billet, and as well as at the periphery of the GR billet. However, this is not the case for microstructures at the center of the GR billet. Instead, a very slow spheroidization was observed. Many large, asymmetrical and irregular globules are still evident in the GR billet even for isothermal holding time as long as 64 minutes (see Figure 15).

Image analysis points out that

- With increasing isothermal time, the microstructures throughout the MHD billet evolve rapidly towards a perfectly globular structure with a shape factor value of 1.1-1.2 (see Figure 16). Interestingly, the rapid spheroidization is also observed at the periphery of the GR billet, but not at the center. Actually, the shape factor of the microstructures at the billet center remains at a high level (around 1.4).

- As expected, isothermal holding leads to coarsening of Alpha particles. Specifically, a good linear dependence was found between the particles size and isothermal hold time (see Figure 17).

- Isothermal holding has no effect on the amount of entrapped liquid in MHD billet, however it greatly decreases the level of entrapped liquid in the GR billet (see Figure 18).

3.3 Microstructural Evolution under Different Shear Rate

Does liquid segregation exist in semi-solid forming? This is an interesting question because liquid segregation will cause problems during casting of semi-solid parts, which will degrade the resultant mechanical properties. Unfortunately, this phenomenon has not been investigated to a great extent, and its occurrence is somewhat controversial [5-8].

Figures 19-20 show typical microstructures of deformed MHD and GR samples at different shear rates. It can be seen that a significant difference in liquid fraction is evident only in MHD samples deformed at a low shear rate.

To quantitatively characterize liquid segregation, a parameter termed "degree of liquid segregation (DLS)" is used, which is defined as

$$DSL = \frac{\text{Fraction area of liquid at periphery of the deformed sample}}{\text{Fraction area of liquid at center of the deformed sample}} \quad (3)$$

Figure 21 presents the results of image analysis on all the deformed specimens. These results clearly show that significant liquid segregation does occur in the MHD specimens deformed at a low shear rate ($5\times10^{-3}s^{-1}$). The degree of liquid segregation can be as high as 1.44, while no significant liquid segregation is seen for GR alloy specimens at the same deformation conditions. For deformation at high shear rate (10^3 s^{-1}), however, no significant liquid segregation was observed for both types of materials.

It can be concluded from these results that the occurrence of liquid segregation is related to the deformation rate, as well as the material "genealogy". Among these, the role of deformation rate is predominant. Significant liquid segregation does not exist during high shear rate conditions; but it does exist at low shear rate conditions, particularly in deformed MHD alloy specimens. This finding clarifies conflicting claims regarding the existence of liquid segregation in previous studies [5-8],

4. DISCUSSION

4.1 Effect of Heating Rate on Microstructural Evolution

Comparing Figures 7-9 with Figures 12-14, one can find that heating rate does not alter microstructural evolution of both MHD and GR billets in a significant way. However, heating rate does affect the evolution of the shape factor to some extent. Lower heating rate tends to have smaller shape factor values, indicating a better spheroidazation during microstructure evolution. This observation is consistent with the results of Kopper and Apelian [1-2] in 357 alloy.

4.2 Effect of Temperature on Microstructural Evolution

Processing temperature, however, has a significant influence on microstructure evolution of both the MHD and GR billets. Higher forming temperature leads to a decrease of both shape factor and entrapped liquid content, particularly for GR billet. However, higher temperature tends to increase particle size. In addition, higher temperature may cause

excessive metal loss (run-off) as pointed out by Kopper and Apelian [1-2]. Therefore, 580-588°C is probably the most favorable temperature range for industrial forming of SSM parts. For GR billets, the upper limit is recommended in order to ensure sufficient flow properties during casting.

4.3 Effect of Isothermal Holding on Microstructural Evolution

Isothermal holding at 580°C results in a rapid spheroidization throughout MHD billet, and the periphery of GR billet, but has little effect on the spheroidization of microstructures at the center of GR billet. In addition, isothermal holding tends to reduce the amount of entrapped liquid in GR billet. However, isothermal hold also incurs coarsening of Alpha particles. Analysis of quantitative data points out that isothermal holding for 1-2 minutes is adequate for MHD billet, while a longer isothermal holding for 5-10 minutes is better for GR billet.

4.4 Differences in Microstructural Evolution throughout Semi-solid Billet.

Significant differences in microstructure evolution are clearly seen throughout GR billet, but not in MHD billet. In all cases, the microstructures at the center of GR billet show a much higher shape factor and a larger particle size; moreover, a strong microstructural "heredity" resulting from the as-cast microstructure has been observed, which implies that once the scale of the fine dendritic structure obtained via chemically grain-refining treatment is above a certain level, it is difficult to obtain optimal spherical morphology through subsequent thermal treatments. Specifically, our analysis points out that increasing cooling rate may be more important than chemically grain refining treatment in obtaining high quality billet.

5. CONCLUSIONS

1. The microstructural evolution of MHD and GR billets during reheating is quite different. GR billets tend to have higher shape factor values, larger particle size, and much more entrapped liquid than MHD billets.

2. Heating rate does not alter microstructure evolution of both MHD and GR billets significantly. Rather, processing temperature has much more of an influence on microstructure evolution of both billets. Higher temperature results in a faster spheroidization, and a significant decease of entrapped liquid of GR billet.

3. Isothermal holding at 580°C leads to a rapid spheroidization throughout MHD billet, and the periphery of GR billet, but has little effect on the microstructures at the center of GR billet. Coarsening during isothermal hold is most evident.

4. The occurrence of liquid segregation is related to the shear rate, strain rate, as well as the material "genealogy". Among these, the shear rate is predominant. Significant liquid segregation does not exist at high shear rate conditions; but exists at low shear rate conditions, particularly in deformed MHD alloy specimens at large strains.

5. Semi-solid microstructure has a strong structural "heredity" resulting from the as-cast microstructure. It is difficult to eliminate the heredity to obtain an optimal spherical morphology through subsequent thermal treatments if the scale of the as-cast microstructure is above a certain threshold level. Our analysis of quantitative data points out that the control of cooling rate is critical in manufacturing high quality, commercial SSM feedstock.

Acknowledgements

The authors are grateful to the Department of Energy's Office of Industrial Technologies (DOE-OIT) for their support to the Semisolid Processing Consortium at MPI, and the consortium members, our industrial partners, for their support and guidance.

References

1. A.Kopper and D.Apelian, in *"Proceedings of the 6th International Conference on the Processing of Semi-Solid Alloys and Composites*, Turin, September, **2000**, pp. 379-384.
2. A.Kopper, *"Microstructural Effect on the Flow Properties of Semi-solid Aluminum 357 Alloy'*, Master thesis, WPI, December, **1999**.
3. Q.Y.Pan and D.Apelian, in *"Proceedings of the 6th International Conference on the Processing of Semi-Solid Alloys and Composites*, Turin, September, **2000**, pp. 399-404.
4. Q.Y.Pan and D.Apelian, in *"Advanced Casting Research Center Consortium Meeting"*, December, **2000**.
5. W.R.Loue, M Suery and J.L.Querbes, in *"Proceedings of the Second International Conference on the Processing of Semi-Solid Alloys and Composites,"* eds. S.B.Brown and M.C.Flemings, **1992**, pp. 266-275.
6. M.Sury and M.C.Flemings, *Metall. Trans.*, vol. 13A, **1982**, pp. 1809-1819.
7. J.F.Seconde and M.Suery, *J. Mater. Sci.*, vol.19, **1984**, pp. 3995-4006.
8. M.Mada and F.Ajersch, in *"Proceedings of the Second International Conference on the Processing of Semi-Solid Alloys and Composites,"* eds. S.B.Brown and M.C.Flemings, Cambridge, Mass., USA, **1992**, pp. 276-289.

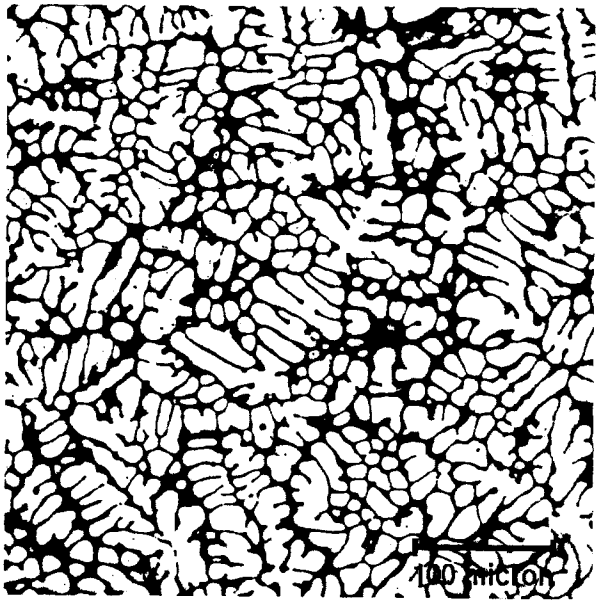

Figure 1(a)

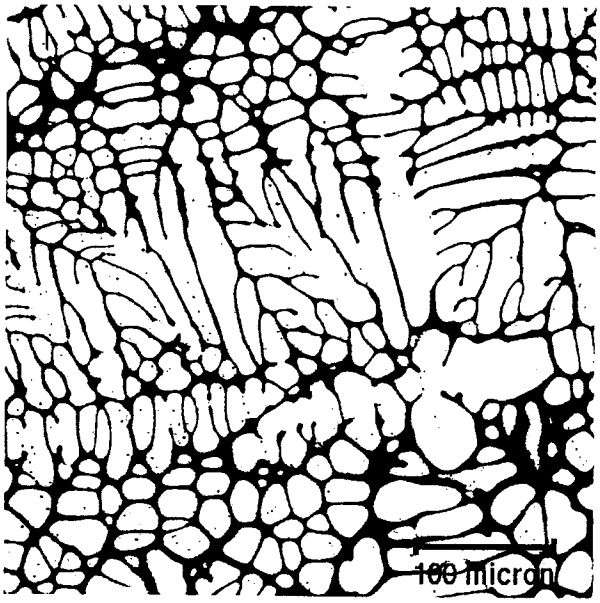

Figure 1 (b)

Figure 1: As-cast microstructure of A356 GR billet, (a) at the periphery, and (b) at the center.

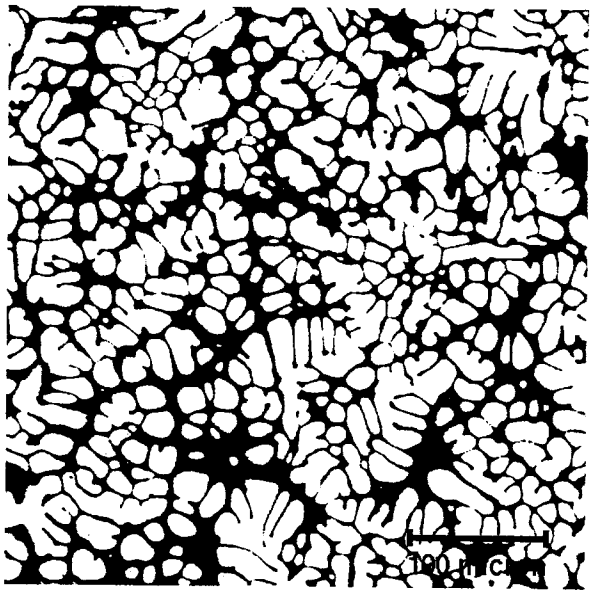

Figure 2(a)

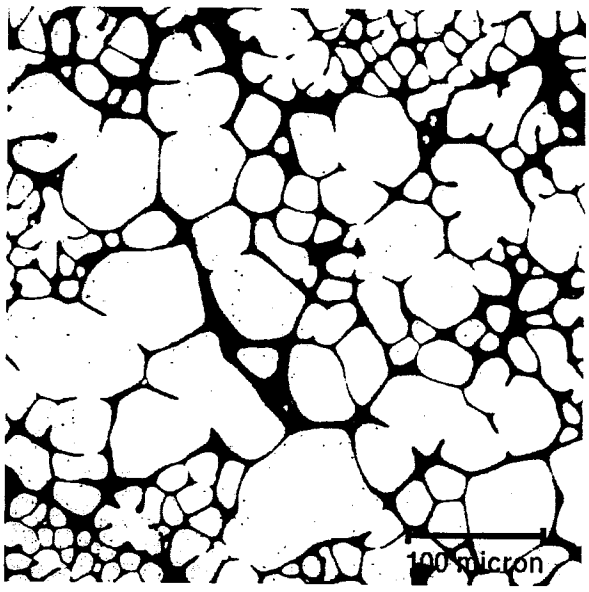

Figure 2(b)

Figure 2: As-cast microstructure of A356 MHD billet, (a) at the periphery, and (b) at the center.

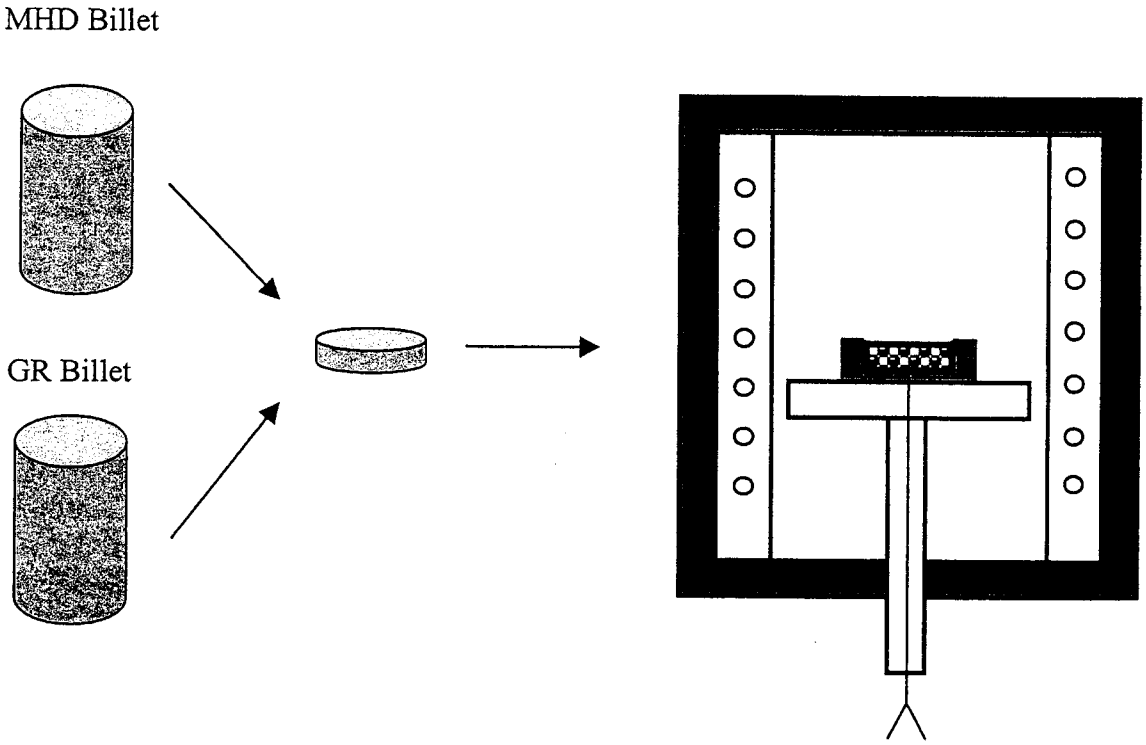

Figure 3: Schematic diagram of experimental procedures.

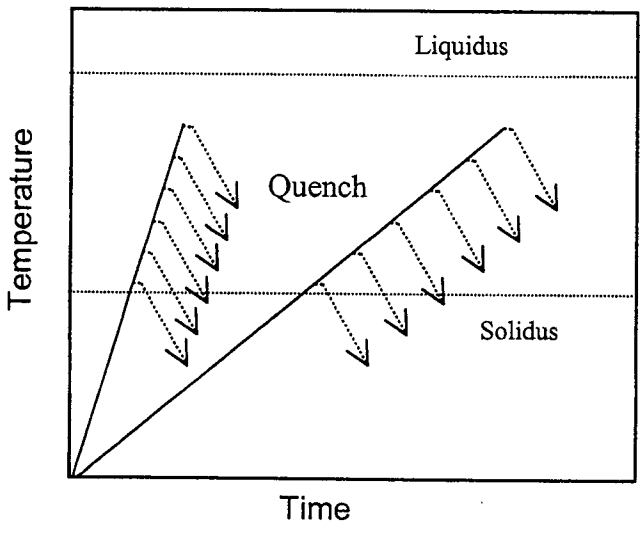

Figure 4 (a)

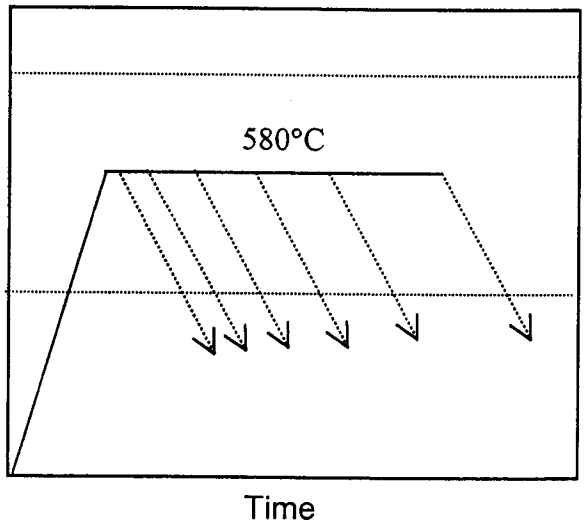

Figure 4 (b)

Figure 4: Schematic diagram of thermal treatments applied, (a) continuous reheating, and (b) isothermal holding.

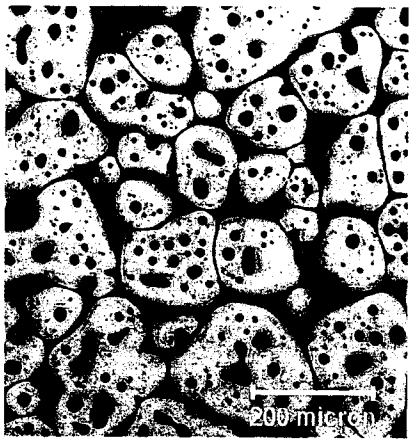

Fig. 5(a) 577°C

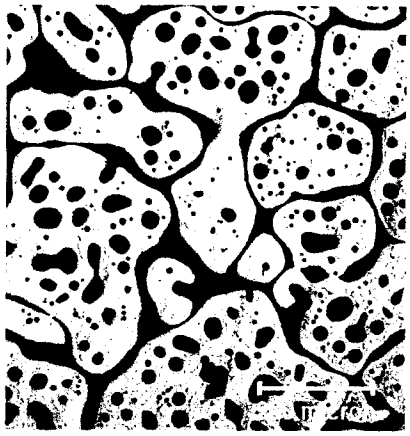

Fig. 5(a1) 577°C

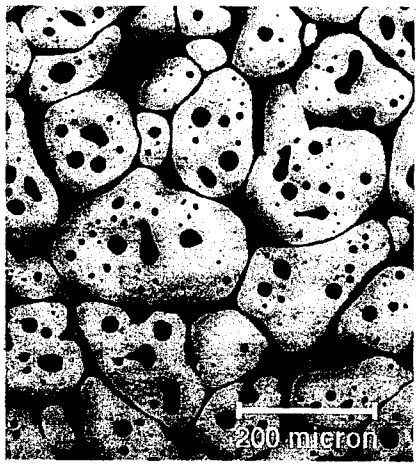

Fig. 5(b) 580°C

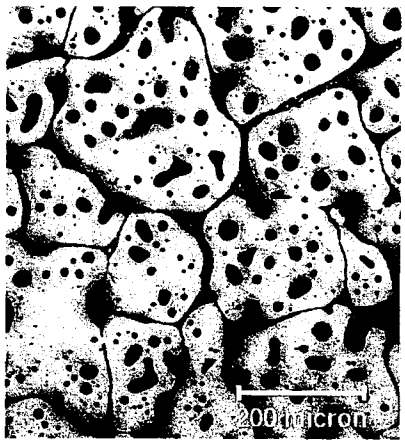

Fig. 5(b1) 580°C

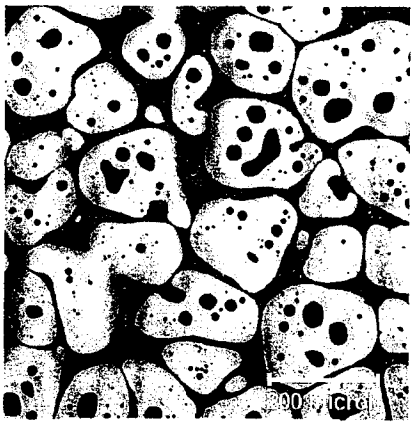

Fig. 5(c) 582°C

Fig. 5(c1) 582°C

Figure 5: Microstructure evolution of GR A356 billet as a function of temperature (heating rate: 49°C/min.), (a)-(b): samples taken from the periphery of the billet; (a1)-(c1): samples taken from the center of the billet.

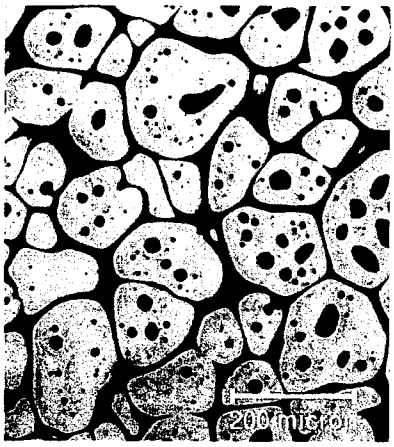

Fig. 5(d) 585°C

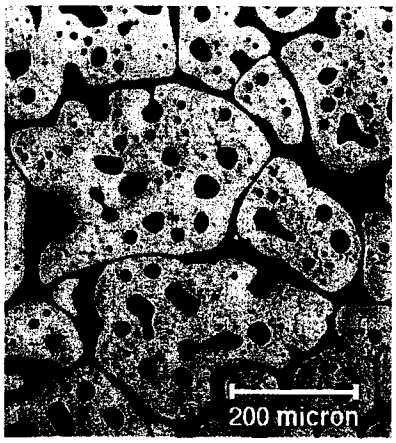

Fig. 5(d1) 585°C

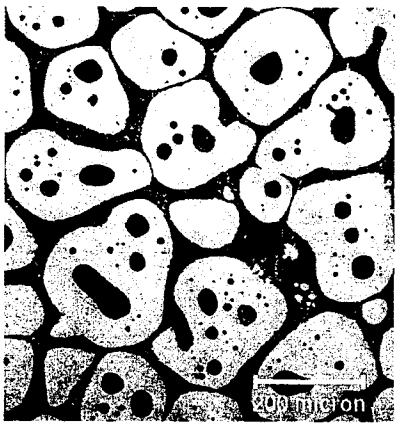

Fig. 5(e) 588°C

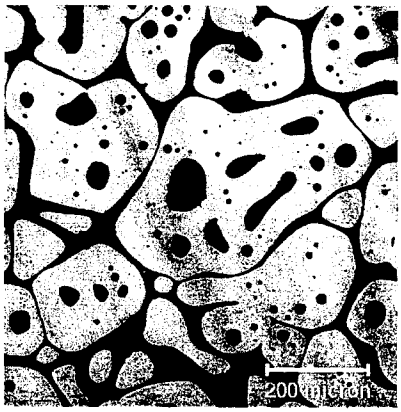

Fig. 5(e1) 588°C

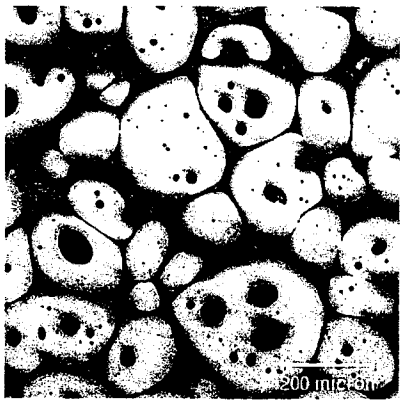

Fig. 5(f) 590°C

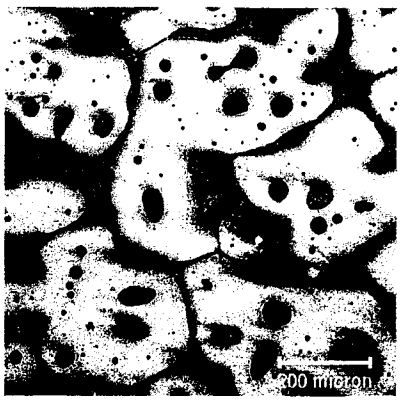

Fig. 5(f1) 590°C

Figure 5: Microstructure evolution of GR A356 billet as a function of temperature (heating rate: 49°C/min.), (d)-(f): samples taken from the periphery of the billet; (d1)-(f1): samples taken from the center of the billet.

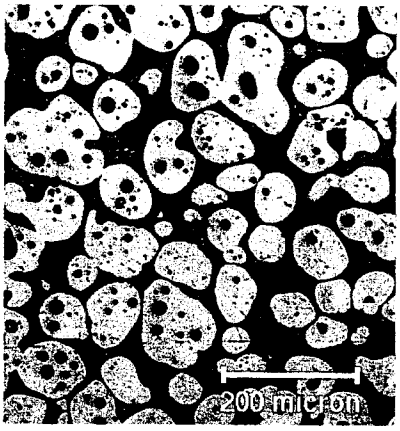

Fig. 6(a) 577°C

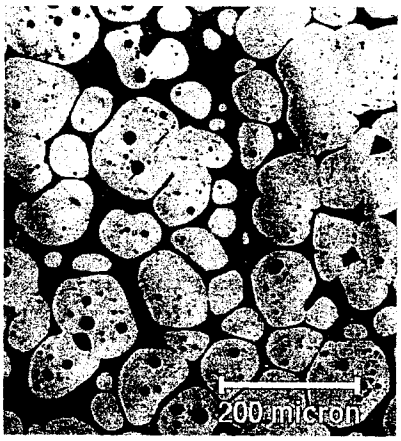

Fig. 6(a1) 577°C

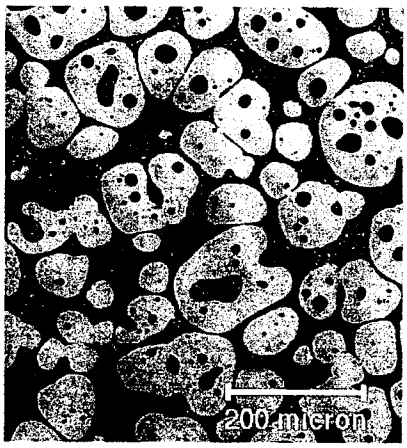

Fig. 6(b) 580°C

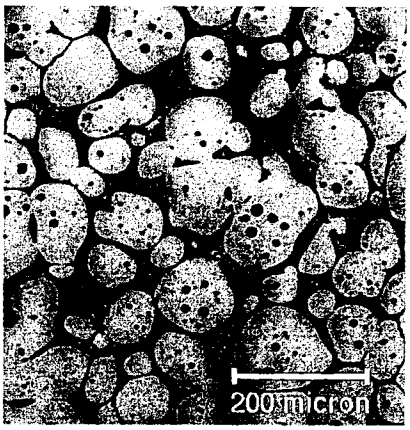

Fig. 6(b1) 580°C

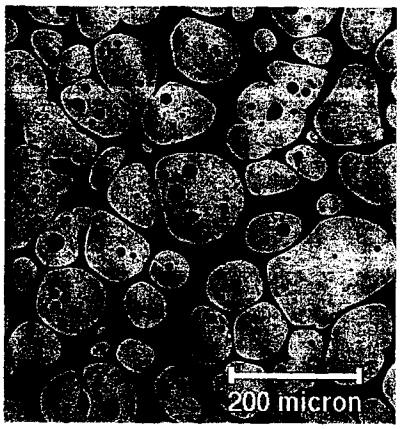

Fig. 6(c) 582°C

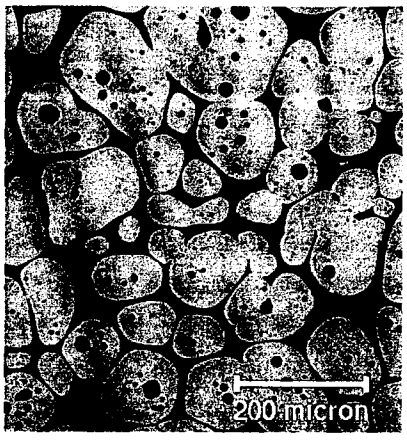

Fig. 6(c1) 582°C

Figure 6: Microstructure evolution of MHD A356 billet as a function of temperature (heating rate: 49°C/min.), (a)-(b): samples taken from the periphery of the billet; (a1)-(c1): samples taken from the center of the billet.

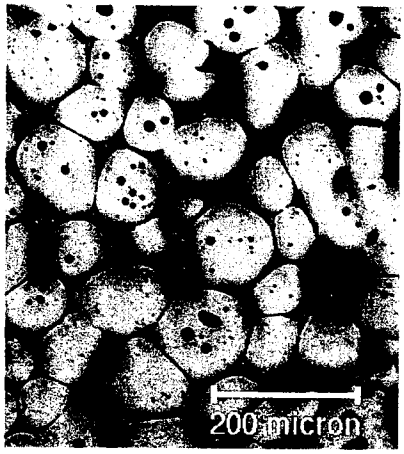

Fig. 6(d) 585°C

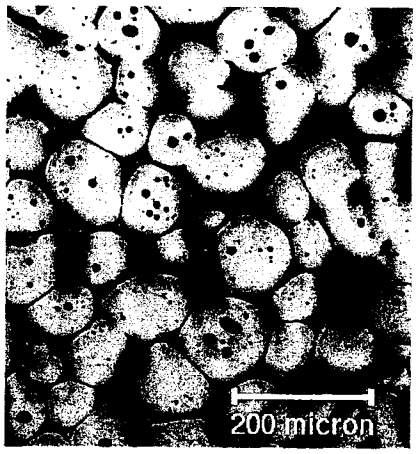

Fig. 6(d1) 585°C

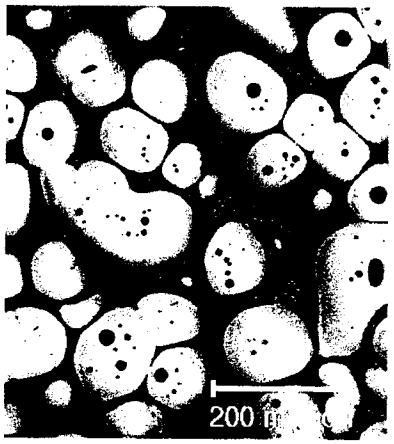

Fig. 6(e) 588°C

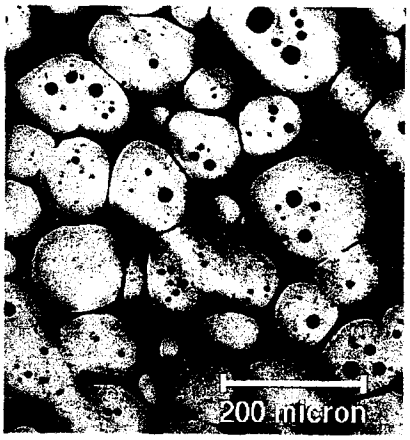

Fig. 6(e1) 588°C

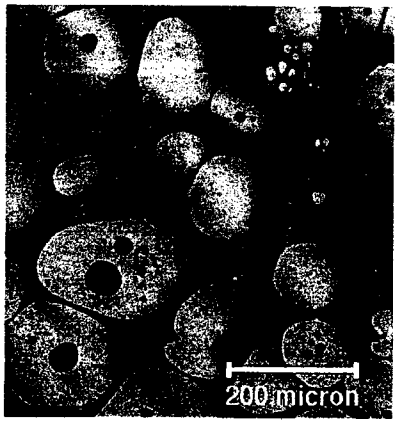

Fig. 6(f) 590°C

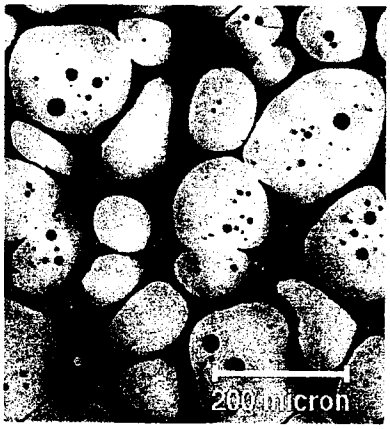

Fig. 6(f1) 590°C

Figure 6: Microstructure evolution of MHD A356 billet as a function of temperature (heating rate: 49°C/min.), (d)-(f): samples taken from the periphery of the billet; (d1)-(f1): samples taken from the center of the billet.

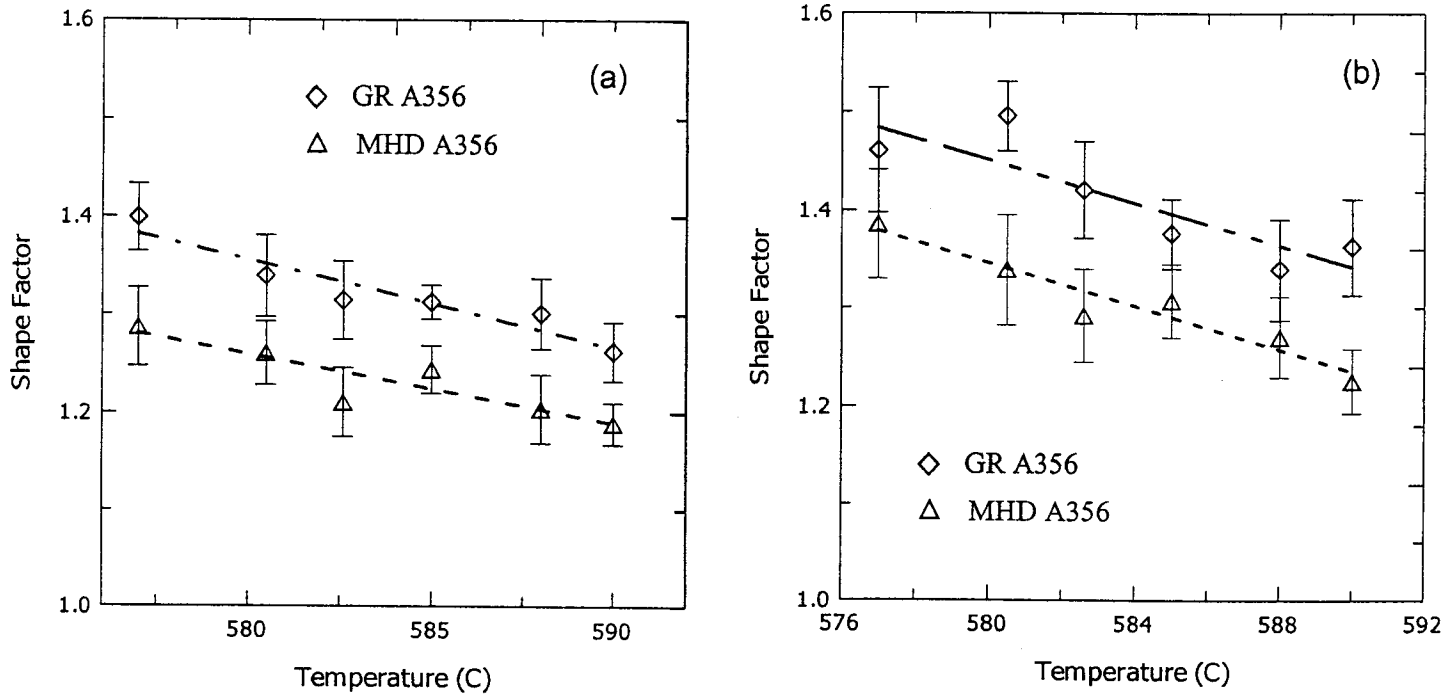

Figure 7: Evolution of shape factor as a function of temperature (heating rate: 49°C/min.), (a) at billet periphery; and (b) at billet center.

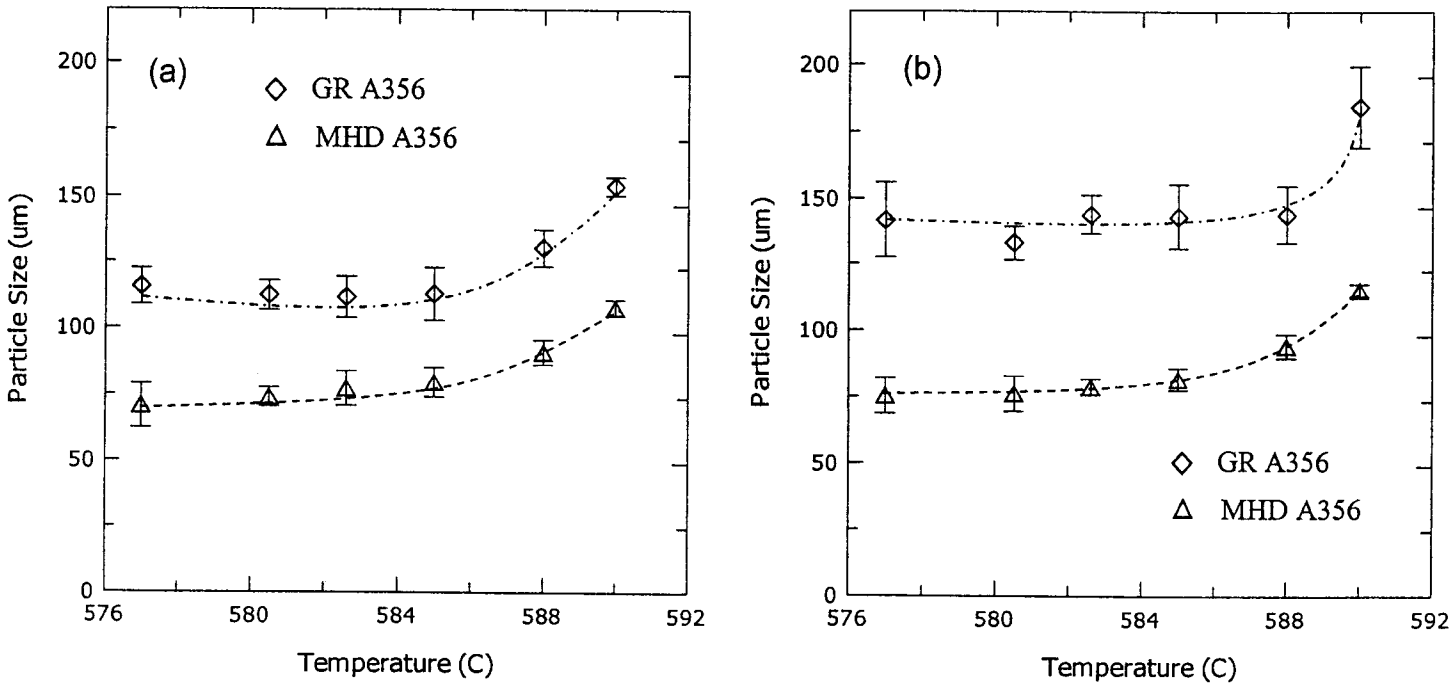

Figure 8: Evolution of particle size as a function of temperature (heating rate: 49°C/min.), (a) at billet periphery; and (b) at billet center.

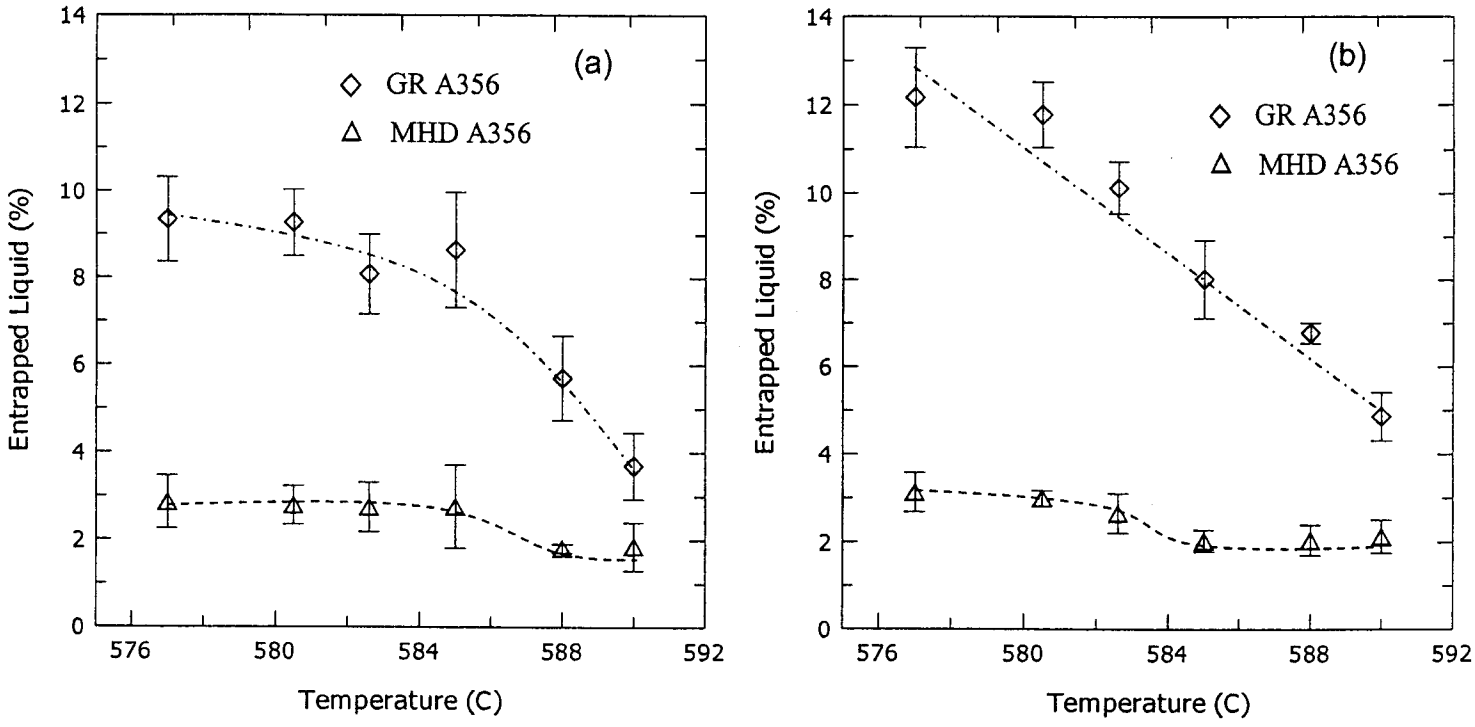

Figure 9: Evolution of entrapped liquid as a function of temperature (heating rate: 49°C/min.), (a) at billet periphery; and (b) at billet center.

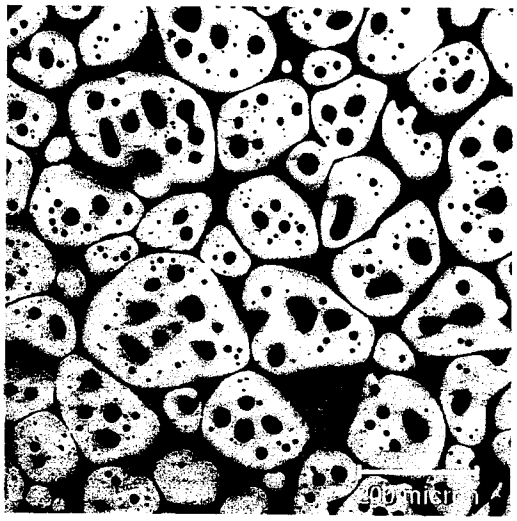

Fig. 10(a) 578°C

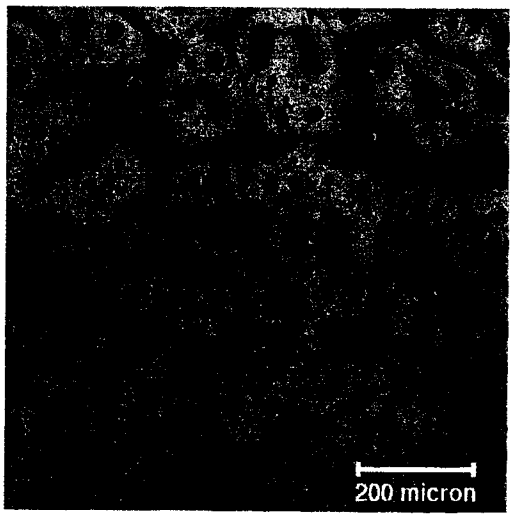

Fig. 10(a1) 578°C

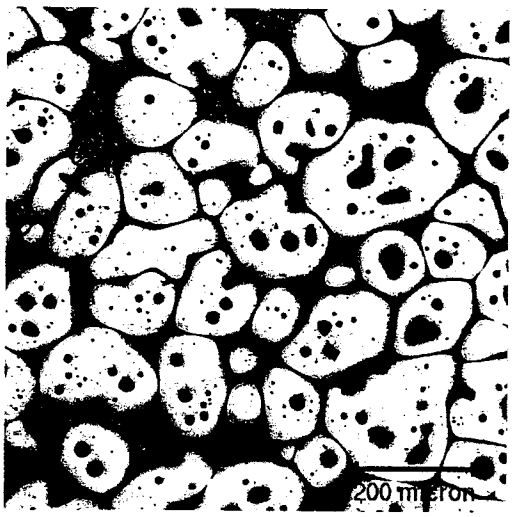

Fig. 10(b) 580°C

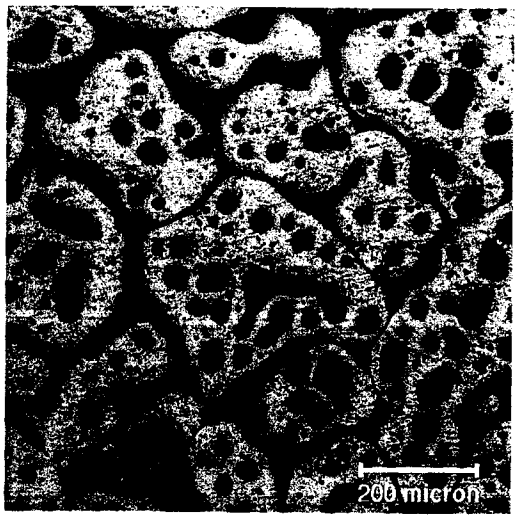

Fig. 10(b1) 580°C

Figure 10: Microstructure evolution of GR A356 billet as a function of temperature (heating rate: 4°C/min.), (a)-(b): samples taken from the periphery of the billet; (a1)-(b1): samples taken from the center of the billet.

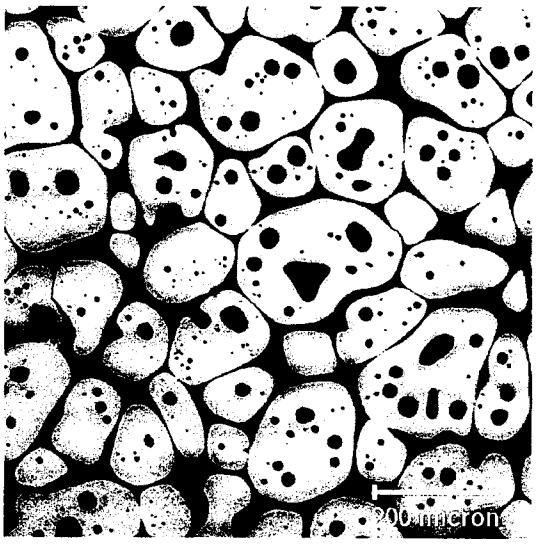

Fig. 10(c) 582°C

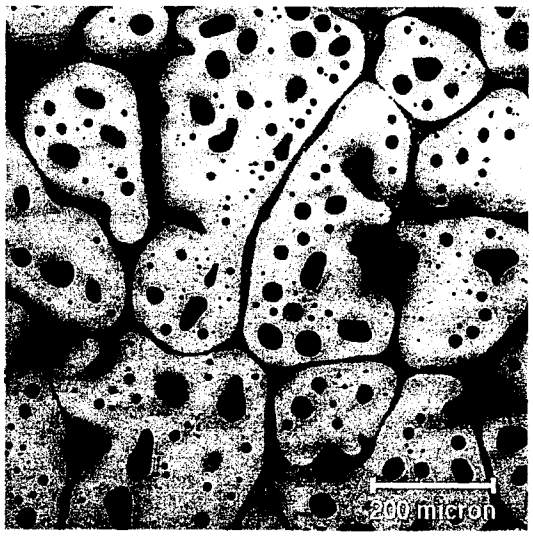

Fig. 10(c1) 582°C

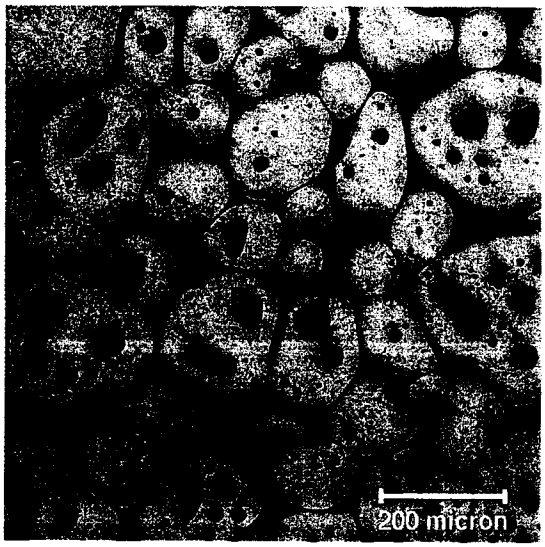

Fig. 10(d) 585°C

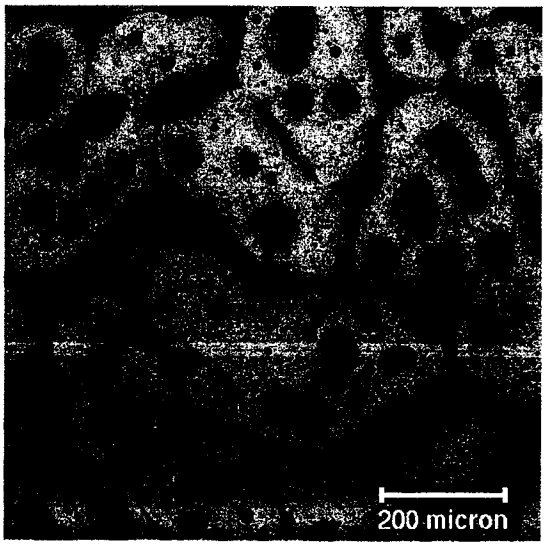

Fig. 10(d1) 585°C

Figure 10: Microstructure evolution of GR billet as a function of temperature (heating rate: 4°C/min.), (c)-(d): samples taken from the periphery of the billet; (c1)-(d1): samples taken from the center of the billet.

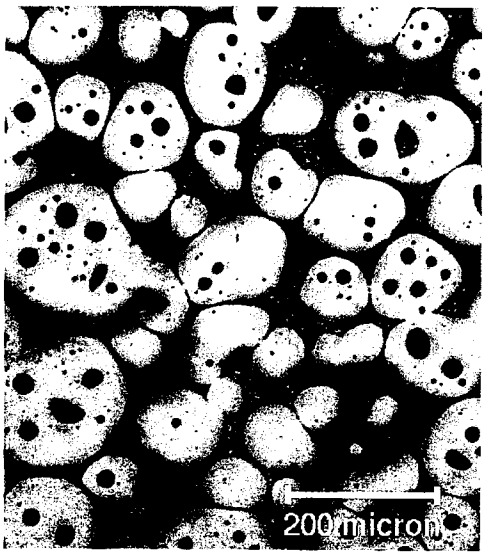

Fig. 11(a) 578°C

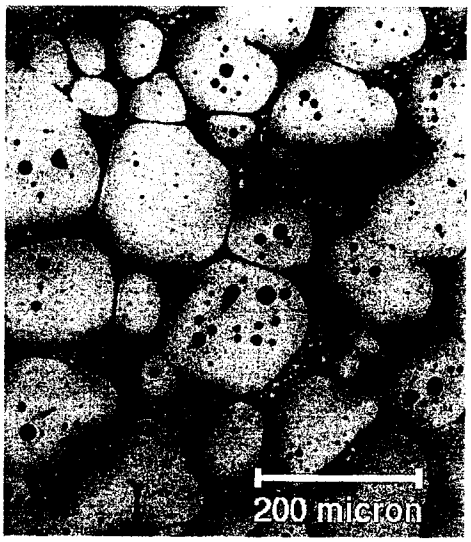

Fig. 11(a1) 578°C

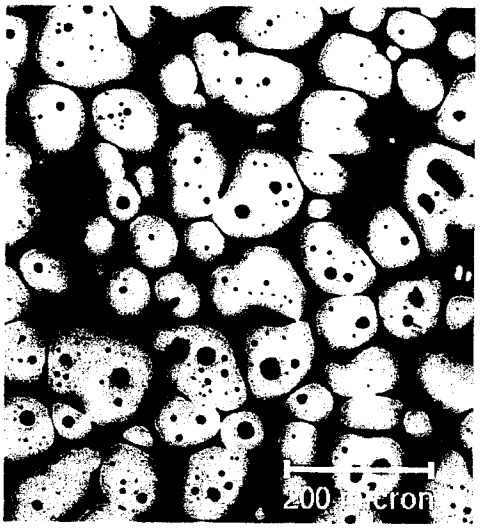

Fig. 11(b) 580°C

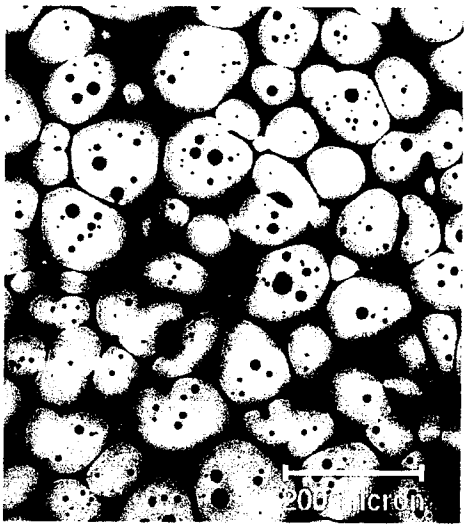

Fig. 11(b1) 580°C

Figure 11: Microstructure evolution of MHD A356 billet as a function of temperature (heating rate: 4°C/min.), (a)-(b): samples taken from the periphery of the billet; (a1)-(b1): samples taken from the center of the billet.

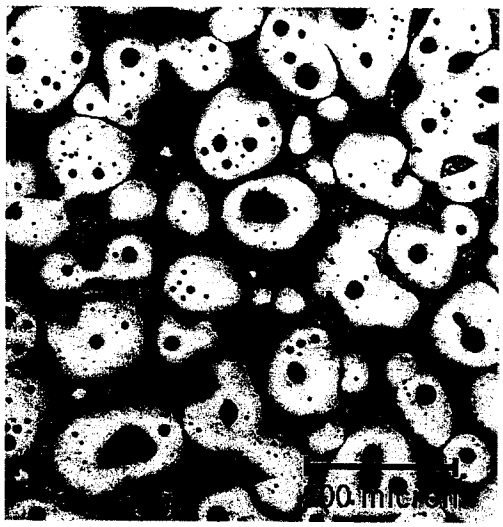

Fig. 11(c) 582°C

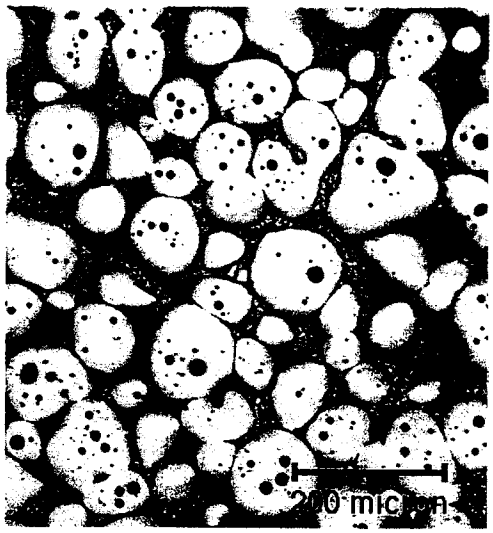

Fig. 11(c1) 582°C

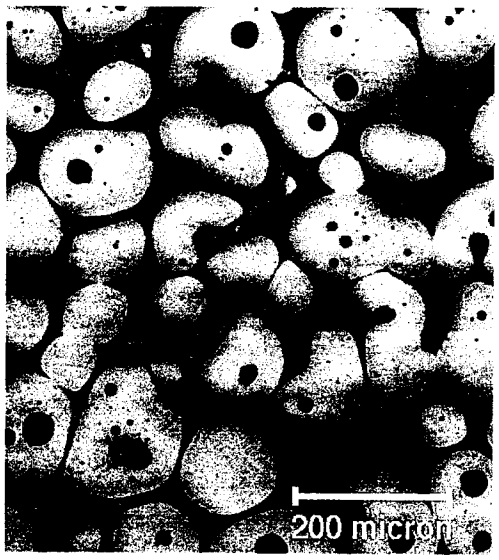

Fig. 11(d) 585°C

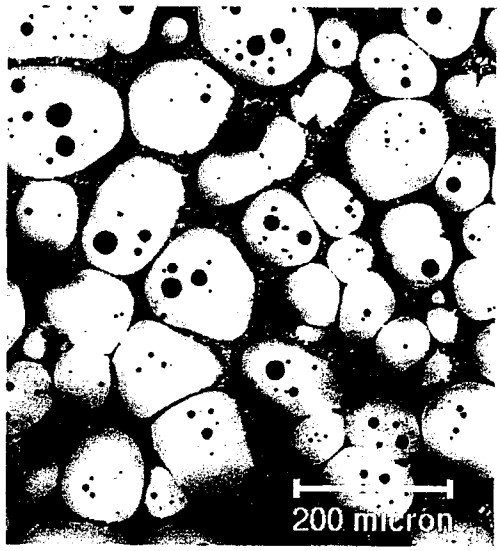

Fig. 11(d1) 585°C

Figure 11: Microstructure evolution of MHD A356 billet as a function of temperature (heating rate: 4°C/min.), (c)-(d): samples taken from the periphery of the billet; (c1)-(d1): samples taken from the center of the

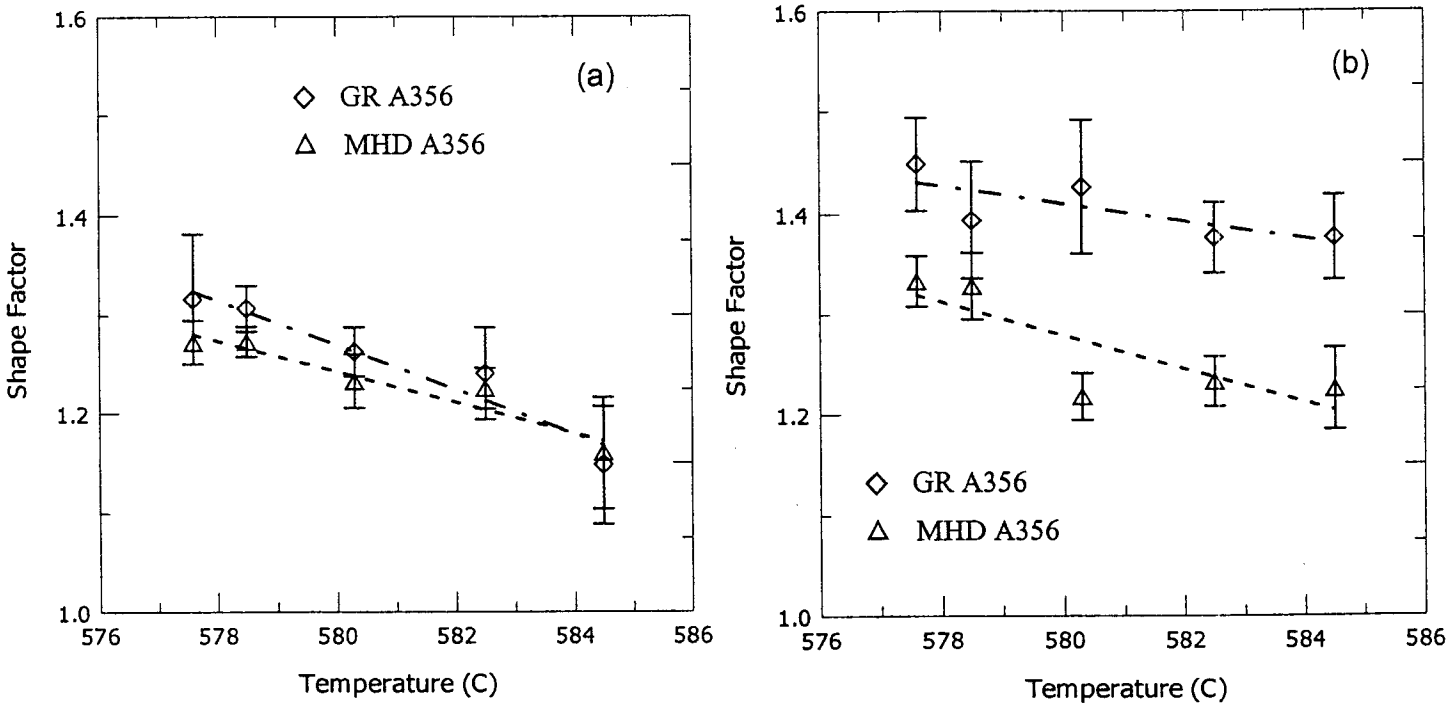

Figure 12: Evolution of shape factor as a function of temperature (heating rate: 4°C/min.), (a) at billet periphery; and (b) at billet center.

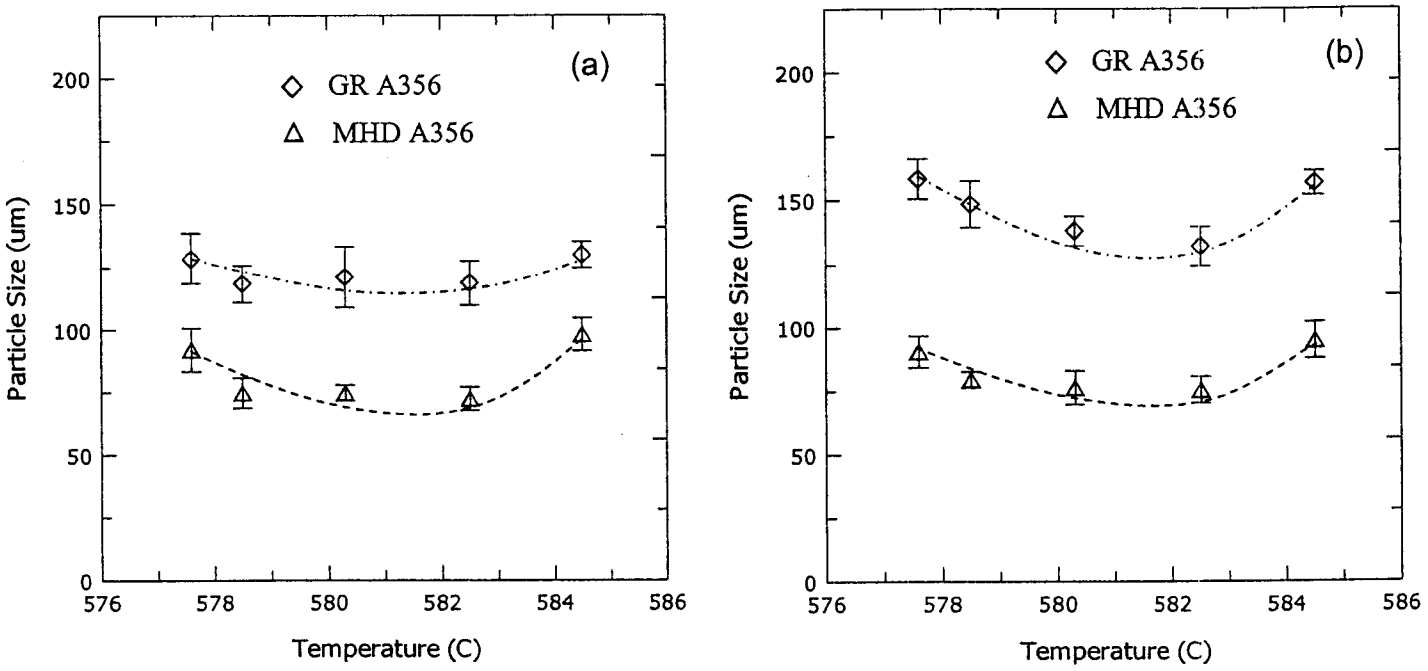

Figure 13: Evolution of particle size as a function of temperature (heating rate: 4°C/min.), (a) at billet periphery; and (b) at billet center.

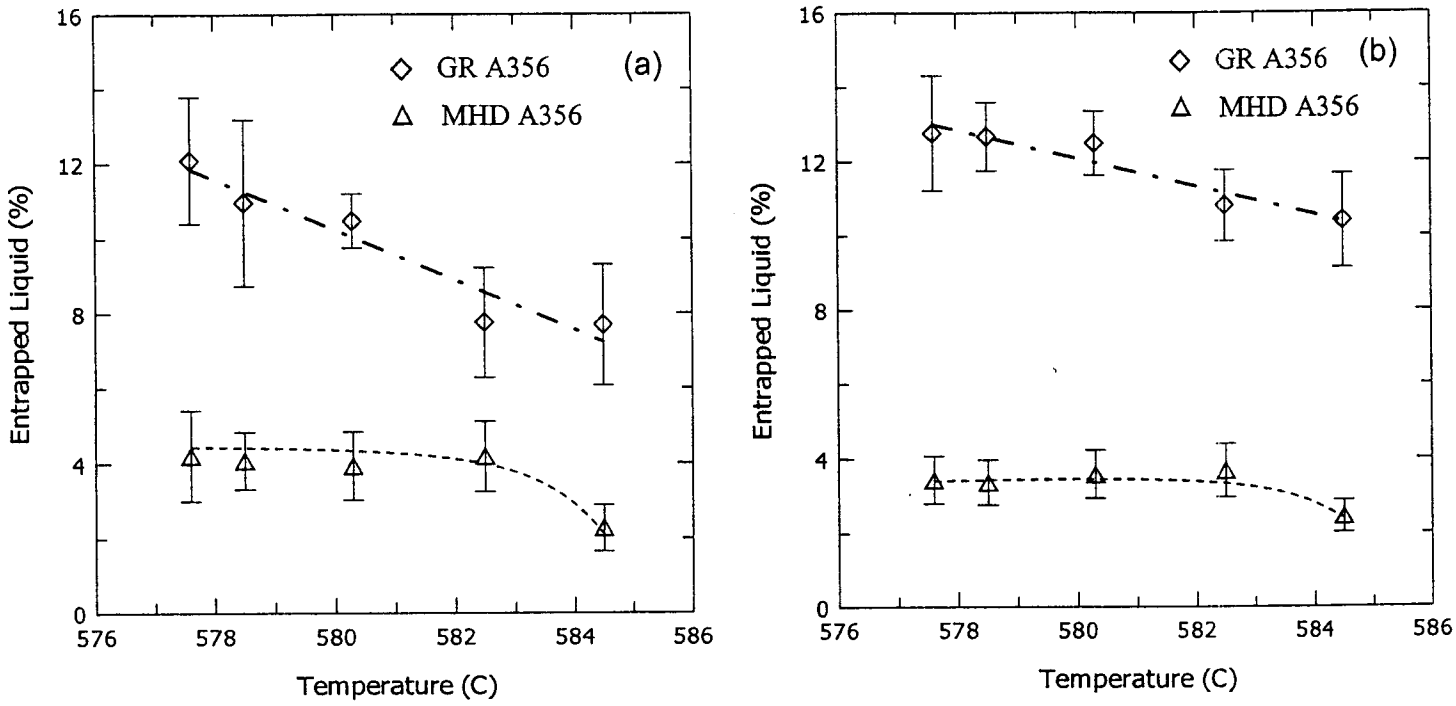

Figure 14: Evolution of entrapped liquid as a function of temperature (heating rate: 4°C/min.), (a) at billet periphery; and (b) at billet center.

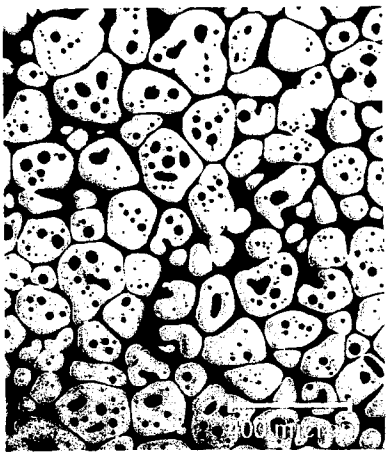

Fig. 15(a) 2 min.

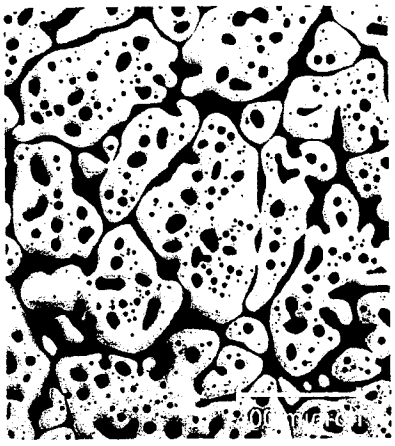

Fig. 15(a1) 2 min.

Fig.15(b) 4 min.

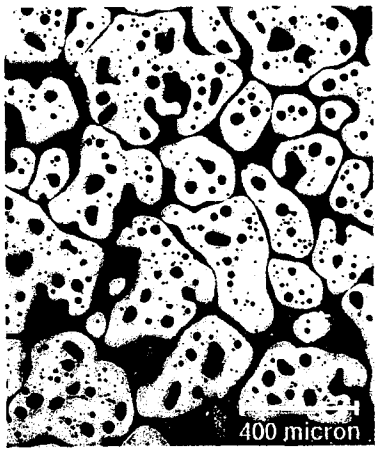

Fig. 15(b1) 4

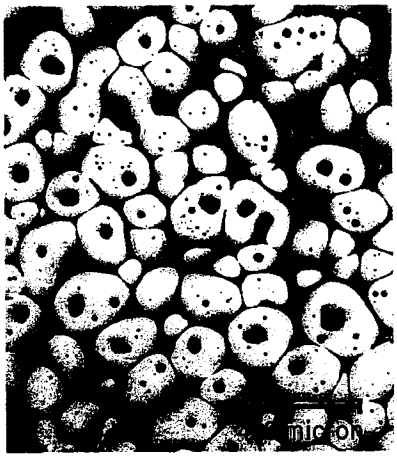

Fig. 15(c) 32 min.

Fig. 15(c1) 32 min.

Figure 15: Microstructure evolution of GR A356 billet as a function of isothermal time at 580°C, (a)-(c): samples taken from the periphery of the billet; (a1)-(c1): samples taken from the center of the billet.

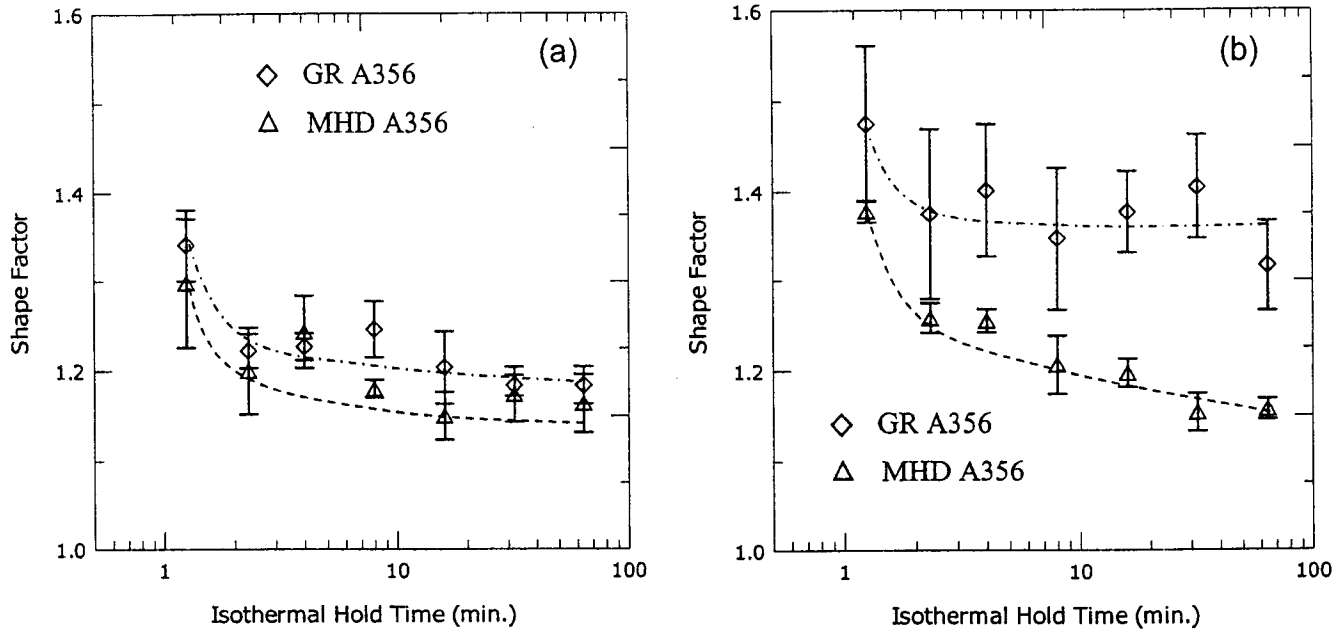

Figure 16: Evolution of a shape factor as a function of isothermal time at 580°C, (a) at billet periphery; and (b) at billet center.

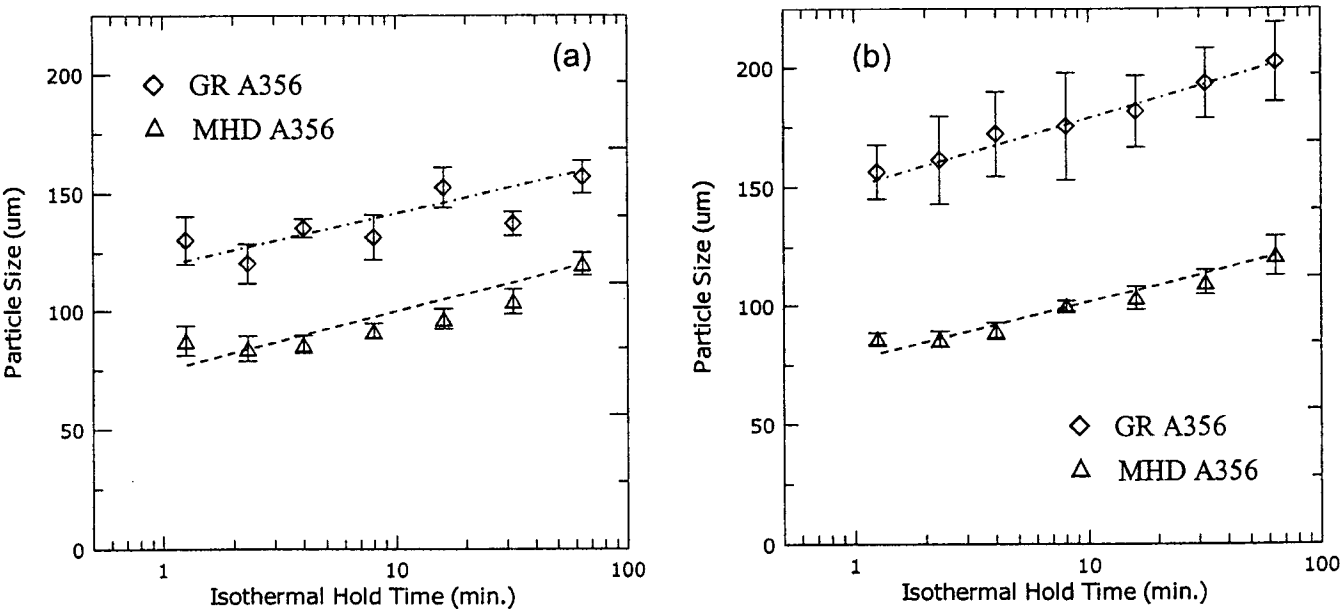

Figure 17: Evolution of particle size as a function of isothermal time at 580°C, (a) at billet periphery; and (b) at billet center.

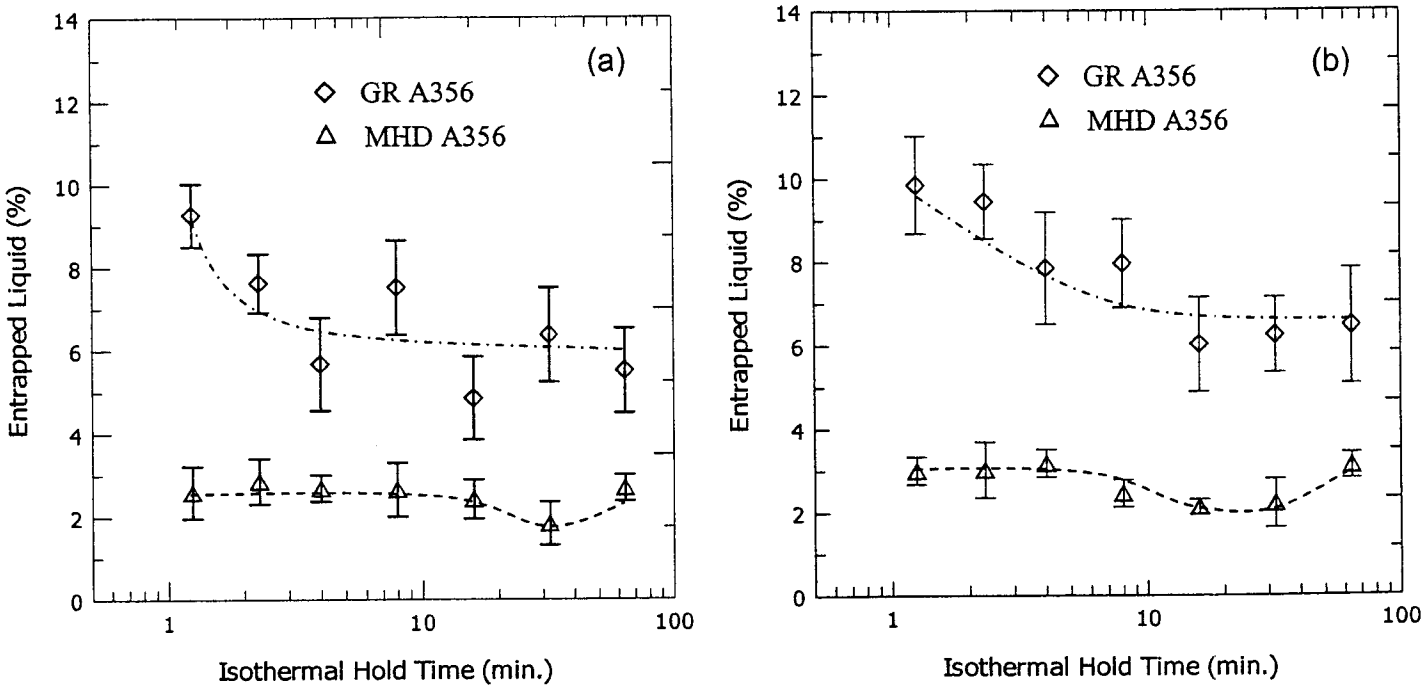

Figure 18: Evolution of entrapped liquid as a function of isothermal time at 580°C, (a) at billet periphery; and (b) at billet center.

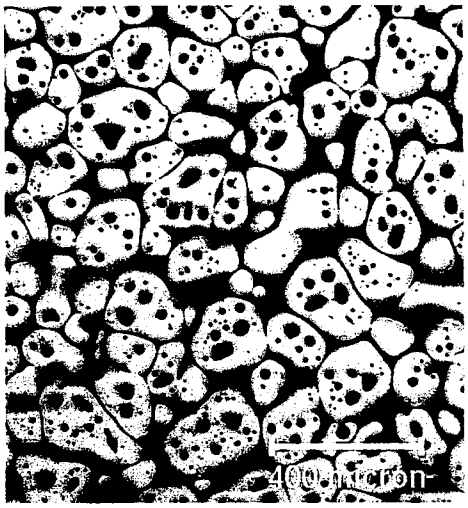

Fig. 19(a)
GR A356 at the edge

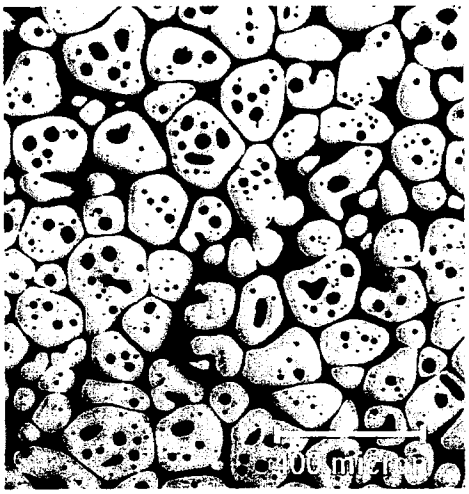

Fig. 19(b)
GR A356 at the center

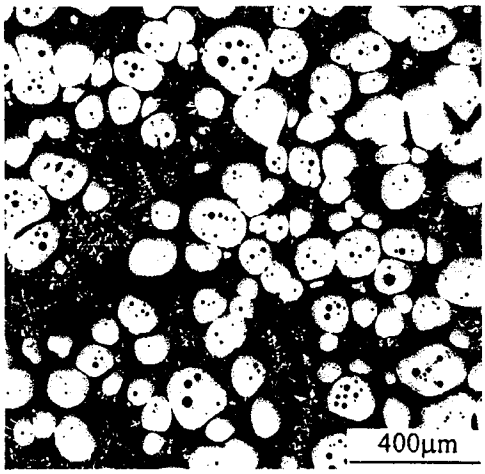

Fig. 19(c)
MHD A356 at the edge

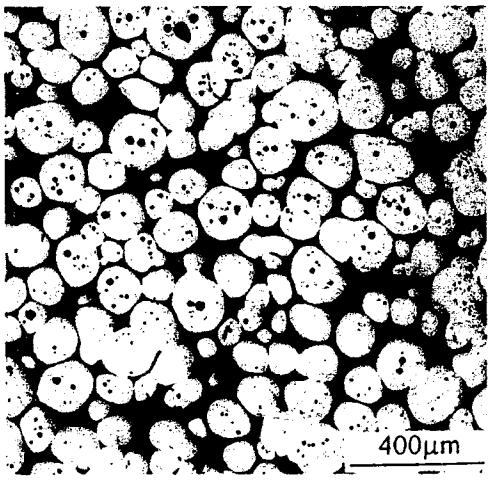

Fig. 19(d)
MHD A356 at the center

Figure 19: Microstructure of compressed GR A356 and MHD A356 alloy samples at different locations (temperature: 580°C; shear rate: $5\times10^{-3}s^{-1}$).

Fig. 20(a)
GR A356 at the edge

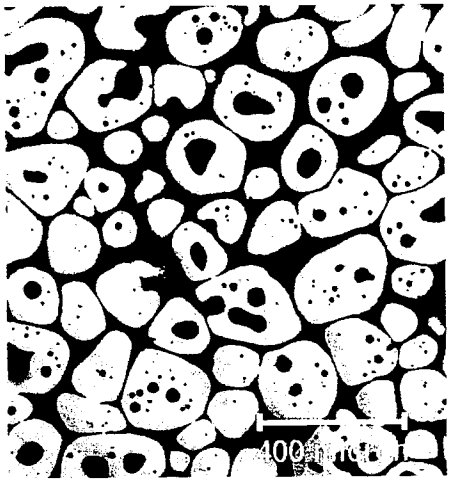

Fig. 20(b)
GR A356 at the center

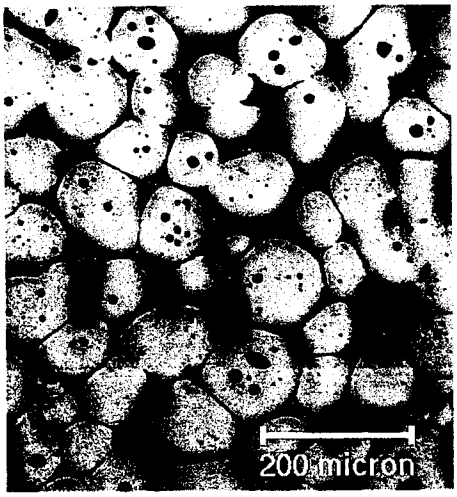

Fig. 20(c)
MHD A356 at the edge

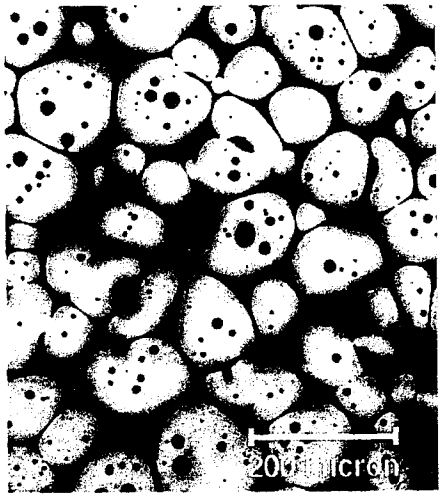

Fig. 20(d)
MHD A356 at the center

Figure 20: Microstructure of compressed GR A356 and MHD A356 alloy samples at different locations (temperature: 585°C; shear rate: $10^3 s^{-1}$).

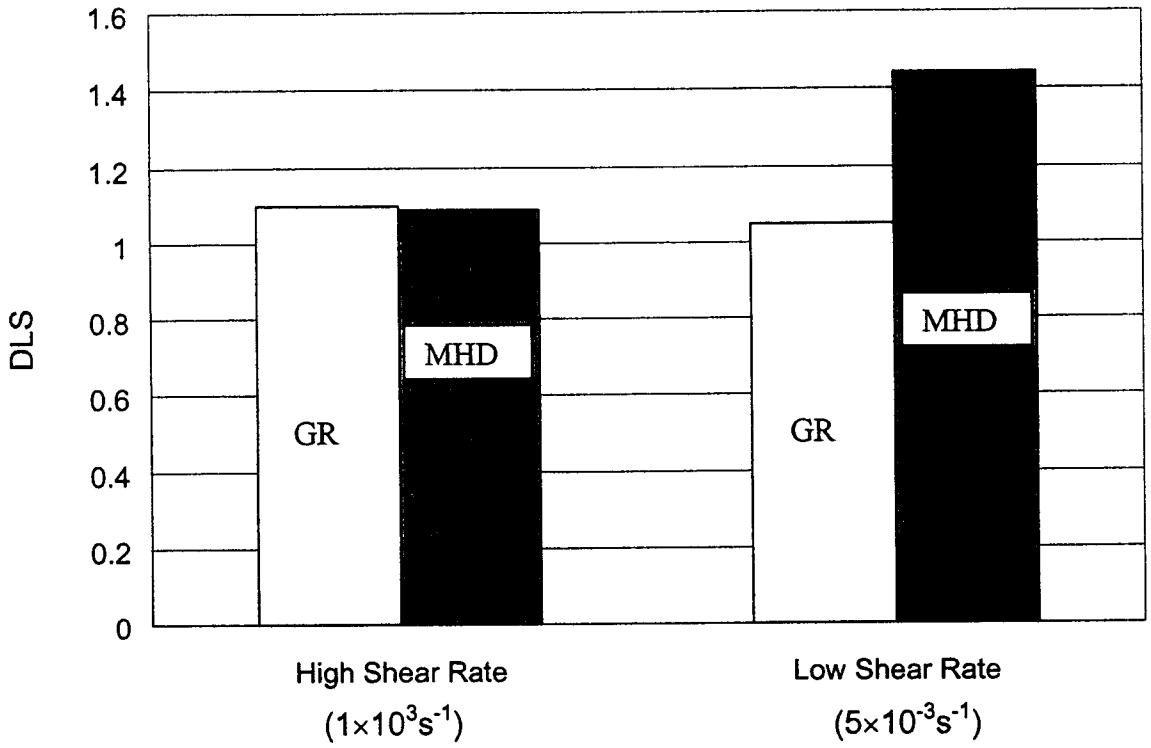

Figure 21: Image analysis results of compressed GR A356 and MHD A356 alloy samples at different shear rates. DLS is the degree of liquid segregation.

C. Time Dependent Rheology of Semi-Solid Alloys

TIME DEPENDENT RHEOLOGY OF SEMI-SOLID ALLOYS

Report PR-01-#1

Research Team:	Anacleto de Figueredo	508-831-6157	amf@wpi.edu
	Qingyue Pan	508-831-5790	qypan@wpi.edu
	Diran Apelian	508-831-5992	dapelian@wpi.edu
Focus Group:	Craig Bergsma	(Northwest Aluminum)	
	Stig Brusethaug	(Hydro Aluminum A.S.)	
	Alain Charbonnier	(Aluminum Pechiney)	
	Karuppa Chinnathamba	(Citation Aluminum)	
	Tom DeJohn	(Superior Industries International)	
	Michel Garat	(Aluminum Pechiney)	
	Vincent Genise	(Citation Aluminum)	
	John Jorstad	(JLJ Technologies)	
	John Miller		
	Rod Riek	(Harley-Davidson Motor)	
	Jim Van Wert	(Amcast)	

PROJECT STATEMENT

Objectives

The main objectives of this work are:

1. Continue the investigation of the flow behavior or semi-solid metals under experimental conditions that better simulate the flow of SSM slurries into molds during forming processes;
2. Correlate SSM structures with viscosity;
3. Determine shear stress-shear rate curves during rapid shear rate transients and establish the operating regime for shear thinning versus shear thickening;
4. Investigate the yielding behavior in semi-solid metals.

Strategy

This work will build on the existing body of experimental data on the flow behavior of SSM metals and other thixotropic slurries, using rheological approaches that are better suited to these materials. A viscometric approach based on the rotating vane geometry will be used to measure the temporal dependence of both the shear rate and the viscosity of slurries subjected to constant shear stresses. An important advantage of this geometry is that it allows for an easier

determination of the conditions where secondary flows and instabilities occur. The previous phenomena make the true behavior of SSM slurries very difficult to detect with other geometries. In addition, the vane method has a number of advantages over Couette or plate techniques, including:

1. The material to be measured can be placed in the regions delimited by the vanes before it is heated into the semi-solid state; this results in far less disturbance, which is a significant factor with thyxotropic slurries, and may lead to conflicting results.
2. The gaps between the vane and the cup are larger, and artifacts arising from large particles are less important.
3. The slurry contained within the cylinder described by the rotating vane blades is assumed to move together with the vane as a solid body. This is important, since the boundary of the cylinder is located between layers of fluid and any yielding must occur within the fluid itself.
4. The possibility of carrying out constant stress experiments and correcting for inertial effects that arise during rapid transient experiments.

The expected outcomes from this work are:

1. Temporal viscosity measurements of SSM slurries for a range of applied shear stresses, with and without pre-shearing;
2. Qualitative and quantitative information on the flow behavior of semi-solid metals during and after very rapid changes in shear stress/shear rate, i.e., changes occurring over periods of time shorter than 100 ms.
3. Information on the yielding behavior of SSM slurries.

The above data are needed as input for WPI's work on mathematical modeling and simulation of semi-solid filling processes, in particular the data on material properties that are time and shear rate dependent

ACHIEVEMENTS THIS QUARTER

- The rotating vane rheometer to be used in this work has been developed by Dr. Nguyen at the University of Adelaide, in Australia. Contact and visitation by Dr. D. Nguyen of University of Adelaide here at MPI.

- Experimental procedures have been developed by MPI and Dr. Nguyen for MHD 357 alloys produced by ORMET.

- The experiments will be initiated during the 3rd week of April 2001.

CHANGES IN PROJECT STATEMENTS

- None

WORK PLANNED FOR NEXT QUARTER

- Analysis of preliminary experimental results of Dr. Nguyen
- Microstructural analysis of sheared samples at WPI
- Correlation of rheological observations with slurry microstructure
- Conduct constant shear stress experiments

OPERATIONAL SCHEDULE

	Jun 2001	Jul 2001	Aug 2001	Sep 2001
Instrument calibration; Development of experimental procedures for SSM alloys	■			
Constant shear stress experiments in the solid fraction range 0.4 – 0.5 MHD alloy 357		■	■	
Microstructural analyses	■	■	■	■

TIME-DEPENDENT RHEOLOGY OF SEMI-SOLID ALLOYS

A.M. de Figueredo, Q. Y. Pan, and D. Apelian
Metal Processing Institute (MPI)
WPI, Worcester, MA 01609 USA

1. Introduction

The flow of semi-solid metals has been the subject of many investigations and a general agreement has been reached regarding the behavior of these materials under steady state flow conditions.[1-3] However, these conditions do not apply to industrial forming operations.[2,4] Semi-solid metal forming takes place under highly transient conditions and over time scales that are smaller by orders of magnitude when compared to the typical duration of a steady state experiment.

In recent years, several attempts have been made to understand the transient flow behavior of semi-solid metals and to measure properties that are time and shear rate dependent.[3-7] Most of the reported work on transient flow behavior of semi-solid metals relies on rotational viscometry,[1-10] but alternative techniques have also been used, including capillary rheometry,[11] back extrusion[12] and rapid compression between parallel plates.[13,14] All these techniques suffer from serious drawbacks when used to investigate the behavior of structured fluids like semi-solid metals.

For example, viscometers with narrow gaps are frequently used to achieve near ideal flow conditions.[1,2] In doing so, the continuum hypothesis is not respected because characteristic flow lengths start to approach the size of the particles in the SSM slurry being tested.[15] When this occurs, the theoretical relations for a given geometry[16] are no longer valid or useful. Due to experimental artifacts and the difficulties in establishing true viscometric flow with semi-solid metals, the available experimental data on the time-dependent rheology of these fluids are conflicting. Under rapid, time-dependent deformation, both shear thinning and shear thickening behavior have been reported for SSM slurries.[4-6] The viscosity (or shear stress) response to rapid shear rate transients and the yield stress are examples of issues that still remain unresolved.[17]

The central objective of this work is to investigate the transient flow behavior of semi-solid metals using an approach that eliminates the drawbacks of the techniques mentioned above, particularly wall slip, flow separation and particle bridging. Specifically, this work will attempt to:

- Determine the flow behavior of SSM slurries under conditions of rapid deformation (tens of milliseconds), and
- Investigate the yielding behavior in SSM slurries.

A clear understanding of the flow behavior during rapid deformation and of the yielding of SSM slurries is critical for the efforts on mathematical modeling and simulation of SSM processing at WPI, as well as the general materials science community.

2. Experimental Approach

Vane Geometry and Rheometer

To avoid the experimental problems mentioned above, the "vane-in-a-cup" geometry was selected for this work.[18-21] This configuration, which consists of four blades connected to a spindle (Figure 1), is simply used as an attachment that can be made to fit an existing rheometer. The vane has several important advantages over other geometries commonly used for measurements of structured fluids,[20] like the cylindrical bob: 1) the vane can be inserted into the sample with minimum disturbance, which is a significant factor with thixotropic slurries; 2) the larger gaps between the blade tips and the cup virtually eliminate artifacts due to large particle size (gap bridging); 3) for a very shear thinning, power-law fluid (a fluid with a power law index less than 0.5), the fluid within the cylinder circumscribed by the vane blades moves together with the vane as a solid body. In this case, the stream lines around the vane are circular, the boundary of the cylinder occurs between layers of fluid and <u>any yielding must occur within the fluid itself</u>.[20] This is, perhaps, the most important advantage of the vane geometry over other configurations.

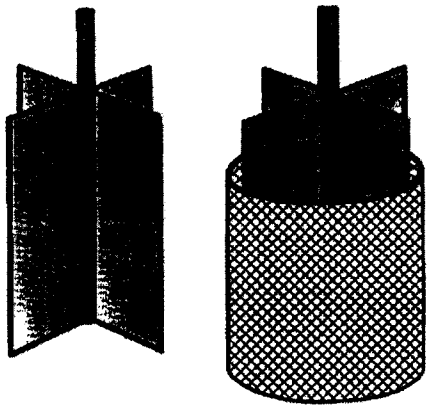

Figure 1. Illustration of the vane-and-cup geometry selected for the present work.

The proposed vane assembly can be used in combination with either stress or shear rate controlled rheometers.[17] The thickness and height of the vanes are, respectivelly, 2.82 mm and 38.2 mm. The internal diameter and the height of the cup are 35.1 mm and 76.4 mm, respectively. Figure 2 shows the controlled stress rheometer that will be used for this work in conjunction with the vane assembly at the University of Adelaide.

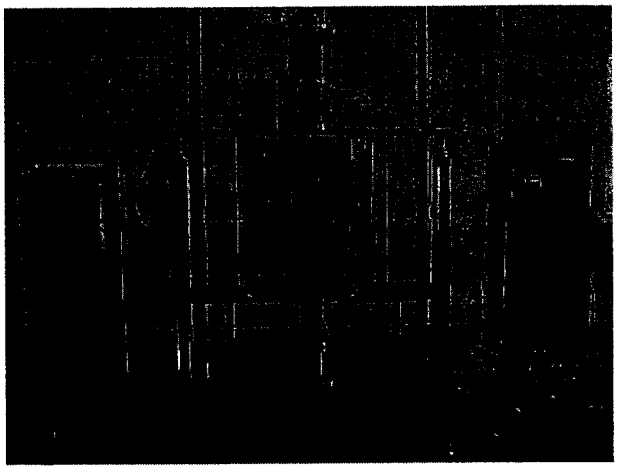

Figure 2. View of the high-temperature (1300°C) rheometer used in the experiments. This rheometer was specially designed for coal ash melts and can be used for any molten material, including SSM slurries. Courtesy of Dr. Q. D. Nguyen, University of Adelaide.

According to Barnes and Dzuy,[21] the formation of vortices behind the blades is likely to occur. The extra dissipation of energy associated with the vortices may produce viscosity measurements that are too high. This problem is common for low-viscosity fluids, but less likely to occur with the viscous SSM slurries, especially under the experimental conditions planned for this work.

SSM Slurry Formation

The slurries to be measured will be formed in the cup by rapid reheating of SSM feedstock. Figure 3 illustrate the sample loading procedure that was devised to minimize or completely eliminate structure disturbances that would inevitably result if the blades were to be inserted in the slurry. Such disturbances make it difficult to achieve reference states for the slurry. Reproducible measurements are very hard to obtain without a well-defined reference state. In the proposed procedure, 34-mm diameter cylinders are machined from as-received billets and split into four sections. The vane is positioned in the cup and the four sections are loaded into the spaces between the vane blades, as shown in Figure 3.

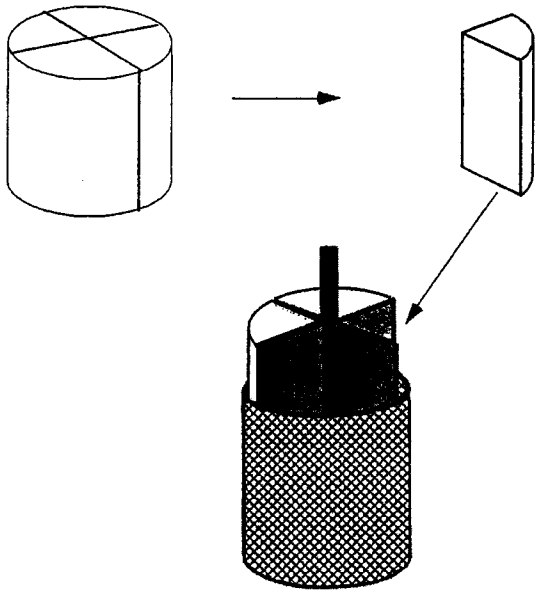

Figure 3. Sample loading procedure to enable the measurement of undisturbed SSM slurry structures.

Materials To Be Investigated

The materials for this investigation consist initially of MHD feedstock, and subsequently, of grain-refined and MIT-process feedstock. The MHD material was produced by ORMET and the grain-refined and MIT-type feedstock will be prepared at WPI and at MIT. The microstructure of the MHD feedstock is shown in Figure 4. Materials processed by different routes will produce slurries of varying particle morphology and entrapped liquid content. This will enable a quantitative evaluation of the effects of the previous variables on both the viscosity and the flow behavior of the slurry.

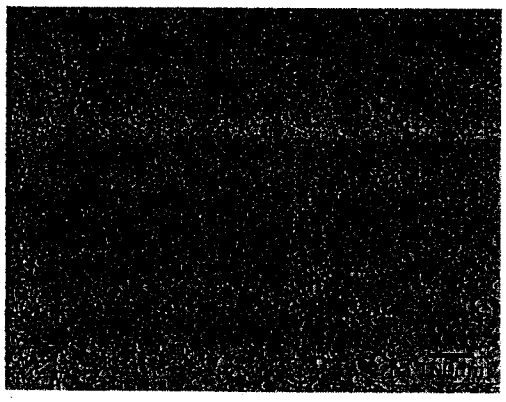

Figure 4. Microstructure of the MHD feedstock used in this work. Origin: ORMET, USA.

3. Planned Experiments

Rheology experiments will be carried out at the laboratory of Dr. Dzuy Nguyen, University of Adelaide, in Australia. Analyses of samples before and after rheological tests will be performed at WPI, including the structural evolution studies.

Preliminary experimentation will begin in the third week of April 2001 and will assess experimental issues of relevance for the planned work, including:

- Wall slip effects and flow separation;
- Maximum shear stress/shear rate that will cause secondary flows or instabilities;
- Achievement of a reference state for the slurry;
- Ability to impose rapid shear rate transients (ideally as rapid as a few tens of ms) by means of either a step increase or decrease in shear rate;
- Ability to measure the slurry response during the rapid shear rate transients (fast data acquisition rates);
- Inertial effects during rapid transients;
- Ability to gas quench and recover samples after a given shear rate history;
- Achievement of shear rates in the range 100 – 1000 s^{-1}.

Experiments will be carried out at constant stress (torque) and constant shear rate and will include transient shear rate measurements and yield stress measurements. Semi-solid forming conditions will be simulated by means of constant stress experiments. These experiments have been developed by Nguyen and applied to the investigation of structured fluids such as bentonite suspensions, which are also time and shear rate history dependent. The methodology consists of pre-shearing the samples at a constant stress for pre-determined periods of time to ensure that the same initial condition (reference state) is achieved before the measurements. These measurements may alloy extraction of information on the kinetics of structure breakdown and structure formation.

Typical results of constant stress experiments with the rotating vane are presented in Figure 5 and are from measurements of bentonite suspensions.[17] In Figure 5, the shear rate of a bentonite suspension was measured at constant imposed shear stresses. The measurement at each shear stress was made immediately after the suspension had been pre-sheared for 60 s at 26 Pa. The observation of Figure 5 reveals that at very short times after start up, the shear rate is relatively insensitive to the applied shear stress. As the time of shear increases, the shear rate steadily decreases; the lower the applied shear stress, the faster the shear rate decreases. This behavior, if verified for semi-solid metals, may have important practical consequences for the mathematical modeling of these fluids.

The plot of Figure 5, however, does not contain data points that describe the transition from the high pre-shearing stress of 26 Pa to the imposed stresses shown. It is the objective of this work to investigate the slurry behavior in that region, i.e., immediately

after the stress has been changed from a high to low value. Such experiments will last much less than one second and are the relevant ones for the present study. The behavior at longer times (tens of seconds) is not relevant for modeling of semi-solid metal forming.

Quenched slurries will be investigated before and after tests. Slurries will be characterized by image analysis, with emphasis on particle morphology and fraction of entrapped liquid.

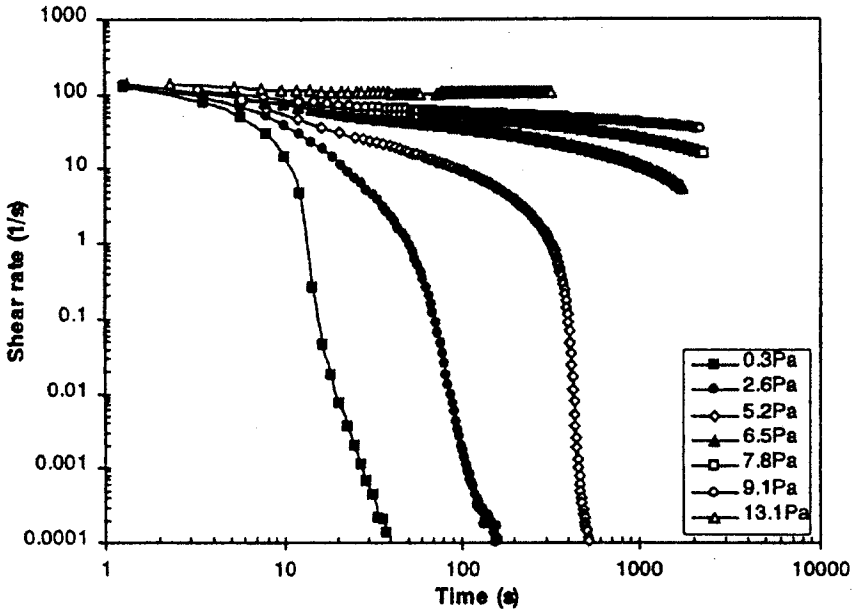

Figure 5. Typical results of constant stress experiments on a bentonite suspension.[17]

4. References

1. M. C. Flemings, Met. Trans. 22B (1991), 269-293
2. D. H. Kirkwood, Int. Mat. Rev. 39 (5) (1994), 173-189
3. H.-K. Moon, (Ph.D. thesis, M.I.T., 1990)
4. A. M. de Figueredo, A. Kato, and M. C. Flemings, Met. Sci. and Tech. 18 (2) (2000), 32-36
5. P. Kumar, C. L. Martin, and S. Brown, Acta Metall. Mater., 42 (11) (1994), 3595-3602
6. P. Kumar, C. L. Martin, and Stuart Brown, Metall. Trans. 24A (1993), 1107-1116
7. C. J. Quaak and W. H. Kool, Mater. Sci. Eng., A188 (1994) 277-282
8. M. Mada, and F. Ajersch, Mat. Sci. Eng. A212 (1996), 157-170
9. T. Z. Kattamis and T. J. Piccone, Mater. Sci. Eng. A 131 (1991), 265-272
10. L. S. Turng, and K. K. Wang, J. Mater. Sci. 26 (1991), 2173-2183
11 F. C. Yee, Ph.D. thesis, Nanyang Technical University, Singapore, 1999)
12. W. R. Loué, M. Suéry and J. L. Querbes, "Microstructure and Rheology of Partially Remelted AlSi-Alloys," Proc. 2nd Int. Conf. On Semi-Solid Processing of Alloys and Composites, Cambridge, (1992), 266-275

13. P. Kapranos, D. H. Kirkwood, and M. R. Barkhudarov, "Modeling of Structural Breakdown During Rapid Compression of Semi-Solid Alloy Slugs," Proc. 5th Int. Conf. On Semi-Solid Processing of Alloys and Composites, Boulder (1998), 11-1912.
14. J. Yurko and M. C. Flemings, "A Drop Forge Viscometer for Semi-solid Alloys", Proc. Of the 6th. Intl. Conf. On Semi-Solid Proc. Of Alloys and Composites, Turin, Italy, Sep. 27-29, 2000, G. L. Chiarmetta and M . Rosso, eds, Edimet, Bescia, Italy, pp. 681-686
15. P.Coussot, Mudflow Rheology and Dynamics, (Rotterdam: A.A. Balkema, 1997), 69-92
16. C. W. Macosko, Rheology, Principles, Measurements, and Applications, (New York, NY: Wiley-VCH, Inc, 1994), 217-219
17. Q. D. Nguyen, P. Coussot, T. Huynh, and D. Bonn, "The Time-Dependent Rheology of Colloidal Suspensions", in preparation.
18. Q. D. Nguyen and D. V. Boger, J. Rheology 27 (4) (1983), 335-347
19 Q. D. Nguyen and D. V. Boger, J. Rheology 29 (3) (1985), 321-349
20. H. A. Barnes and J. O. Carnali, J. Rheology 34 (6) (1990), 841-867
21. H. A. Barnes and Q. D. Nguyen, "The Use the Rotating Vane Geometry for Non-Newtonian Liquids – A review", in preparation.

04/20/01

D. Optimization of Heat Treatment Conditions for Semi-Solid 357 Alloy

OPTIMIZATION OF HEAT-TREATMENT CONDITIONS FOR SEMI-SOLID 357 ALLOY

Report PR-01-#1

Research Team:	Jason Astle	(508) 831 5681	clyde@wpi.edu
	Diran Apelian	(508) 831 5992	dapelian@wpi.edu
	Qingyue Pan	(508) 831 5790	qypan@wpi.edu

Focus Group:	John Miller	
	Craig Bergsma	(Northwest Aluminum)
	Stig Brusethaug	(Hydro Aluminum A.S.)
	Karuppa Chinnathamba	(Citation Aluminum)
	Vincent Genise	(Citation Aluminum)
	Tom DeJohn	(Superior Industries International)
	Michel Garat	(Aluminum Pechiney)
	Alain Charbonnier	(Aluminum Pechiney)
	John Jorstad	(JLJ Technologies)
	Rod Riek	(Harley-Davidson Motor)
	Jim Van Wert	(Amcast)

PROJECT STATEMENT

Objectives

- Determine the heat treatment response of SSM cast Al 357 alloy in comparison to conventionally cast A356 and A357 alloys.
- Provide experimental data that can be used to optimize the industrial practice.
- Characterize the microstructure evolution of SSM 357 alloy during heat treatment, and measure the mechanical properties subsequent to heat treatment.
- Identify the optimum conditions for heat-treating SSM 357 alloy.

Strategy

- A Taguchi design of experiments consisting of two L9 Orthogonal arrays was used in order to establish the optimum solution heat-treatment and aging conditions. The conditions tested are presented in ***Appendix A*** - attached.

- Mechanical testing was performed on all treated samples, SSM 357 and conventionally cast A356 and A357, in order to quantify strength and ductility of samples due to difference in treatment conditions.

- Image analysis was performed in order to characterize the evolution of microstructure in SSM 357 samples. Analysis of the fracture surfaces of test bars was performed using scanning electron microscopy (SEM) in order to identify the mode of failure.

Achievements This Quarter

During this quarter, heat treatment has been performed along with mechanical property testing of all samples. Microstructure analysis of the samples is currently being performed.

- A comparison of the tensile test results for SSM 357 alloy and conventionally cast A356 and A357 alloys is presented in ***Appendix B***. It can be seen from the results presented in ***Appendix C*** that SHT times between 1 – 6 hours, for all three heat treatment temperatures examined, result in excellent tensile strength and ductility. In order to better represent the tensile data, the quality index was calculated. Although it was found possible to increase the strength and ductility of the material by using longer heat-treatments, the benefit in mechanical properties was not enough to justify the expense associated with longer heat treatment cycles.

- Analysis of Variance (ANOVA) was performed on the tensile strength data, and the % elongation data. It is evident from the analysis ***[Appendix D]*** that these properties are highly dependent on the aging time and temperature. One can also note from the ANOVA analysis with respect to the % elongation ***[Appendix E]*** that it tensile strength data are very dependent upon the solution heat-treatment conditions.

- Since the Taguchi method can only determine the optimum condition within the parameters selected for testing, it is possible that the real optimum condition would not be identified if the appropriate testing parameters were not initially selected. In order to identify the real optimum condition for maximum strength, ductility, and the combination of strength and ductility, the team decided to use an Advanced Neural Network Analysis technique (ANNA). With ANNA it is be possible to determine the optimum condition no matter what test parameters were initially selected.

- The trained ANNA results for the heat treatments performed in the Taguchi matrix are very close to the actual tensile data received. The trained values from the ANNA are presented in ***Appendix F***.

- Image analysis and SEM are currently being performed and the complete results and discussion will be presented in ACRC PR- 01- #2.

Changes in Project Statements

None

Work Planned for Next Quarter

- Complete the remaining image analysis and SEM work and characterize the evolution of the microstructure during the heat treatment cycle.
- Characterize the mode of failure during tensile testing.
- Validate the optimum conditions predicted by the ANNA.
- Document the mechanical and microstructure results in a final report.

Operational Schedule

All analysis and documentation will be completed by the end of May 2001. A final report will be issued.

Attachment A gives a summary of the methodology followed, the procedures utilized, and tabulated results.

Appendices A through F, also attached, give the detailed results.

ATTACHMENT A

Attachment A: METHODOLOGY, PROCEDURES, AND TABULATED RESULTS OF HEAT TREATING OF SEMI-SOLID 357 ALLOY

Methodology

The following is a breakdown, in chronological order, of the procedure that was followed for this experimental study.

◊ Phase I – Performed at ORNL (8/99-12/99)

- 72 samples cut from SSM Al 357 alloy in form of fuel rail castings
- Calibration of furnaces and quench tank
- Solution heat-treatment @ 540°C for 1,2,4, or 8 hours
- Quench in water held at 80°C
- Natural aging (incubation time) 18-24 hours
- Aging at 155, 165, 175°C for 2,3,4,6,12, or 16 hours

◊ Phase II – Performed at MPI (1/00 – present)

- Taguchi heat-treatment matrix consisting of 18 experimental runs
- Calibration of furnaces and quench
- Semisolid Al 357 samples taken from cast fuel rails and machined into rectangular tensile specimen.
- Solution heat-treatment @ 540, 545, 550° for 1,2,4,6,8,10 hours
- Quench in water held at 80°C
- Natural aging (incubation time) 24 hours
- Aging at 155, 165, 175°C for 2,4,6,8,12,16 hours
- Circular tensile specimen from permanent mold A356.2 and 357.2 undergone same heat treatment for purpose of comparison

◊ Phase III – Mechanical and Microstructural Analysis

- Tensile testing of all semisolid and permanent mold heat-treated samples
- SEM analysis of fracture surfaces of semisolid samples
- Image analysis of microstructure of semisolid samples
- Taguchi and ANN analysis of optimum conditions

Experimental Procedures

The experimental procedure for this study is broken down into three distinct phases. The first phase of the study is a preliminary heat-treatment experiment, while phase two was the final heat-treatment matrix, followed by the microstructural and mechanical analysis, phase three. These phases are discussed below.

Preliminary Heat Treatment Experiment (Phase I)

In order to justify the further experimentation of trying to find why a shorter heat treatment time was preferable for this semisolid aluminum 357 alloy, it was first necessary to see if it was a feasible goal. These preliminary tests are considered phase I.

The semisolid aluminum 357 material used in this experiment was provided by Madison-Kipp Co. in the form of as-cast fuel rails. All samples were cut from the corresponding cross section of the castings, which were all produced in the same manner, to ensure minimum variance between samples. The castings were cut into pieces 0.75cm thick and approximately 3 cm. long. The treatment apparatus was set up and calibrated to ensure quality results.

The hardness tests of the heat-treated samples were performed using a Brinell hardness machine. For the purpose of our tests on aluminum, a 10mm steel ball and a 500 kg load was the appropriate procedure. An indentation was made and the diameter was measured by using a 20x microscope with a millimeter scale in the sight of the scope. Once the samples were sufficiently treated and aged they would be given sufficient time to cool down and then hardness tested. Using the manual Brinell tester with a 10mm ball and 500 kg load, three indentations were made on each sample and measured with the 20x scope. The average of these three values was recorded and then graphed in order to make a visual comparison of the hardness effects of the different solution heat treatment and aging methods. The results of these hardness tests were presented in ACRC report 00-#1. These results showed that it was possible to obtain excellent hardness properties when SHT for 2 hours at 540°C along with an aging treatment at 175°C for 6 hours. From these results the team decided it was necessary to proceed with a more in-depth testing and evaluation of these heat treatments.

Final Taguchi Heat-treatment Matrix (Phase II)

The samples used for this heat-treatment matrix were again machined from SSM Al 357 fuel rail castings, provided by Madison-Kipp Co. Since a more in-depth analysis was to be performed, the samples were machined into rectangular tensile specimen of precise geometry. All of the machining of the samples was carried out courtesy of the Oak Ridge National Laboratory in Oak Ridge, Tennessee. For purposes of comparison samples were also cast from A356.2 and A357.2 material. These samples were permanent mold castings of circular tensile bars. The casting was

performed at the MPI/ACRC facilities in Worcester, MA. To ensure consistency between samples, all castings from each alloy were cast from the same melt. The melts were sufficiently degassed to a hydrogen content of less than 0.08% before being cast, to ensure high integrity.

In the interest of time, a Taguchi design of experiments was used to set up the new heat-treatment matrix. The main purpose of this type of experimental procedure is the ability to find the optimum conditions desired while minimizing experimental runs. In this case, the Taguchi design cut down the number of experiments from around 100 to 18. This matrix setup can be seen in ***Appendix A***. The variables in this experiment were the same as Phase I, solution heat-treatment time and temperature, and aging time and temperature. The quench delay, quench time, and quench temperature were held constant, as well as the incubation time, throughout the experiments. As can be seen in the methodology section of this report, two higher solution heat-treatment temperatures (545°, 550°) were examined as well as the typical 540°C SHT temperature. It has been reported [Pan, 2000] that the SSM Al 357 material does not experience any partial melting at temperatures up to 560°C, which is slightly higher than the conventionally (permanent mold, sand cast, etc.) cast Al 357 material. For this reason the group believed it would be beneficial to examine these elevated temperatures. Given the experimental setup, it was decided to use a Taguchi design consisting of two L9 matrices.

A small box furnace was used to carry out the solution and aging heat treatments. This furnace was calibrated to within ± 2°C, which is acceptable for these experiments. The quench tank was also calibrated to within acceptable values. Once the apparatus was calibrated, the experimental heat-treatments were carried out. For each experiment, one SSM 357 sample along with a conventionally cast A356.2 and A357.2 sample were treated at the same time. This was done to ensure that the variables between samples were minimized for comparison purposes. The time it took for these samples to reach the appropriate temperature, ramp time, inside the furnace was also examined. The ramp time for these samples was approximately 10-15 minutes. After completing their respective heat-treatments, a mechanical and microstructural analysis (Phase III) was performed.

Mechanical and Microstructural Evaluation (Phase III)

This phase of the project is critical and the most important in finding out why these castings behave the way in which they do. The mechanical testing was performed first followed by the microstructural characterization.

The strength of the samples was tested using an Instron tensile testing machine. From these tests we were able to find out the ultimate tensile strength of the material along with the percent elongation ***[Appendix B]***. These are two of the most important factors the commercial sector considers when choosing a material for automotive and aerospace applications. The hardness of the material can also be calculated when given the results of these tensile tests. For the purpose of this

study, the tensile strength and elongation after treatment were the focal point of the mechanical testing. Once the data from the tensile tests are obtained, it will be possible, using Taguchi analysis techniques, to determine the optimum heat treatment condition and the properties that the optimum condition should demonstrate. Although this Taguchi analysis is a fairly quick and accurate way of determining the optimum conditions, it can only give an optimum condition within the boundaries selected. For example, if the optimum heat treatment condition for material ductility was a solution heat-treatment of 24 hours at 530°C, we would not find this information from our Taguchi analysis. This is because we designed our matrix to examine only solution heat-treatment times between 1 -10 hours and temperatures between 540° - 550°C. By performing an analysis of variance (ANOVA) we are able to find the precent contribution of the different parameters selected, for example solution heat treatment time, temperature, aging time, and aging temperature. This ANOVA analysis has been performed with respect to both the tensile strength ***[Appendix D]*** and the % elongation ***[Appendix E].***

To compensate for this lack of ability to determine the absolute optimum heat-treatment conditions, the team decided to perform an ANN analysis as well. With the ANN, advanced neural network, analysis we are able to determine the optimum conditions even if they are not within the parameters tested.

After the samples were tensile tested, it was necessary to carry out a microstructural evaluation in order to find out what factors directly influenced the properties demonstrated. The fracture surfaces of the resulting tensile tested samples were examined using a scanning electron microscope (SEM). This SEM analysis gives insight as to the mode of failure of the sample while the optical microscope will show the resulting microstructure after heat-treatment. Selected samples, which have undergone different heat-treatments, will be examined and compared in hopes of relating the difference in microstructure to certain changes in their heat-treatment processes.

APPENDIX A: Taguchi Matrix for Heat Treatment of SSM 357 Alloy

Exp.	SHT (°C)	SHt (hours)	AHT (°C)	Aht (hours)
1	540	1	155	2
2	540	2	165	4
3	540	4	175	6
4	545	1	155	6
5	545	2	165	2
6	545	4	175	4
7	550	1	155	4
8	550	2	165	6
9	550	4	175	2
10	540	6	155	8
11	540	8	165	12
12	540	10	175	16
13	545	6	155	16
14	545	8	165	8
15	545	10	175	12
16	550	6	155	12
17	550	8	165	16
18	550	10	175	8

APPENDIX B: Tensile Results for Heat-Treated Samples

Sample ID	A357.2		A356.2	SSM 357
A1A2	UTS(ksi)	33.7	30.5	21.1
	% elong	1.60	2.39	1
A2B4	UTS(ksi)	44.9	36.9	44.0
	% elong	3.73	1.90	10.73
A4C6	40		43.4	42.6
	0.64		4.43	1.99
A6A8	47		38.7	41.4
	6.5		3.40	14.45
A8B12	43.3		39.5	46.5
	0.87		1.55	8.10
A10C16				
B1B6	44		38.3	46.1
	1.79		1.62	9.78
B4A4	41.4		39.2	39.9
	2.62		9.54	8.46
B6B16	49.7		41.4	43.5
	2.23		1.20	2.15
B8C8	42.2		48.0	
	0.70		4.0	
B10A12	38.9*		41.4	27.5*
	0.84*		2.67	0.78*
C1C4	47.5		44.5	45.3
	3.74		2.85	6.26
C2A6	34.8		40	40.8
	1.10		5.85	12.63
C4B2	36.9		37.3	37.8
	1.78		6.99	8.76
C6C12	52.2		47	46.3
	3.43		4.14	12.37
C8A16	42.5		44.6	45.6
	1.41		5.63	11.46
C10B8	49.9		38.9	41.2
	6.84		1.64	8.41

* Results are doubtful.

The Sample ID # is decoded as follows:

First letter denotes SHT temperature:	A = 540°C, B = 545°C, C = 550°C
First number denotes SHT time:	1 - 10 hours
Second letter denotes Aging temperature:	A = 155°C, B = 165°C, C = 175°C
Second number denotes Aging time:	2 - 16 hours

APPENDIX C: Quality Index of Heat Treated SSM Al 357 Samples

Quality Index: Q(MPa) = UTS (MPa) + 150 log (% elong.)

Condition	UTS (MPa)	% elongation	Quality Index
As Cast	233.05	17.35	418.94
A1A2	145.48	1	145.48
A2B4	303.38	10.73	457.97
A4C6	293.73	1.99	338.56
A6A8	285.45	14.45	459.43
A8B12	320.62	8.10	456.89
A10C16	*	*	*
B1B6	317.86	9.78	466.41
B2C2	284.76	16.43	467.11
B4A4	275.11	8.46	414.22
B6B16	299.93	2.15	349.79
B8C8	322	8.53	461.62
B10A12	*	*	*
C1C4	312.34	6.26	431.83
C2A6	281.32	12.63	446.53
C4B2	260.63	8.76	402.01
C6C12	319.24	12.37	483.09
C8A16	314.41	11.46	473.29
C10B8	284.07	8.41	422.79

1ksi = 6.895 MPa

APPENDIX D: Analysis of Variance with Respect to Tensile Strength

Trial Run	SHT	SHt	AHT	Aht	UTS	% Elongation	Quality Index
1	540	1	155	2	145.8	1	145.48
2	540	2	165	4	303.38	10.73	457.97
3	540	4	175	6	293.73	1.99	338.56
4	545	1	165	6	317.86	9.78	466.41
5	545	2	175	2	284.76	16.43	467.11
6	545	4	155	4	275.11	8.46	414.22
7	550	1	175	4	312.34	6.26	431.83
8	550	2	155	6	281.32	12.63	446.53
9	550	4	165	2	260.63	8.76	402.01

	Degrees of Freedor	Sum of Squares	Variance	% Contributio
SHT	2	3459.04	1729.52	16.15
SHt	2	1465.89	732.95	6.84
AHT	2	7546.75	3773.38	35.23
AHt	2	8950.16	4475.08	41.78

APPENDIX E: Analysis of Variance With Respect to % Elongation

Trial Run	SHT	SHt	AHT	Aht	UTS	Elongatio	Quality Index
1	540	1	155	2	145.8	1	145.48
2	540	2	165	4	303.38	10.73	457.97
3	540	4	175	6	293.73	1.99	338.56
4	545	1	165	6	317.86	9.78	466.41
5	545	2	175	2	284.76	16.43	467.11
6	545	4	155	4	275.11	8.46	414.22
7	550	1	175	4	312.34	6.26	431.83
8	550	2	155	6	281.32	12.63	446.53
9	550	4	165	2	260.63	8.76	402.01

Factors	Degrees of Freedom	Sum of Squares	Variance	Percent Contribution
SHT	2	75.80	37.902	39.84
SHT	2	105.09	52.545	55.24
AHT	2	8.81	4.407	4.63
AHT	2	0.54	0.270	0.28

APPENDIX F: Trained ANN Results for Tested Samples

	UTS(MPa)	UTS(MPa) (trained)	Elongation(%)	Elongation(%) (trained)
A1A2	145.48	150.586411	1	1
A2B4	303.38	306.172699	10.73	10.685494
A4C6	293.73	293.239288	1.99	2.009587
A6A8	285.45	287.137512	14.45	14.436964
A8B12	320.62	319.437225	8.1	8.105284
B1B6	317.86	318.841309	9.78	9.766171
B2C2	284.76	284.744293	16.43	16.399982
B4A4	275.11	271.598541	8.46	8.509809
B6B16	299.93	299.203827	2.15	2.184688
B8C8	322	317.516174	8.53	8.588956
C1C4	312.34	315.293732	6.26	6.230551
C2A6	281.32	280.762085	12.63	12.62949
C4B2	260.63	258.717133	8.76	8.775007
C6C12	319.24	319.10907	12.37	12.379145
C8A16	314.41	315.104065	11.46	11.448699
C10B8	284.07	287.445038	8.41	8.360417
	error:	0.1829057		

Advanced Casting Research Center (ACRC) Consortium Meeting

December 4-5, 2001

Report 01-#2

Metal Processing Institute
WPI, Worcester, MA 01609 USA
www.wpi.edu/+mpi

TABLE OF CONTENTS

A. Modeling of Rheology in Semi-Solid Alloys

MODELING OF RHEOLOGY IN SEMISOLID ALLOYS

Report No. PR–01#2

Research Team:	Philippe LeMenn		
	Andreas Alexandrou	+357-2-892256	andalexa@ucy.ac.cy
Focus Group:	Craig Bergsma		Northwest Aluminum
	Tom Caldwell		Madison-Kipp Corp.
	Ray Donahue		Mercury Marine
	Eric Erike		TRW
	John Jorstad		JLJ Technologies
	Steve Midson		Formcast
	Mike Thieman		THT Presses
	Per Arne Tondel		Elkem Aluminum
	Steve Udvardy		NADCA
	Jim Van Wert		Amcast
	Josef Woehrer		Salzburger Aluminum

PROJECT STATEMENT

Objectives

(a) Develop a general mathematical and computational model that can describe the flow of semisolid materials.

(b) Study various flows through modeling and simulation in order to validate the models and to study the flow behavior at the level allowed by the mathematical models. Obtain insight into the bulk flow of semisolid materials and help identify the influence of various flow parameters on the final product.

Strategy

Developed a general phenomenological mathematical model that describes the flow of viscoplastic materials with shear and time dependent properties and used actual experimental data to fit the model parameters.

ACHIEVEMENTS TO DATE

The following tasks were completed:

- Development of mathematical and computational models
- Study of basic flow geometries and development of processing maps
- Document the stability for semisolid material flow into a simple cavity

CHANGES IN PROJECT STATEMENT

None

WORK PLANNED FOR THE NEXT QUARTER

Determine the material constants through "reversed engineering". This includes modeling of the compression experiments performed by Pan and Apelian to establish the constants in the constitutive relations

PROJECT SCHEDULE

Task	November	December	January	February	March	April
Mathematical Model	xxxxxxxxx	xxxxx				
Computational code	xxxx	xxxxxxxxx	xxxxxxxx			
Numerical Simulations			xxxxxx	xxxxxxxx	xxxxxxxx	xxxxxxxx
Report				xxxxxxxx	xxxxxxxx	xxxxxxxx

APPENDIX

A.N. Alexandrou, P. LeMenn, D. Apelian, "On the Reliability of the Semisolid Process," Metallurgical Transactions (to be submitted).

Appendix A

Flow Instabilities in Herschel-Bulkley Fluids

Andreas N. *Alexandrou*[a,1], Philippe Le *Menn*[a],
Vladimir Entov[b] and George C. Georgiou[c]

[a] *Semisolid Metal Processing Lab, MPI, Worcester Polytechnic Institute*
Worcester, MA 01609, USA

[b] *Institute for Problems in Mechanics of the Russian Academy of Science*
pr. Vernadskogo, 101, 117526 Moscow, Russia

[c] *Department of Mathematics, University of Cyprus*
CY 1618, Nicosia, Cyprus

Abstract

In this paper we investigate the interaction of a two-dimensional jet of a Herchel-Bulkley fluid with a vertical surface at a distance L from the die exit. This problem also simulates the early stages of filling of a two-dimensional cavity. The main purpose of this work is to study numerically flow instabilities for this flow arrangement. Results are obtained for a range of Reynolds and Bingham numbers, and we establish the effects of these dimensionless numbers on both the filling, and the stability of the jet.

1 Introduction

Materials that exhibit no deformation below a finite applied shear stress (τ_o) are known as Bingham plastics [1]. Examples of such materials include paint, slurries, aqueous foams, pharmaceutical products, pastes, polymeric solutions, paper pulp, food substances like margarine, mayonnaise and ketchup [2], colloidal suspensions [3], plastic propellant doughs [4], drilling fluids [5], and semisolid materials [6].

The motivation of the present work is our interest in the processing of semisolid slurries. These are two-phase slurries whose behavior can be represented using a Herschel-Bulkley fluid model. In processing of such slurries filling patterns are often irregular and unpredictable, pointing to the existence of possible instabilities. Here, we investigate the "toothpaste" behavior which is a typical flow instability observed in semisolid slurry processing. Figure 1 shows an experimental observation of such an instability: as shown, even though the part is symmetric, the left arm develops a wave-like pattern after the jet hits the closed-end of the cavity. A similar jet profile is also shown in Fig. 2. The name "toothpaste" comes from the similarity between this instability and the toothpaste behavior when forced out of its tube. From a practical point of view such instabilities are undesirable and can lead to non-uniformities in the parts being made. Investigations by Midson et al. [7, 8] provide further evidence of these instabilities, and demonstrate experimentally that slow filling yields the "best" die filling behavior, with mostly laminar flow, and the least amount of material folding. In general, these instabilities originate at the point where the filling front in the form of a jet meets the wall of the cavity. Therefore, the jet-vertical wall arrangement chosen here represents well the early stages of filling of a 2-D cavity. To our knowledge no similar investigation has been reported in the literature.

Several rheological equations and yield criteria have been proposed [9, 10, 11] to describe the stress-deformation behavior of materials exhibiting a yield stress. The most commonly used model is the Bingham model [1, 12, 13], which in tensorial form is expressed as:

$$\underline{\underline{\dot{\gamma}}} = 0 \quad \text{for} \quad \tau \leq \tau_o, \tag{1}$$

$$\underline{\underline{\tau}} = \left(\eta + \frac{\tau_o}{\dot{\gamma}}\right) \underline{\underline{\dot{\gamma}}} \quad \text{for} \quad \tau > \tau_o, \tag{2}$$

where $\underline{\underline{\dot{\gamma}}} = \left(\nabla \mathbf{u} + \nabla \mathbf{u}^{\mathbf{T}}\right)$ represents the rate of strain tensor, $\underline{\underline{\tau}}$ the extra stress tensor, τ_o the yield stress and η the viscosity of the deformed material. τ and $\dot{\gamma}$ are respectively the second invariants of the extra stress and rate of strain tensors, defined as:

$$\tau = \left[\frac{1}{2}\tau_{ij}\tau_{jk}\right]^{1/2} \quad \text{and} \quad \dot{\gamma} = \left[\frac{1}{2}\dot{\gamma}_{ij}\dot{\gamma}_{jk}\right]^{1/2}. \tag{3}$$

The rheological behavior of a Bingham fluid is characterized by two different flow regimes: if $\tau \leq \tau_o$ the material behaves as a rigid solid. If $\tau \geq \tau_o$ it flows with the apparent viscosity $\eta_{app} = \eta + \frac{\tau_o}{\dot{\gamma}}$.

The Herschel-Bulkley model is a generalization of the Bingham model that takes into account changes in the effective viscosity with the applied shear rate. The Herschel-Bulkley model assumes that the effective viscosity upon deformation follows a power-law behavior:

$$\eta = \kappa \dot{\gamma}^{n-1}, \tag{4}$$

where n and κ are the power-law and consistency indices, respectively. The fluid behavior is shear-thickening for $n > 1$, and shear-thinning for $n < 1$. For $n = 1$, the Herschel-Bulkley model reduces to the Bingham model with the consistency index equivalent to the viscosity.

The two distinct regions (yielded ($\tau > \tau_o$) and unyielded ($\tau < \tau_o$)) of the fluid are separated by the "yield surface" defined as the surface where the local stress is equal to the yield stress. In numerical modeling, in addition to the non-linearities in the governing equations, an inherent difficulty is the discontinuity in the constitutive relation. Due to the presence of $\dot{\gamma}$ in the denominator of Eq. (2), the apparent viscosity becomes unbounded at vanishing shear rates. Also, while calculating the velocity field the shape and location of the yield surface are unknown. Although this does not constitute any limitation in analytic solutions in simple cases such as flow in tubes [14], it introduces significant difficulties in more complicated problems that are only amenable to numerical analysis. To overcome these issues, several modified versions of Eqs. (1) and (2) have been proposed [15, 16, 17, 18]. Keunings [19] reviews current developments in the field of computational rheology applied to the prediction of the flow of polymeric liquids, i.e., highly non-Newtonian materials, in complex geometries. Many of the reviewed papers are representative of current trends in the field of numerical modeling of Herschel-Bulkley fluids.

For numerical modeling purposes, a common approach is to approximate the rheological behavior of the fluid to be valid uniformly at all levels of stress. Papanastasiou [15] introduced a regularization parameter m that controls the

exponential rise in the stress at low rates of strain:

$$\underline{\underline{\tau}} = \left[\eta + \tau_o \frac{1 - exp(-m\dot{\gamma})}{\dot{\gamma}}\right] \underline{\underline{\dot{\gamma}}}. \tag{5}$$

The parameter m has dimensions of time. This constitutive relation is expressed in terms of three independent material parameters, τ_o, κ, and n, which are determined from experimental data. The Herschel-Bulkley behavior is approximated for relatively large m values. According to Eq. (5) for $\dot{\gamma} \approx 0$ the apparent viscosity is finite, given by $\eta_{app} \approx (\eta + m\tau_o)$. The constitutive relation is then expressed as $\underline{\underline{\tau}} \approx (\eta + m\tau_o)\underline{\underline{\dot{\gamma}}}$. Papanastasiou [15] validated this model on several simple flows such as one-dimensional channel flow, two-dimensional boundary layer flow and extrusion flow. The accuracy and effectiveness of this model in representing Herschel-Bulkley fluids has also been demonstrated by Elwood et al. [20], Mitsoulis and Abdali [21], Tsamopoulos et al. [22], Blackery and Mitsoulis [23] and Burgos et al. [18, 24].

Experimental data reported by Ellwood et al. [20], Keentok et al. [25] and Dzuy et al. [26] actually demonstrate that a continuous model provides a better approximation to experimental data than the ideal model. Therefore, it is postulated that the ideal Bingham model may be only a theoretical idealization. Recent investigations by Blackery and Mitsoulis [23], Beaulne and Mitsoulis [27], Papanastasiou and Boudouvis [28] concentrate on problems that involve Bingham and Herschel-Bulkley fluids. In these studies the material was also modeled using Papanastasiou's regularized constitutive equation.

In a recent study, Alexandrou et al. [29] investigated filling of a 2-D cavity by Bingham fluids. They examined the relative importance of inertial, viscous and yield stress effects on the filling profiles. They identified five characteristic filling patterns: "mound," "disk," "shell," "bubble" and a "transition" between that of "mound" and "bubble" patterns. A summary of these different flow behaviors is shown in Fig. 3. These characteristic flow patterns highlight the important role of the finite yield stress in Bingham fluids. Experimental studies confirmed the existence of the numerically obtained patterns; the "mound," "disk," and "shell" patterns have been observed by Paradies and Rappaz [30] in semisolid processing. Recent experimental results by Koke et al. [31] also confirmed these patterns by using

model substances such as chocolate cream, calcium-carbonate/oil suspension, tomato paste, ultrasonic gel and Newtonian silicone oil.

The main objective of the present work is to investigate the stability of a jet of a Herschel-Bulkley fluid emanating from a die and impinging on a vertical wall. As discussed earlier, this flow arrangement simulates also the early stages of filling of a 2-D cavity. Since the results obtained by Alexandrou et al. constitute the equilibrium states for the problem considered here, for the purpose of the present study we also simulated the cases considered in [29].

2 Mathematical and Computational Model

2.1 Governing Equations

The schematic of the problem considered here is shown in Fig. 4. The 2-D geometry is characterized by the inlet section (length l and height H). The material is injected in the die from the left side and hits the vertical solid surface at a distance L away. The flow was modeled using the conservation of mass and momentum for an incompressible fluid:

$$\nabla \cdot \mathbf{u} = 0, \tag{6}$$

$$\rho \left[\frac{\partial \mathbf{u}}{\partial t} + \mathbf{u} \cdot \nabla \mathbf{u} \right] = \nabla \cdot \underline{\underline{\sigma}}, \tag{7}$$

where $\mathbf{u}$ is the velocity vector, ρ the density of the fluid, and $\underline{\underline{\sigma}}$ the total stress tensor, which is given by

$$\underline{\underline{\sigma}} = -P\underline{\underline{I}} + \underline{\underline{\tau}}.$$

Here P represents the total pressure, $\underline{\underline{I}}$ the unit tensor, and $\underline{\underline{\tau}}$ the viscous stress tensor. The body force per unit volume due to gravity was neglected in this study.

2.2 Non-Dimensionalization

The set of governing equations (Eqs. (6) and (7)) were non-dimensionalized using:

$$x_i^* = \frac{x_i}{H};\ t^* = \frac{t}{H/U_o};\ \mathbf{u}^* = \frac{\mathbf{u}}{U_o};\ P^* = \frac{P}{\tau_o};\ \underline{\underline{\tau}}^* = \frac{1}{\tau_o}\underline{\underline{\tau}};\ \underline{\underline{\sigma}}^* = \frac{1}{\tau_o}\underline{\underline{\sigma}}, \tag{8}$$

where H is taken as the inlet height and U_o the average inlet velocity. Due to the non-dimensionalization the imposed volumetric flow rate is $Q^* = 1$.

2.3 Dimensionless Equations

Using the dimensionless groups introduced in Eq. (8) we can rewrite the governing equations in a dimensionless form:

$$\nabla \cdot \mathbf{u}^* = 0, \tag{9}$$

$$Re\left[\frac{\partial \mathbf{u}^*}{\partial t^*} + \mathbf{u}^* \cdot \nabla \mathbf{u}^*\right] = Bi \nabla \cdot \underline{\underline{\sigma}}^*. \tag{10}$$

Here,

$$\underline{\underline{\sigma}}^* = -P^* \underline{\underline{I}} + \underline{\underline{\tau}}^*,$$

is the total non-dimensional stress tensor. According to Eqs. (9) and (10) the fluid behavior depends on two dimensionless parameters, the Reynolds (Re) and Bingham (Bi) numbers, defined respectively as:

$$Re = \frac{\rho U_o H}{\eta_{eff}} \quad \text{and} \quad Bi = \frac{\tau_o H}{\eta_{eff} U_o}. \tag{11}$$

The effective viscosity η_{eff} is obtained from the one-dimensional analog of the constitutive equation (Eq. (5)):

$$\tau = \tau_o + \kappa \dot{\gamma}^n = \tau_o + \kappa \mid \dot{\gamma} \mid^{n-1} \dot{\gamma}, \tag{12}$$

where $\dot{\gamma}$ is the shear rate, and $\eta_{eff} = \kappa \mid \dot{\gamma} \mid^{n-1}$ is the effective viscosity.

Therefore, the Reynolds and Bingham numbers are generalized as:

$$Re = \frac{\rho U_o^{(2-n)} H^n}{\kappa} \quad \text{and} \quad Bi = \frac{\tau_o H^n}{\kappa U_o^n}. \tag{13}$$

The Herschel-Bulkley constitutive relation, Eq. (5), can thus be rewritten in a dimensionless form:

$$\underline{\underline{\tau}}^* = \left[\frac{1}{Bi}\dot{\gamma}^{*(n-1)} + \frac{[1 - exp(-m^*\dot{\gamma}^*)]}{\dot{\gamma}^*}\right]\underline{\underline{\dot{\gamma}}}^*, \tag{14}$$

where $\underline{\underline{\dot{\gamma}}}^*$ is the dimensionless rate of strain tensor, $\dot{\gamma}^*$ its second invariant, and m^* the dimensionless growth exponent, which are respectively defined as

$$\underline{\underline{\dot{\gamma}}}^* = \frac{1}{U_o/H}\underline{\underline{\dot{\gamma}}}; \quad \dot{\gamma}^* = \frac{\dot{\gamma}}{(U_o/H)^2}; \quad m^* = \frac{mU_o}{H}. \tag{15}$$

Equation (14) has only two independent material parameters (Bi and n), whereas Eq. (5) had three (κ, τ_o, and n). Hereafter, for convenience, the asterisk ($*$) is dropped from the non-dimensional variables and all physical quantities mentioned are implicitly dimensionless.

The flow is established by applying a fixed dimensionless volumetric flow rate (i.e., Q=1) at the inlet with a parabolic velocity profile imposed at the entrance plane of the inlet. The inlet length is fixed at a sufficient distance l so that the flow becomes fully developed prior to reaching the exit of the die. In this study the non-dimensional length of the inlet was fixed at $l = 5$ which was found to be sufficient to ensure fully developed flow in the die. Along the die walls the velocity was set to zero. The same no-slip condition was imposed at the end-wall.

As mentioned earlier, different lengths L were used in order to study the influence of this geometrical parameter on the stability of the jet. The simulation is initialized when the jet emanating from the inlet section reaches the end-wall. The initial jet profile is taken from the steady state results, and corresponds to a column of fluid hitting the end-wall at velocities $u \approx 1$, $v \approx 0$.

3 Method of Solution

The governing equations and constitutive relation were discretized using the classical mixed-Galerkin finite element method with nine-node rectangular elements. The resulting non-linear system of equations was linearized using a Newton-Raphson iteration procedure. For converged results in the

Newton-Raphson iterative scheme, usually three to four iterations were necessary at each time step.

A detailed presentation of the mixed-Galerkin finite element discretization for the extrusion problem can be found in [20, 32, 33]. The nonlinear system of equations resulting from this analysis is then solved by Newton-Raphson iteration. The spatial discretization reduces the set of equations to a system of ordinary differential equations:

$$\mathbf{M} \cdot \frac{\partial \mathbf{q}}{\partial t} + \mathbf{R}(\mathbf{q}) = 0, \tag{16}$$

where $\mathbf{q} = [u_1(y,z,t), v_1(y,z,t), ..., h_{N_h}(z,t)]$ is the vector of all the time-dependent nodal unknowns, $\mathbf{R}$ is the column vector of the time-dependent Galerkin residuals. The time derivatives are discretized by a standard backward difference scheme,

$$\mathbf{M} \cdot \frac{\partial \mathbf{q}}{\partial t} \equiv \mathbf{M} \cdot \left[\frac{\mathbf{q}^{n+1} - \mathbf{q}^n}{\Delta t} \right] = \mathbf{R}(\mathbf{q}^{n+1}). \tag{17}$$

Thus all the nodal unknowns of the velocity components and pressure are evaluated simultaneously. The free surface is calculated automatically by properly assigning the velocity of the nodes along the free surface to reflect the fact that the free surface is a material surface.

Equation (17) is then solved at each time step by Newton-Raphson iteration for $\mathbf{u}$, P, and h. The set of linear equations is repeatedly solved by a frontal technique [34, 35, 36] developed by Hood [37]. The tessellation is updated at every iteration with the newly found free surface. The initial conditions are those of a jet from its steady state. The initial velocity and pressure fields are determined from the steady-state counterpart of the problem at the initial configuration.

4 Results

In this work, we concentrate on a problem equivalent to that of die filling, i.e., the interaction of a Herschel-Bulkley fluid jet and a vertical surface at a distance L from the die exit and we study the interplay between inertia, viscous drag and yield stress, or as expressed in terms of force per

unit depth, $F_i \equiv \rho U_o^2 H$, $F_v \equiv \eta U_o$, and $F_{\tau_o} \equiv \tau_o H$ respectively (Fig. 5). Non-dimensional analysis shows that the flow depends on two dimensionless parameters: the Reynolds (Re) and Bingham (Bi) numbers. The Reynolds number represents the F_i/F_v ratio, while the Bingham number indicates the F_{τ_o}/F_v ratio. A third choice is the Saint-Venant number which indicates the importance of the yield stress effects relative to inertia forces (F_{τ_o}/F_I) and which is defined as:

$$Sv = \frac{Bi}{Re} = \frac{\tau_o}{\rho U_o^2}. \tag{18}$$

Obviously, only two of these three parameters are independent. The appropriate choice of parameters depends on the flow regime being analyzed. The effects of Re and Bi are investigated using the two-dimensional geometry shown in Fig. 4, with the finite-element mesh shown in Fig. 6.

The parameter m in the regularized model was set to a value of $m = 1000$, which was found to be high enough to insure results independent of m. The reported results are also mesh and time-step independent. A more pertinent study of the effect of m on the accuracy of the results can be found in [18, 24]. The power-law index n was set to a value of $n = 1$ as in [29].

Figure 7 shows the results for conditions similar to those in [29]. The five typical flow behaviors reported in [29] have been reproduced here as well, providing thus further evidence on the existence of these patterns. Table 1 summarizes the flow parameters for the flow patterns shown in the aforementioned figure.

Re	Bi	$FlowPattern$
500	10	Shell
6	0.1	Disk
0.5	0.1	Mound
1	3	Bubble
10	1.7	Transition

Table 1: Flow parameters used for the displayed jet behaviors ($L = 10$ geometry).

The figure also shows the topography of the yielded and unyielded regions. As shown in the figure, only the "bubble" and "transition" patterns

exhibit significant unyielded zones. Therefore the first three patterns behave in a manner consistent with a viscous fluid. The "bubble" and "transition" patterns, though, are expected to be influenced by the yield stress effects. As we will demonstrate below, flow instabilities are primarily connected to these two patterns.

The following results examine the interaction of the Herschel-Bulkley jet with a vertical wall as a function of rheological and geometrical parameters. Numerical simulations of flows that in real life are unstable may fail to predict flow instabilities. This is due to the almost perfect symmetry of numerical results, and due to the fact that numerical errors take a long time to grow to a magnitude that can trigger instabilities. Therefore, it is customary to introduce an artificial disturbance to disrupt the symmetry of the flow. This artificial instability is typically very small, and it is applied for a short duration. Here, a small disturbance is introduced in the flow by imposing an asymmetric velocity profile at the inlet for a short time Δt, beginning at the moment the jet reaches the vertical wall (defined as $t = 0$ in the following). For $t > \Delta t$, the inlet velocity was kept constant and symmetric. In both the symmetric and asymmetric cases the volumetric flow rate was kept constant. The flow field and the jet stability are found to be independent of the magnitude and the duration of the asymmetry.

The finite-element mesh used in the simulations is refined around zones that are sensitive to flow singularities and where gradients are large (die exit and end-wall). The case $n \neq 1$ is considered at the end of the present study. The unsteady simulation is initiated at the time where the jet hits the vertical wall ($t = 0$). The initial conditions were taken from the steady solution of the problem for the configuration when the jet is about to touch the wall. The geometry used here includes an inlet section ($H = 1$, $l = 5$), and a vertical wall at a distance L from the exit of the die. Results are also shown for variable values of L. Typical jet-wall interactions obtained numerically are shown in Figs. 8 and 9, as sequences of 'snapshots' of the jet profile, where t is the non-dimensional time.

Figure 8 shows the jet behavior for the $L = 10$ geometry at a low Reynolds number ($Re = 1$) and at a moderate Bingham number ($Bi = 3$). For a symmetric velocity profile at the inlet (i.e., no disturbance), these conditions lead to a "bubble" pattern. Here, when the jet emanating from the inlet section reaches the vertical wall, it grows as a "bubble" up to a dimensionless

time $t \approx 7$. When the disturbance is introduced from the start of the flow ($t = 0$) until $t = \Delta t = 1.5$, it triggers an instability which forces the jet to bend, very much like the buckling of a slender solid column. This flow behavior is very similar to what is observed experimentally and described as the "toothpaste" effect. For the discussion that follows such behavior is labeled as "unstable".

The flow shown in Fig. 9 is obtained for $Re = 5$ and $Bi = 1$. For both symmetric and asymmetric flow conditions the jet grows in a manner consistent with a "transition" pattern. Therefore, the initial disturbance has no impact on the stability of the jet, and no noticeable difference can be observed between the symmetric and asymmetric cases. In the discussion below this flow behavior is labeled as "stable".

Figure 10 shows a complete map of the jet profiles as a function of the Reynolds and Bingham numbers for the range $0.5 \leq Re \leq 50$, $0 < Bi \leq 40$. This map clearly shows the regions where "stable" and "unstable" patterns occur. The estimated boundary between these two zones has been sketched in in order to demarcate the range of Re and Bi which they correspond to. On this map, the symbols ▲, •, ■, ▼ represent respectively the "mound," "disk," "bubble" and "transition" patterns. The hollow symbols (□, and ▽) represent the cases discussed in detail (Figs. 8 and 9). As speculated, while "bubble" pattern leads to unstable jet behavior, "shell," "disk" and "mound" patterns remain stable and most of the "transition" cases lead to stable jet profiles. The "bubble" pattern is very sensitive to flow instabilities, that prevent this pattern to develop. These numerical results explain why experimental observations of the "bubble" pattern are not as common as the other patterns. It is clear from the results that the instabilities are indeed the result of the finite yield stress and the way yielded and unyielded regions interact with each other.

As mentioned earlier, it is possible to express the results in terms of the Saint-Venant number as shown in Fig. 11. In the map, the squares (■) represent stable configurations and the upward pointing triangles (▲) correspond to unstable behaviors. The hollow markers (□ and △) correspond to the cases shown in Figs. 8 and 9. The advantage of considering the Saint-Venant number is that it is independent of the characteristic length scale parameter H, and is expressed in terms of fluid properties and kinematics of the flow.

So far the length L was kept constant. However, the stability characteristics depend also on the length of the die L. The effect of the distance between the die exit and the vertical wall was established by using three different lengths $L = 10$, 15 and 20. Figure 12 highlights this effect on the stability of the jet for given rheological parameters ($Re = 1$, $Bi = 0.7$). The jet behavior is either stable and symmetric (Fig. 12(a), $L = 10$) or unstable and toothpaste-like (Fig. 12(b), $L = 15$, and (c), $L = 20$). This demonstrates that the longer the die, the more likely it is to observe the toothpaste instability. Figure 13 summarizes this behavior in a manner similar to Fig. 10 for $L = 15$ and $L = 20$. The map shows the estimated boundaries between stable and unstable jet behavior for the three lengths studied. The solid line represents the $L = 10$ case while the dashed line and the dashdotted line stand for the $L = 15$ and $L = 20$ cases, respectively. From that figure, the overall jet stability is confirmed: the longer L, the more likely it is to observe toothpaste-like instabilities.

The results shown are for Bingham fluids ($n = 1$). However, once the yield stress is exceeded, Herschel-Bulkley fluids flow either in a shear-thinning or shear-thickening manner. The effect of the power-law exponent was studied for two cases: one corresponding to a shear-thinning fluid ($n = 0.5$) and another to a shear-thickening fluid ($n = 1.5$). For both cases the length was set to $L = 15$. Figure 14 shows the overall stability behavior as a function of n. Again, limiting lines separate stable and unstable behaviors. The solid line represents the $n = 1$ case while the dashed line and the dashdotted line stand for the $n = 0.5$ and $n = 1.5$ cases, respectively. A shift between the three limiting lines can be observed: the smaller the power-law index, the more unstable the flow is. In other words, a shear-thinning behavior is more sensitive to instabilities than a shear-thickening one. It appears also that the power-law index becomes less important (actually it is not important at all) for large values of Bi. This is due to the fact that for large Bi the flow behaves more like a solid as very little of the fluid deforms.

5 Conclusions

The numerical simulations presented in this study verify the importance of the finite yield stress in Herschel-Bulkley flows. The results confirm the

existence of five characteristic flow patterns ("shell," "disk," "mound," "bubble" and "transition") that have been observed both experimentally and numerically. By controlling flow parameters, one may be able to a priori fix jet behavior to lead to desirable quality and properties of the final parts.

In actual Herschel-Bulkley flows, the injection process is very sensitive to flow instabilities which may lead to irregular and unpredictable filling patterns. This undesired behavior is likely to happen at distinct combinations of flow parameters. Stability maps of the injection process have been drawn as a function of these parameters. It was concluded that the most unstable pattern is that of "bubble" and to a lesser degree that of the "transition" pattern, primarily due to the effects of the yield stress.

Acknoledgments: Partial support for this study was provided by Aluminium Pechiney, France.

References

[1] Bingham E. C. *Fluidity and Plasticity.* McGraw-Hill, 1922.

[2] Vradis G. C., and Őtűgen M. V. The axisymmetric sudden expansion flow of a non-Newtonian viscoplastic fluid. *Journal of Fluids Engineering*, 119:193–200, 1997.

[3] Covey G. H. and Stanmore B. R. Use of parallel-plate plastometer for the characterization of viscous fluids with yield stress. *Journal of Non-Newtonian Fluid Mechanics*, 8:249, 1981.

[4] Carter R. E. and Warren R. C. Extrusion stresses, die swell, and viscous heating effects in double-phase propellants. *Journal of Rheology*, 31:151–173, 1987.

[5] Azouz I., Shirazi S. A., Pilehvari A., and Azar J. J. Numerical simulation of laminar flows of yield-power-law fluids in conduits of arbitrary cross-section. *Journal of Fluids Engineering*, 115:710–716, 1993.

[6] Ahmed A. and Alexandrou A. N. Processing of semisolid materials using a shear-thickening Bingham fluid model. In *Proceeding of the*

1994, ASME Fluids Engineering Division Summer Meeting, FED-Vol. 179, pages 83–87, New York, 1994.

[7] Midson S. P., Minkler R. B., and Brucher H. B. Gating of semisolid aluminum castings. In *6th International Conference on Semisolid Processing of Alloys and Composites, Conference Proceedings*, pages 67–71, Turin, Italy, 27-29 September 2000.

[8] Midson S. P., Thornhill L. E., and Young K. P. Influence of key process parameters on the quality of semisolid metal cast aluminum components. In *5th International Conference on Semisolid Processing of Alloys and Composites, Conference Proceedings*, pages 181–188, Golden, CO, 23-25 June 1998.

[9] Fredrickson A. G. *Principles and applications of rheology.* Prentice Hall, Englewood Cliffs, NJ, 1964.

[10] Argon A. S. *Constitutive equations in plasticity.* MIT Press, Cambridge, MA, 1975.

[11] Malvern L. E. *An introduction to the mechanics of the continuous medium.* Prentice Hall, Englewood, NJ, 1969.

[12] Oldroyd J. G. A rational formulation of the equations of plastic flow for a Bingham solid. *Proceedings of the Cambridge Philosophical Society*, 43:100–105, 1947.

[13] Bird R. B., Dai G. C., and Yarusso B. J. The rheology and flow of viscoplastic materials. *Rev. Chemical Engineering*, 1:1–70, 1983.

[14] Bird R. B. and Armstrong R. C. *Dynamics of polymeric liquids.* John Wiley and Sons, New-York, NY, 1977.

[15] Papanastasiou T. C. Flows of materials with yield. *Journal of Rheology*, 31:385–404, 1987.

[16] Bercovier M. and Engelman M. A finite element method for incompressible non-Newtonian flows. *Journal of Computational Physics*, 36:313–326, 1980.

[17] O'Donovan E. J. and Tanner, R. I. Numerical study of the Bingham squeeze film problem. *Journal of Non-Newtonian Fluid Mechanics*, 15:75–83, 1984.

[18] Burgos G. R., Alexandrou A. N., and Entov V. On the determination of yield surfaces in Herschel-Bulkley fluids. *Journal of Rheology*, 43:463–483, 1999.

[19] Keunings B. Advances in the computer modeling of the flow of polymeric liquids. *accepted for publication in Computational Fluid Dynamics Journal*, ??:??, 1999.

[20] Ellwood K. R. J., Georgiou G. C., Papanastasiou T. C., and Wilkes J. O. Laminar jets of Bingham-plastic liquids. *Journal of Rheology*, 34:787–811, 1990.

[21] Mitsoulis E., Abdali S. S., and Markatos N. C. Flow simulation of Herschel-Bulkley fluids through extrusion dies. *The Canadian Journal of Chemical Engineering*, 71:147–160, 1993.

[22] Tsamopoulos J. A., Chen M. F., and Borkar A. V. On the spin coating of viscoplastic fluids. *Rheologica Acta*, 35:597–615, 1996.

[23] Blackery J. and Mitsoulis E. Creeping motion of a sphere in tubes filled with a Bingham plastic material. *Journal of Non-Newtonian Fluid Mechanics*, 70:59–77, 1997.

[24] Burgos G. R. and Alexandrou A. N. Flow development of Herschel-Bulkley fluids in a sudden 3-D square expansion. *Journal of Rheology*, 43:485–498, 1999.

[25] Keentok M., Milthorpe J. F., and O'Donovan E. On the shearing zone around rotating vanes in plastic liquids: theory and experiment. *Journal of Non-Newtonian Fluid Mechanics*, 17:23, 1985.

[26] Dzuy N. Q. and Boger D. V. Direct yield stress measurement with the vane method. *Journal of Rheology*, 29:334, 1985.

[27] Beaulne M. and Mitsoulis E. Creeping motion of a sphere in tubes filled with Herschel-Bulkley fluids. *Journal of Non-Newtonian Fluid Mechanics*, 72:55–71, 1997.

[28] Papanastasiou T. C. and Boudouvis A. G. Flows of viscoplastic materials: models and computations. *Computers and Structures*, 64:677–694, 1997.

[29] Alexandrou A. N., Duc E., and Entov V. Inertial, viscous and yield stress effects in Bingham fluid filling of a 2-D cavity. *Journal of Non-Newtonian Fluid Mechanics*, 96:383–403, 2001.

[30] Paradies C. J. and Rappaz M. Modeling the rheology of semisolid metal alloys during die casting. In *Modeling of Casting, Welding and Advanced Solidification Processes VIII. Proceedings of the 8th International Conference on Modeling of Casting and Welding Processes*, pages 933–940, San Diego, CA, June 7-12 1998. The Minerals, Metals and Materials Society, Edited by Thomas B. G. and Beckermann C.

[31] Koke J., Modigell M., Hufschmidt M., and Alexandrou A. A study on the die filling behavior with semisolid fluids. In *6th International Conference on Semisolid Processing of Alloys and Composites, Conference Proceedings*, pages 635–639, Turin, Italy, 27-29 September 2000.

[32] Georgiou G. C. *Singular finite elements for newtonian flow problems with stress singularities.* PhD thesis, The University of Michigan, Ann Arbor, MI, 1989.

[33] Housiadas K., Georgiou G. and Tsamopoulos J. The steady annular extrusion of a Newtonian liquid under gravity and surface tension. *International Journal for Numerical Methods in Fluids*, 33:1099–1119, 2000.

[34] Irons B. M. A frontal solution program for finite element analysis. *International Journal for Numerical Methods in Engineering*, 2:5, 1970.

[35] Walters R. A. The frontal method in hydrodynamics simulations. *Computers and Fluids*, 8:265, 1980.

[36] Boudouvis A. G. and Scriven L. E. Explicitly vectorized frontal routine for hydrodynamic stability and bifurcation analysis by Galerkin/finite element methods. In *Proc. Supercomp. Appl. Symp.*, Oct. 31-Nov. 1, 1984.

[37] Hood P. Frontal solution program for unsymmetric matrices. *International Journal for Numerical Methods in Engineering*, 10:379, 1976.

Figure 1: Flow instability in SSMP: toothpaste behavior (Courtesy of Aluminium Pechiney).

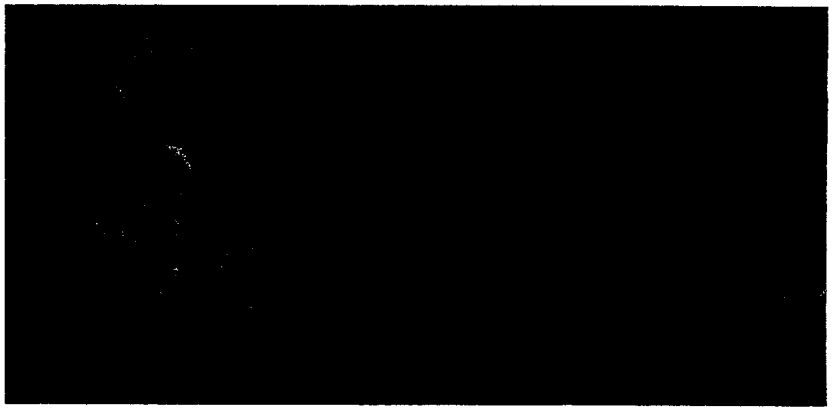

Figure 2: Flow instability in SSMP: toothpaste behavior (Courtesy of Aluminium Pechiney).

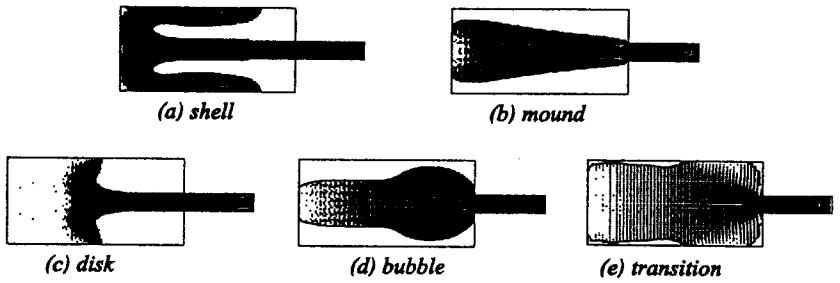

Figure 3: Summary of the flow patterns observed in 2-D die filling [29].

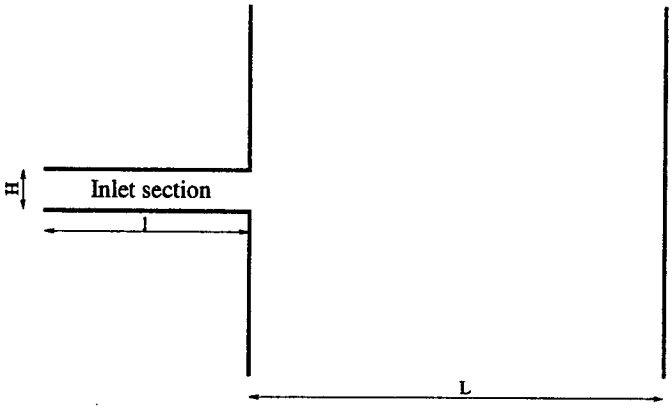

Figure 4: Geometry of the two-dimensional cavity (H, l, L).

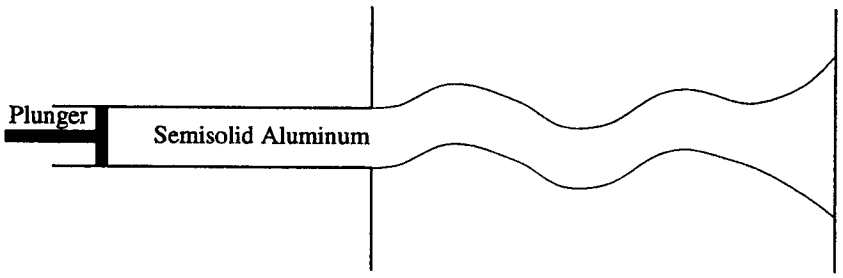

Figure 5: Schematic of the "toothpaste" behavior in a simple cavity.

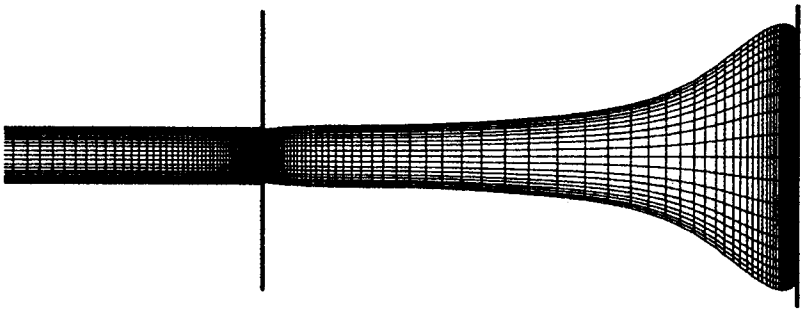

Figure 6: Geometry and finite element mesh.

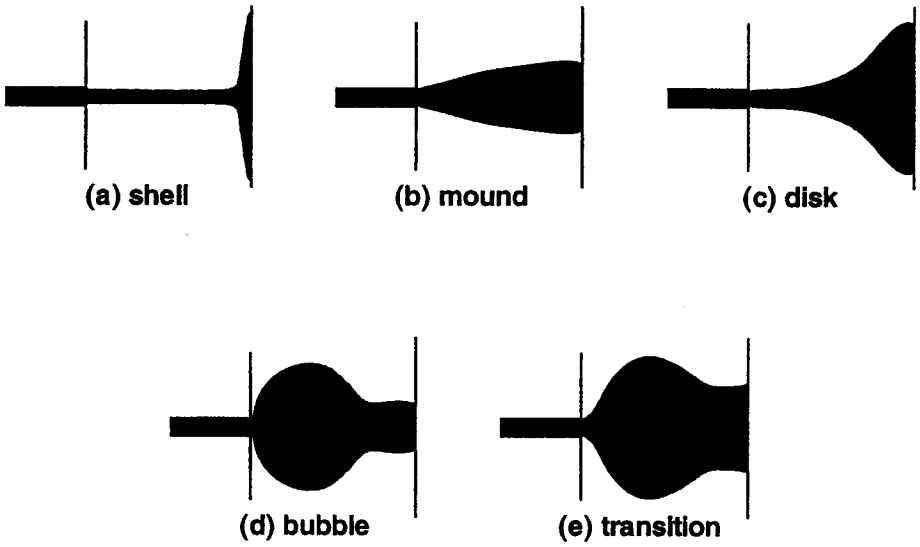

Figure 7: Summary of the flow patterns observed for the $L = 10$ geometry. Yielded and unyielded regions are highlighted.

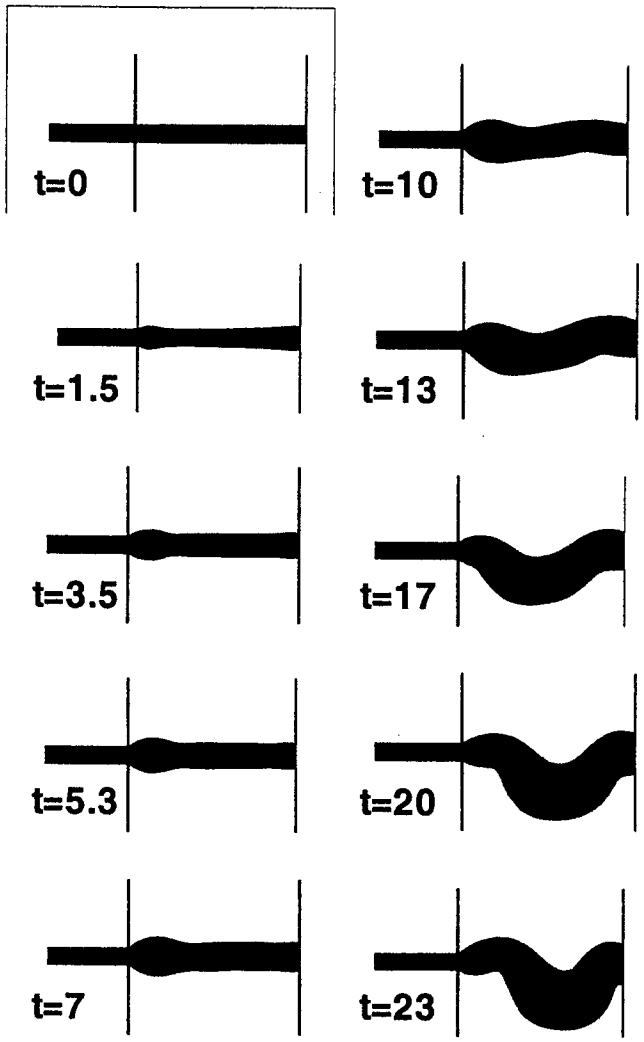

Figure 8: Toothpaste behavior, $Re = 1$, $Bi = 3$, $L = 10$. The disturbance is imposed from $t = 0$ until $t = 1.5$.

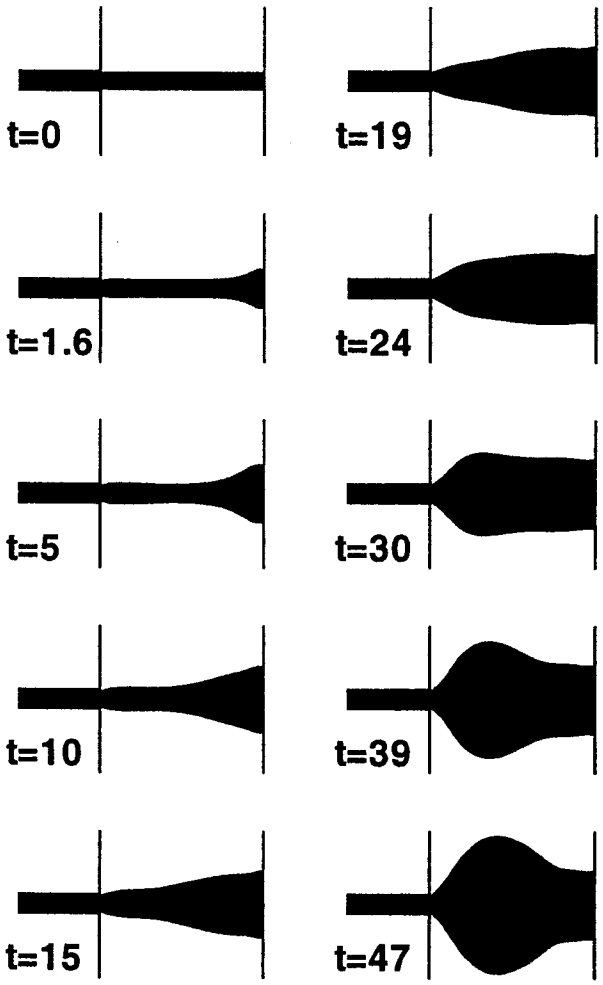

Figure 9: Stable jet behavior, $Re = 5$, $Bi = 1$, $L = 10$. The disturbance is imposed from $t = 0$ until $t = 1.5$.

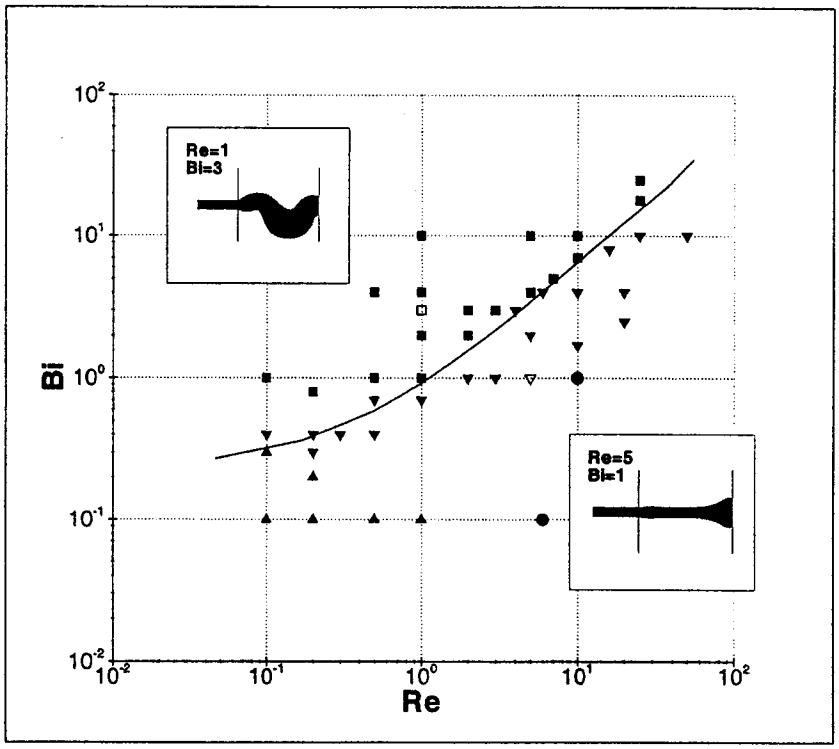

Figure 10: Stability of the jet when hitting a vertical suface ($L = 10$), the Reynolds and Bingham numbers being the control parameters. ▲-"mound" pattern; ●-"disk" pattern; ■-"bubble" pattern; ▼-"transition" pattern. The hollow symbols (□, and ▽) represent the cases discussed in detail and pictured on the map. The estimated boundary between the stable and unstable behaviors has been sketched in. Stable and unstable behaviors are respectively below and above this limiting line.

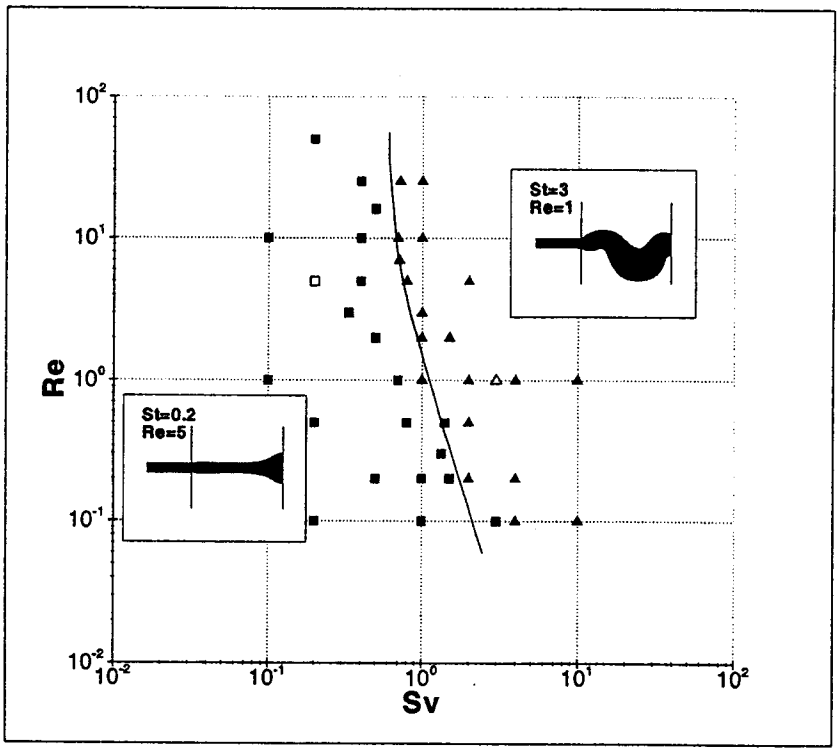

Figure 11: Stability of the jet when hitting a vertival surface ($L = 10$), the Saint-Venant and Reynolds numbers being the control parameters. ■-stable pattern; ▲-unstable pattern. The hollow symbols (□ and △) represent the cases pictured on the map. The estimated boundary between the two behaviors has been sketched in.

thickness each were cut directly from the billets. Figure 1 illustrates the experimental procedures.

Table I: Chemical composition of the alloys investigated

Alloy	Composition, %				
	Si	Mg	Cu	Mn	Fe
A356 (MHD)	6.92	0.18	0.09	0.05	0.1
A356 (GR)	6.85	0.33	0.11	0.05	0.1
SiBloy (GR)	6.84	0.29	0.0005	0.003	0.07
A357 (SIMA)	6.61	0.53	--	0.01	0.1
A356 (MIT)	7.27	0.38	0.01	---	0.1
Al-Si-Cu (UBE)	---	---	---	---	---

1.2 Processing Conditions

Processing conditions investigated in this study include continuous heating and quenching samples at different temperatures in the two-phase region, as well as isothermal holding at 582°C and quenching samples at different holding time, as shown in Figure 2.

The ***first series*** of experiments dealt with the effect of processing temperature on semi-solid microstructure during continuous heating in the semi-solid state. The average heating rate was about 49^0C/min.

The ***second series*** of experiments were designed to investigate the effect of isothermal hold on microstructural evolution at a temperature commonly used in commercial forming operations (582°C). Holding time varied from 1 to 64 minutes.

1.3 Microstructure Characterization

Metallographic observations were made on the water-quenched samples. The specimens were etched with Keller's reagent after mounting, grinding, and polishing.

Microstructure characterization was performed using optical microscopy and image analyzer (microGOP2000/S). Three specific microstructural parameters

were measured to quantitatively characterize the semisolid microstructures. They are

1. particle size of the Alpha phase, *D*
2. shape factor of the Alpha particles, *SF*
3. entrapped liquid content within the Alpha particles, V_f

The particle size (*D*) is determined by

$$D = 2 \times \sqrt{\frac{A}{\pi}} \tag{1}$$

Where *A* is the area of the particle. The average particle size is the mean value of the total numbers of particles measured.

The shape factor (*SF*) is defined as

$$SF = \frac{P^2}{4\pi A} \tag{2}$$

Where *P* is the perimeter of the particle. For a perfectly globular shape, *SF* is equal to 1. The more irregular the particles, the higher the shape factor value. The shape factor values reported here are the mean values of the total numbers of particles measured.

Specifically, we found that there are two types of entrapped liquid in nature. One is entrapped within Alpha particles in isolation, and the other is entrapped within the Alpha particles in 2D, but is connected to the intergranular eutectic in 3D. The entrapped liquid content (V_f) here is defined as

$$V_f = \frac{A_{EL}}{A_{Liquid}} \times 100\% \tag{3}$$

Where A_{EL} is the area of the entrapped liquid in isolation, A_{Liquid} is the area of the entire liquid phase including the intergranular eutectic phase, the entrapped liquid in isolation, as well as the entrapped liquid in connection to the intergranular eutectic. Since most entrapped liquid has a spherical shape, here the mean entrapped liquid content in 2D can be considered as an approximate volume fraction value in 3D.

In order to obtain results of statistical significance, more than twelve images were measured for each sample. In addition, since there is significant difference in

microstructural scale throughout MHD A356, GR A356 and SiBloy as-cast billets, we analyzed semi-solid microstructures at twelve different locations on the cross section, which cover the whole region within a radius.

2. RESULTS & ANALYSIS

Microstructural evolution of various semi-solid billets as a function of material genealogy and processing temperature is presented below in section 2.1. Microstructure evolution as a function of material genealogy and isothermal holding time at 582°C is presented in section 2.2. This is followed by analysis on formation mechanism of the entrapped liquid within the Alpha phase.

2.1 Microstructural Evolution During Continuous Reheating

From a rheological standpoint, an "ideal" semi-solid microstructure is composed of small, round Alpha particles containing no entrapped liquid and homogeneously distributed in a eutectic phase, as illustrated in Figure 3. The small size of the Alpha particles is beneficial for the casting of thin-walled parts, while a more spherical shape, and the absence of entrapped liquid are critical for the improvement of the slurry flow properties during die filling.

Figure 4 compares typical as-cast microstructures of various semi-solid billets. It can be seen that their as-cast microstructures are quite different. The as-cast microstructure of GR billets (by addition of Ti-B or Si-B alloys) is a dendritic structure with a very fine scale, while the microstructure of MHD billets is a mixture of dendritic and rosette-like structures. SIMA billets show typical deformed microstructure with a lot fine Mg_2Si particles. The new MIT processed billets, however, have a globular Alpha structure, which is formed due to a rapid mechanical stirring and a strict cooling rate control during billet casting.

Upon reheating, the above billets show quite different microstructural evolution. Figures 5 and 6 give the typical semi-solid microstructures of all these billets at 580°C and 585°C, respectively. Visually, there are significant differences among them in terms of the shape and size of the Alpha particles, as well as the entrapped liquid content within the Alpha phase. Detailed image analysis results are given below.

2.1.1 Entrapped Liquid Content

The entrapped liquid within the Alpha phase has a significant influence on the rheological behavior of semi-solid slurry. As the entrapped liquid does not participate in the deformation during die filling, it has the effect of decreasing "effective" liquid fraction, and thus flow properties.

Figure 7 details the evolution of entrapped liquid as a function of processing temperature and material genealogy. It can be seen that

- GR billets (by addition of Ti-B or Si-B alloys) have much higher entrapped liquid content than MHD billets. The entrapped liquid content in Ti-B refined billets can account for as high as 36% of the liquid phase at 578°C. During commercial forming temperature range between 580-590°C, the entrapped liquid content in GR billets varies between 15-30%, which is 2-3 times higher than in MHD billets

- Processing temperature has a significant influence on the entrapped liquid content of GR billets. With increasing temperature, the entrapped liquid content decreases dramatically, however, processing temperature shows little effect on the entrapped liquid content of MHD and SIMA billets.

- No entrapped liquid was found in MIT and UBE processed billets.

2.1.2 Particle Size

Figure 8 details the evolution of particle size as a function of processing temperature and material genealogy. The quantitative data shows that

- Higher processing temperature tends to increase particle size, but the effect is not significant in commercial forming temperature range (580-590°C).

- The Alpha particle size in grain refined billets (by addition of Ti-B or Si-B alloys) is much larger than in MHD, SIMA and MIT processed billets. Among them, the SIMA billets have the smallest Alpha particle size, and very uniform size distribution, falling in the range between 50-80 μm in the temperature range investigated.

- Interestingly, processing temperature has no influence on Alpha particle size of Si-B grain refined billets (SiBloy). In addition, compared to Ti-B grain refined billets (GR A356), the particle size distribution in Si-B refined billets is more uniform.

2.1.2 Shape Factor

Figure 9 details the evolution of shape factor as a function of processing temperature and material genealogy. It can be seen that

- During commercial forming temperature range (580-590°C), shape factor values of all the semi-solid billets decrease with increasing temperature, indicating that higher forming temperature leads to a better spheriodization of Alpha particles.

- As shown in Figure 9, SIMA billets have the smallest shape factor value, corresponding to the best spheroidized Alpha particles. Whereas, Si-B refined billets have the highest shape factor value, thus corresponding to the most irregular shape of Alpha particles. This is consistent with microstructure observations.

2.2 Microstructural Evolution During Isothermal Holding at 582°C

Figures 10 and 11 give the semi-solid microstructures of various billets isothermal holding for 2 minute, and 32 minute, respectively. A rapid evolution of Alpha particles towards a globular structure was seen in MHD, SIMA and MIT billets, whereas relatively slow spheroidization was observed in GR billets. This can be clearly seen from the image analysis results given below.

2.2.1 Entrapped Liquid Content

Figure 12 gives the evolution of entrapped liquid content as a function of isothermal holding time and material genealogy. The results show that

- Isothermal holding has a significant effect on the entrapped liquid content of GR billets (by addition of Ti-B or Si-B alloys). With increasing isothermal holding time, the entrapped liquid content decreases considerably.

- Isothermal holding, however, shows little influence on the entrapped liquid content of MHD and SIMA processed billets. Again, no entrapped liquid was found in MIT processed billets under isothermal holding conditions.

2.2.2 Particle Size

Figure 13 gives the evolution of particle size as a function of isothermal holding time and material genealogy.

- As expected, isothermal holding leads to coarsening of Alpha particles. Specifically, a good linear dependence between particle size and isothermal holding time was found in GR (by addition of Ti-B alloys), MHD, MIT and SIMA processed billets.

- Interestingly, isothermal holding does not show any influence on the particle size of Si-B refined billets. With increasing isothermal holding time, the particle size of Si-B refined billets tends to a constant value (around 160 μm), even isothermal holding for 64 minutes.

- The insensitivity of particle size in Si-B grain refined billets to both processing temperature and isothermal holding time is most likely related to the long-term grain refinement effect of Si-B alloys found by ACRC researchers.

2.2.3 Shape Factor

Figure 14 gives the evolution of shape factor as a function of isothermal holding time and material genealogy. It can be seen that

- A rapid spheroidization process usually occurs in the first 1-2 minute isothermal holding, and thereafter, the process proceeds very slowly.

- Si-B and Ti-B grain refined billets have higher shape factor values than the other billets, corresponding to a more irregular shape of Alpha particles. Moreover, isothermal holding shows little effect on the spheroidization of Alpha particles in GR billets, particularly for Si-B grain refined billets.

- Specifically, a significant difference in shape factor values has been observed throughout the grain refined billets. Usually, the microstructures at billet center have higher shape factor values than those at billet edge, indicating that the speroidization process at billet center is relatively slow.

2.3 Entrapped Liquid Analysis

As stated before, the entrapped liquid within the Alpha particles does not participate in the deformation during die filling, thus it greatly decreases the flow properties of the semi-solid slurry. Moreover, since no feeding is available during the subsequent solidification process, the entrapped liquid may cause casting defects such as microporosity, shrinkage etc. Therefore, an understanding of origin and nature of the entrapped liquid is critical.

Figures 15 through 16 show typical morphologies of the entrapped liquid within the Alpha phase under both microscope and SEM. It is clear that

- The entrapped liquid has different morphologies (see Figure 15). One typical morphology is circular. Others include irregular shapes such as triangle, rectangular or ellipse, etc.

- The morphology and amount of the entrapped liquid is strongly dependent on the as-cast microstructure of the billet. A fine dendritic as-cast structure tends to form high volume of entrapped liquid with both circular and irregular shapes, while a rosette-like as-cast structure gives rise to intermediate volume of globular entrapped liquid. If the as-cast billet has a spherical Alpha phase (for example, the MIT billet), one can obtain semi-solid microstructure completely free of the entrapped liquid upon reheating (compare Figure 4d with Figures 5d and 6d).

- Specifically, SEM observations clearly show that there are two types of entrapped liquid in nature. As shown in Figure 16(a), one is entrapped in isolation within the Alpha particles, and the other is entrapped in 2D but is connected to the intergranular eutectic in 3D. This can be easily identified by a comparison between the entrapped liquid and the intergranular eutectic. In fact, the entrapped liquid, which is connected to the intergranular eutectic in 3D, has exactly the same morphology as the intergranular eutectic phase.

- More importantly, an enlarged view of the entrapped liquid in isolation reveals that the entrapped liquid indeed consists of many extremely fine eutectic grains, as shown in Figure 16(b). The grain size is in order of several micrometers.

- Further SEM and EDAX analysis points out that there are many small oxide spheroids inside each eutectic grain, as shown in Figure 16(c). The small spheroids serve as nuclei for eutectic grains, thus leading to the formation of the extremely fine eutectic grains.

Based on the above observations, it is logical to assume that the origin of the entrapped liquid is due to the coalescence of the broken dendritic arms formed either by MHD or grain refinement treatment. Compared to rosette-like structure, the fine dentritic structure tends to entrap more liquid and form more irregular shapes during the coalescence upon reheating, and that's why the GR billets have much more entrapped liquid, and the entrapped liquid has more irregular shapes than MHD billets.

Obviously, our findings clarify some conflicting claims as to whether the entrapped liquid is connected to the rest of the eutectic or it is entrapped in isolation. Still, there are some issues remaining open.

- Where do the oxide spheroids come from? They come from the broken oxide film during billet casting? or from the oxidization due to the addition of Sr?

- Specifically, we observed that most modified eutectic silicon grows from the oxide films. Is this a new mechanism for modification of the eutectic silicon?

Further experiments are being carried out to try to answer these questions.

3. CONCLUSIONS

Based on our extensive microstructural observations and quantitative data, the following conclusions were drawn:

1. The chemically grain refined billets have relatively high entrapped liquid content. During commercial forming conditions, the entrapped liquid content usually accounts for 15-30% of the total liquid phase for grain refined billets, and 8-15% for SIMA and MHD billets.

2. The formation of the entrapped liquid can be attributed to the coalescence of the broken dendrite arms upon reheating. SEM analysis reveals that there are two types of entrapped liquid in nature. One is entrapped in isolation within the Alpha phase, and the other is entrapped in 2D but is connected to the intergranular eutectic in 3D. Specifically, we found that the isolated entrapped liquid consists of extremely fine eutectic grains (in order of several micrometers), and a lot of small oxide spheroids have been identified as the nuclei for the fine eutectic grains.

3. Higher processing temperature tends to decrease shape factor value and entrapped liquid content, however, it also increases the Alpha particle size and the runoff of liquid phase during semi-solid forming. A favorite temperature range for aluminum semi-solid billets is between 580-590°C. For grain refined billets, 585-590°C is recommended.

4. Isothermal holding leads to a speroidization and a coarsening process of Alpha particles. Analysis on quantitative data points out that an optimum isothermal holding time is between 2-8 minutes. For grain refined billets, the upper limit is recommended.

5. Specifically, both processing temperature and isothermal holding have a significant influence on the entrapped liquid content of GR billets. Increasing processing temperature or isothermal holding time decreases entrapped liquid content of GR billets considerably. However, processing temperature and isothermal holding time show little effect on the entrapped liquid content of SIMA and MHD billets.

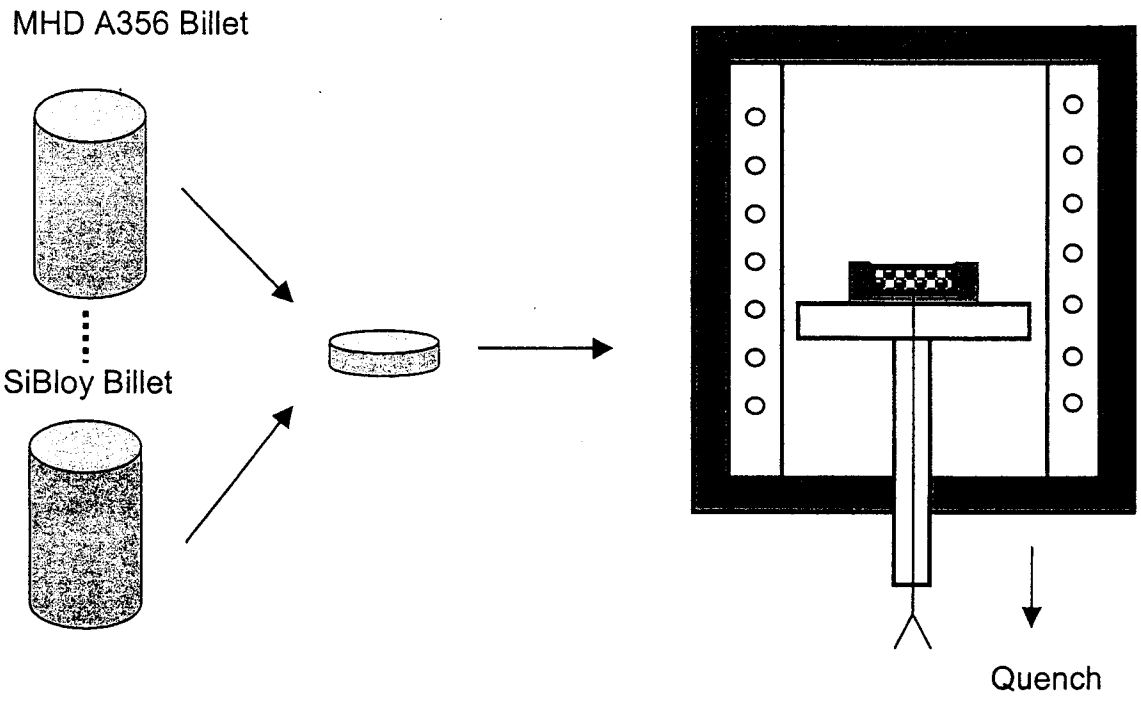

Figure 1: Schematic diagram of experimental procedures.

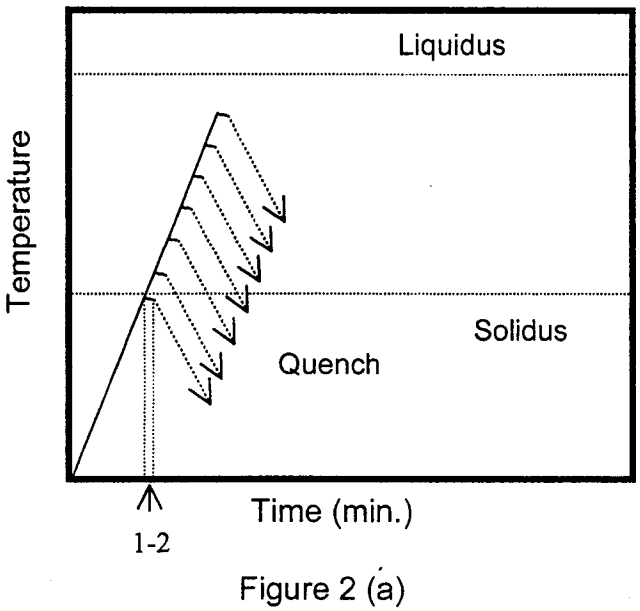

Figure 2 (a)

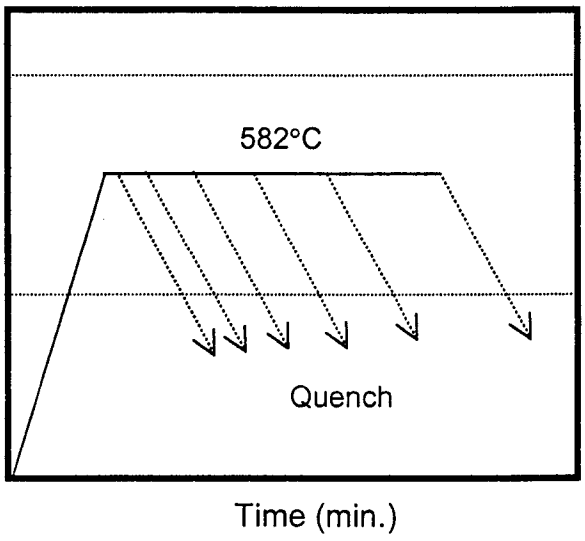

Figure 2 (b)

Figure 2: Schematic diagram of thermal treatments applied, (a) continuous reheating, and (b) isothermal holding.

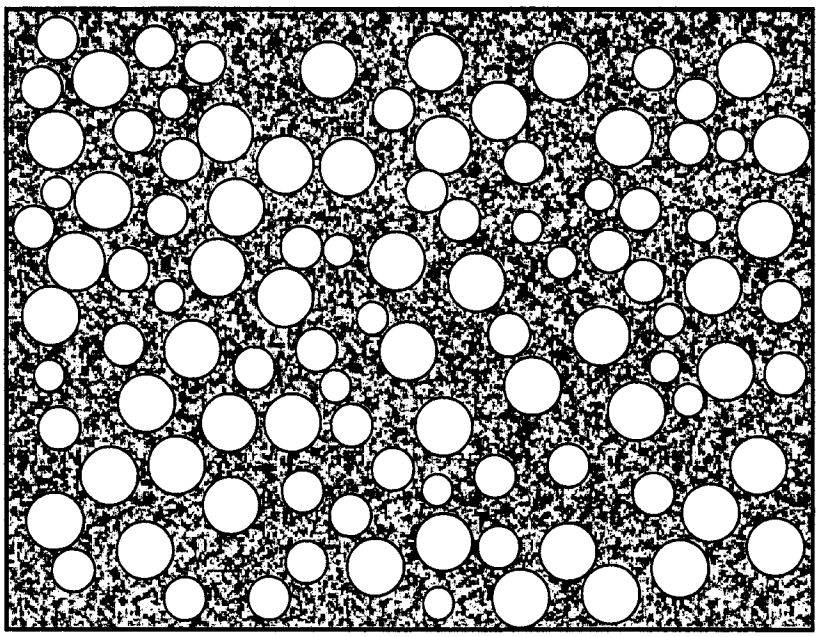

Figure 3: Schematic diagram of an “ideal” semi-solid structure.

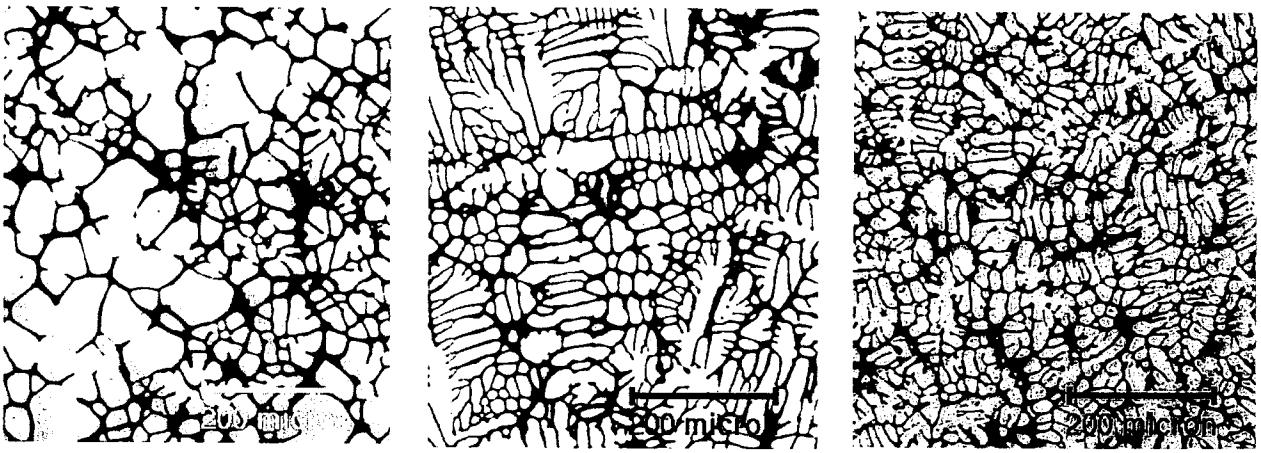

(a) MHD A356 (b) GR A356 (c) SiBloy

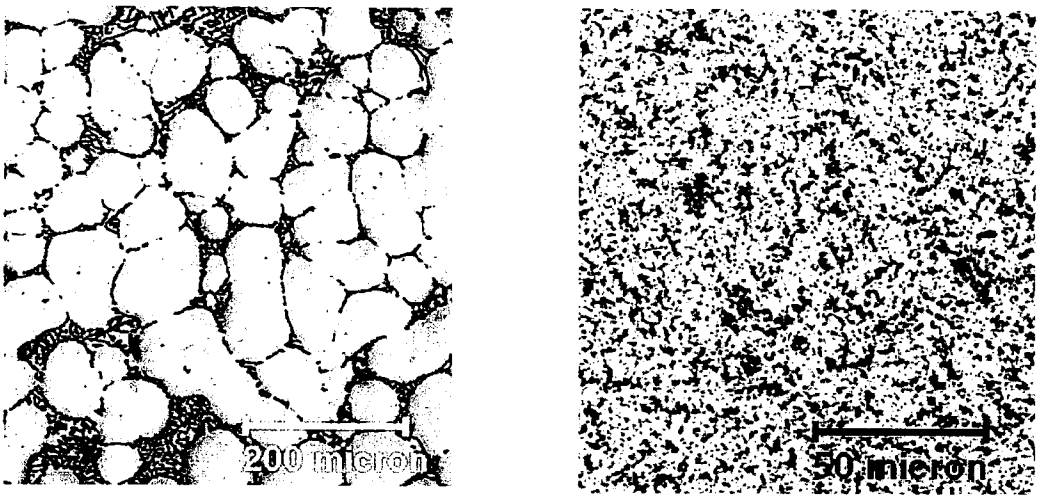

(d) MIT A356 (e) SIMA 357

Figure 4: As-cast microstructure of various semi-solid billets.

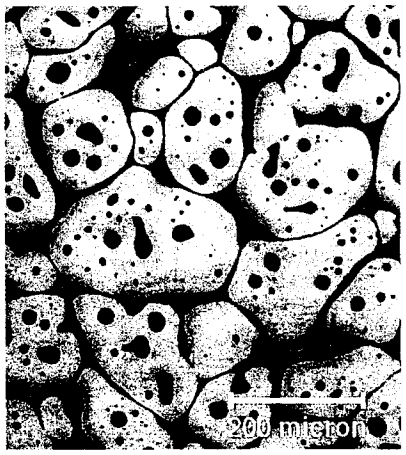

(a) MHD A356

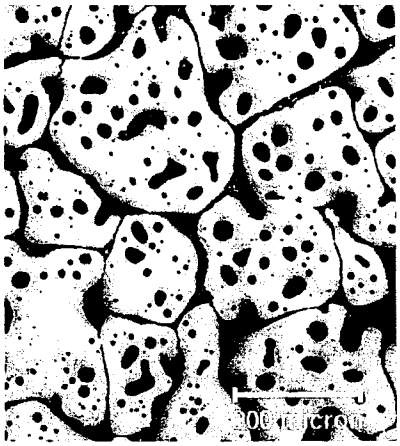

(b) GR A356

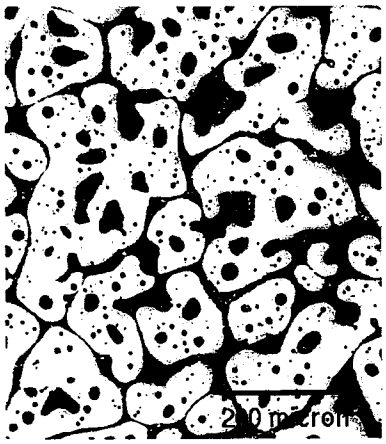

(c) SiBloy

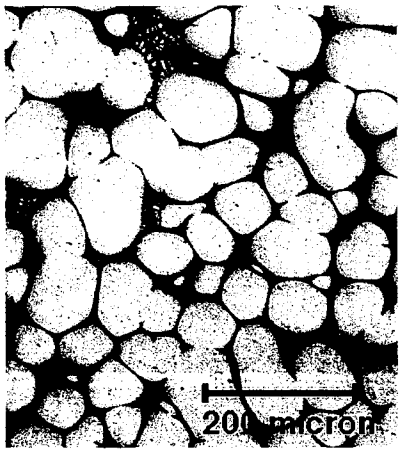

(d) MIT A356

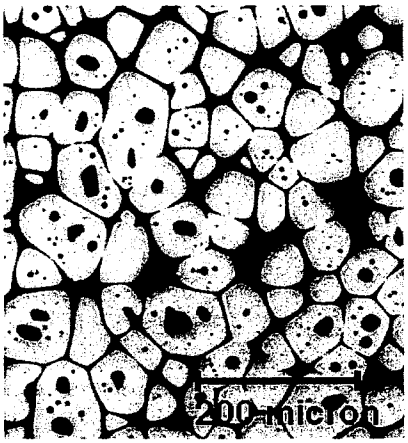

(e) SIMA A357

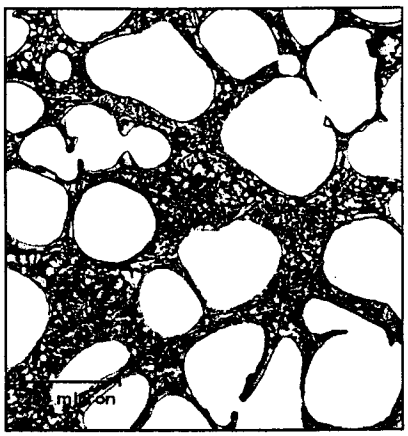

(f) UBE (Al-Si-Cu)

Figure 5: Semi-solid microstructure of various billets at 580°C.

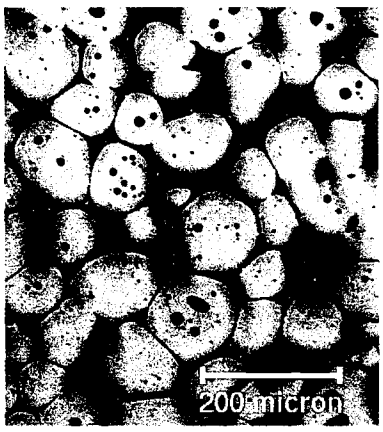

(a) MHD A356

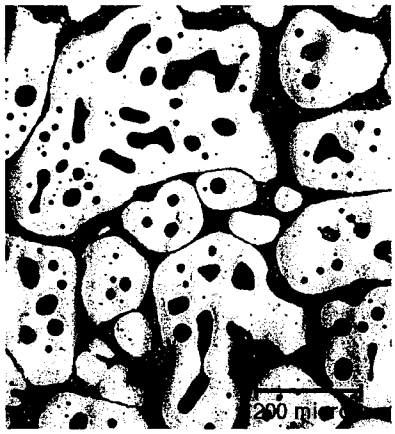

(b) GR A356

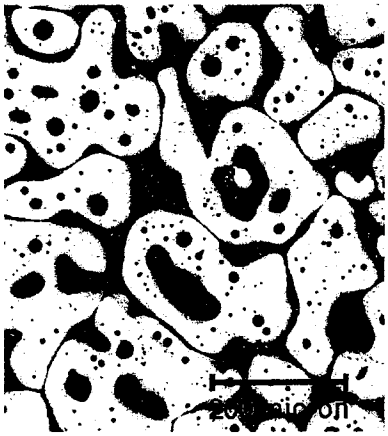

(c) SiBloy

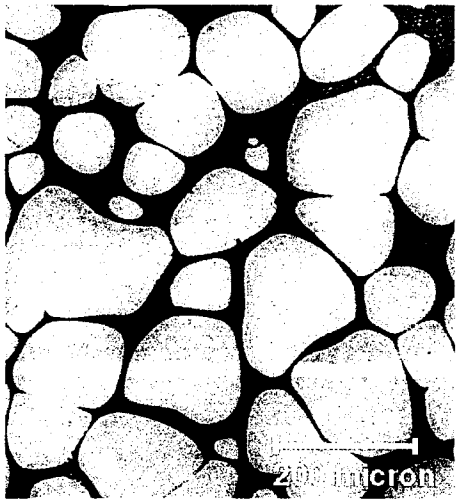

(d) MIT A356

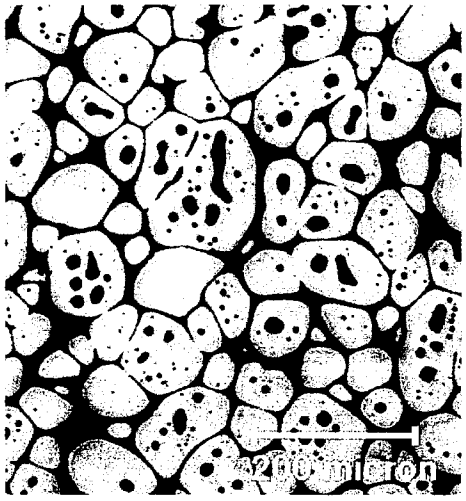

(e) SIMA 357

Figure 6: Semi-solid microstructure of various billets at 585°C.

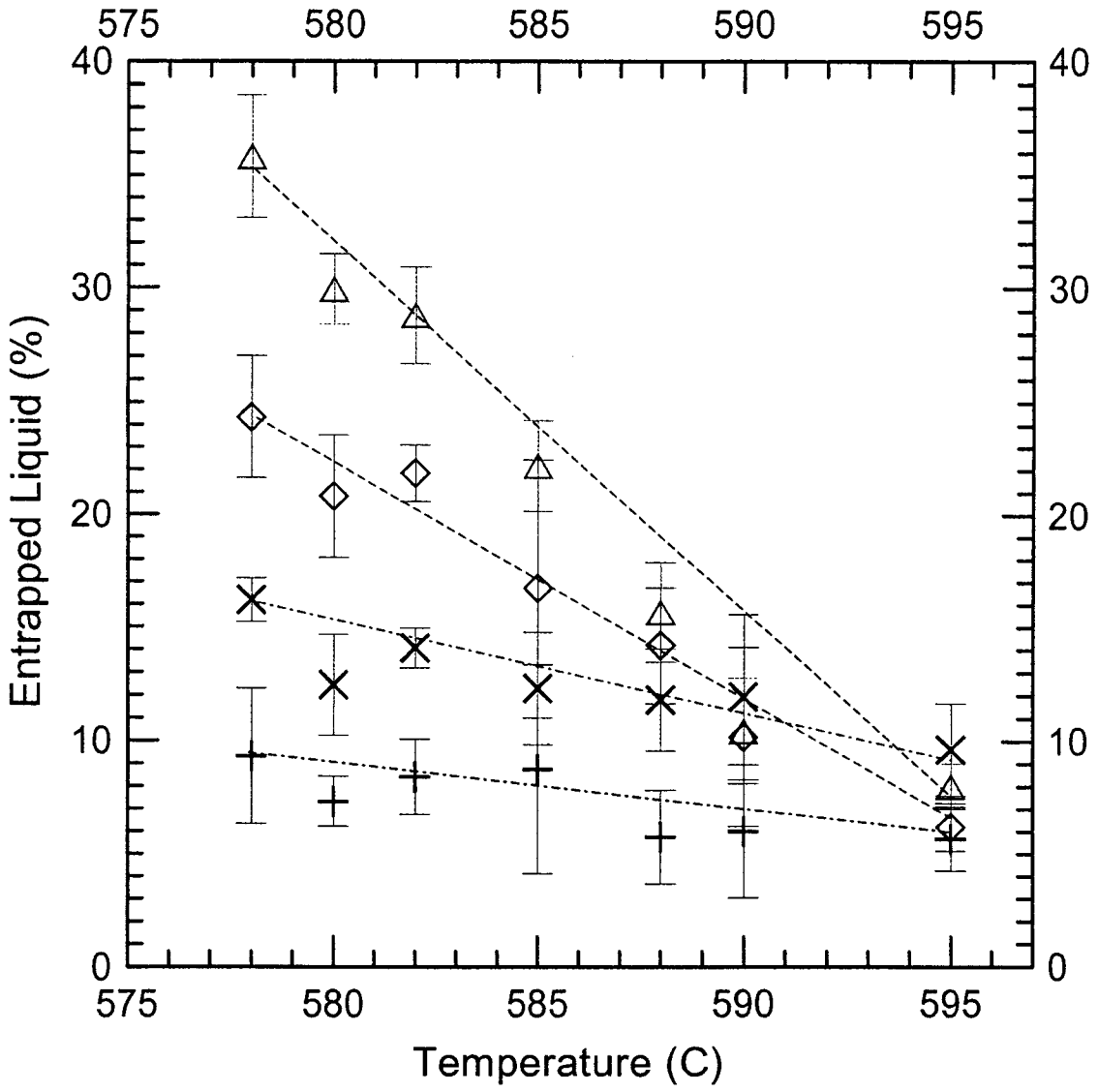

Figure 7: Evolution of entrapped liquid content as a function of processing temperature and material genealogy.

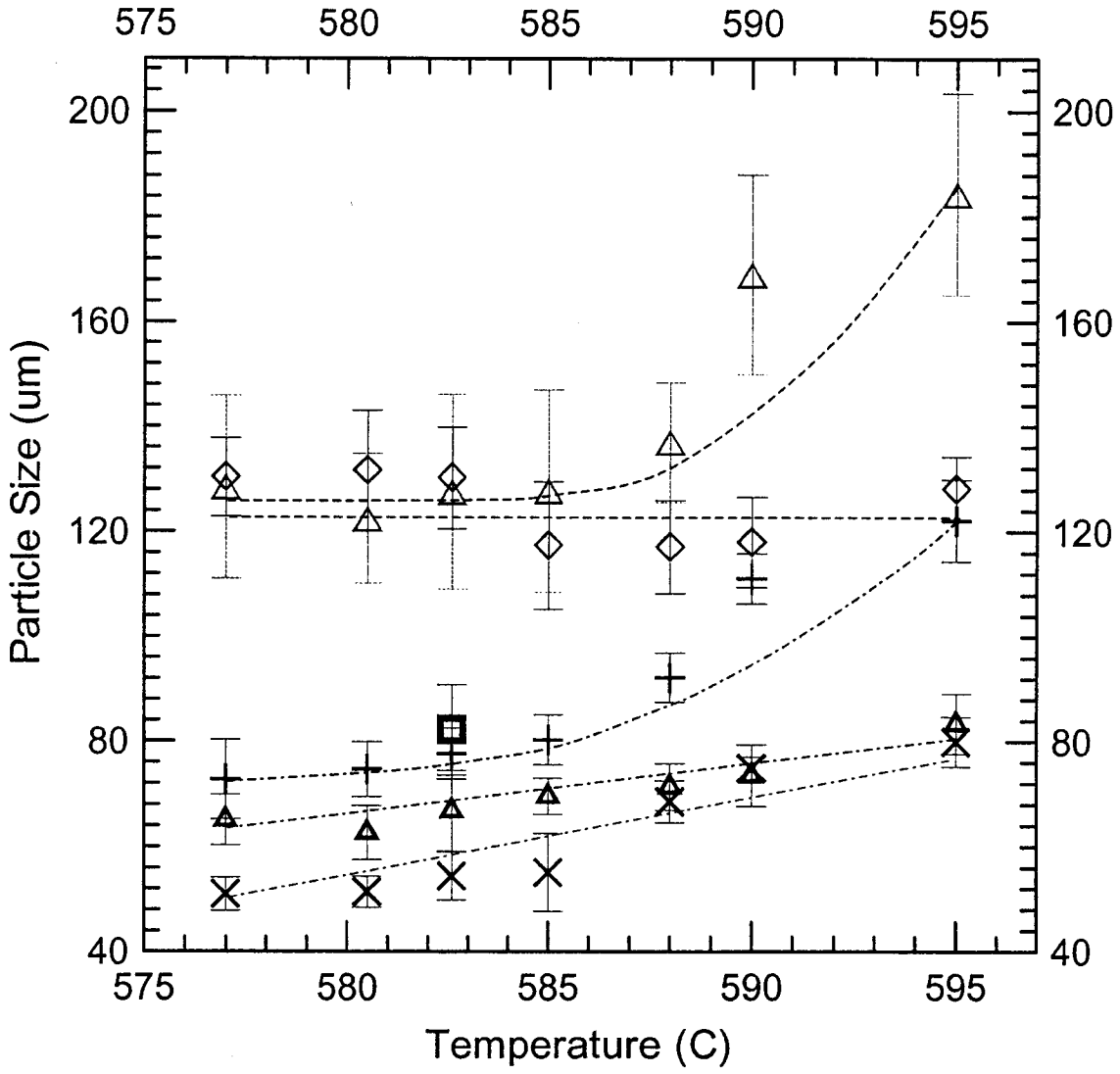

Figure 8: Evolution of particle size as a function of processing temperature and material genealogy.

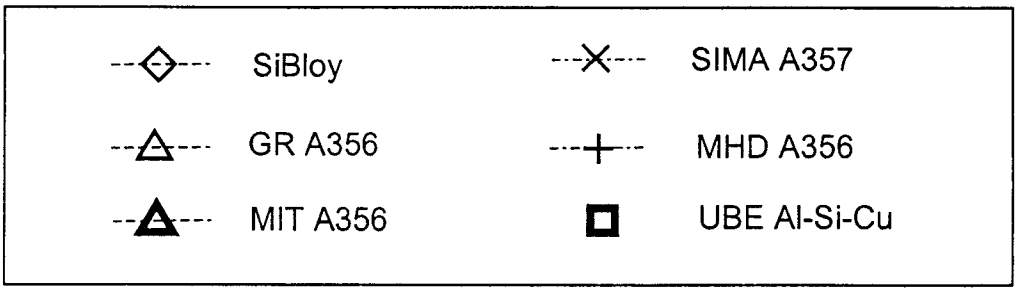

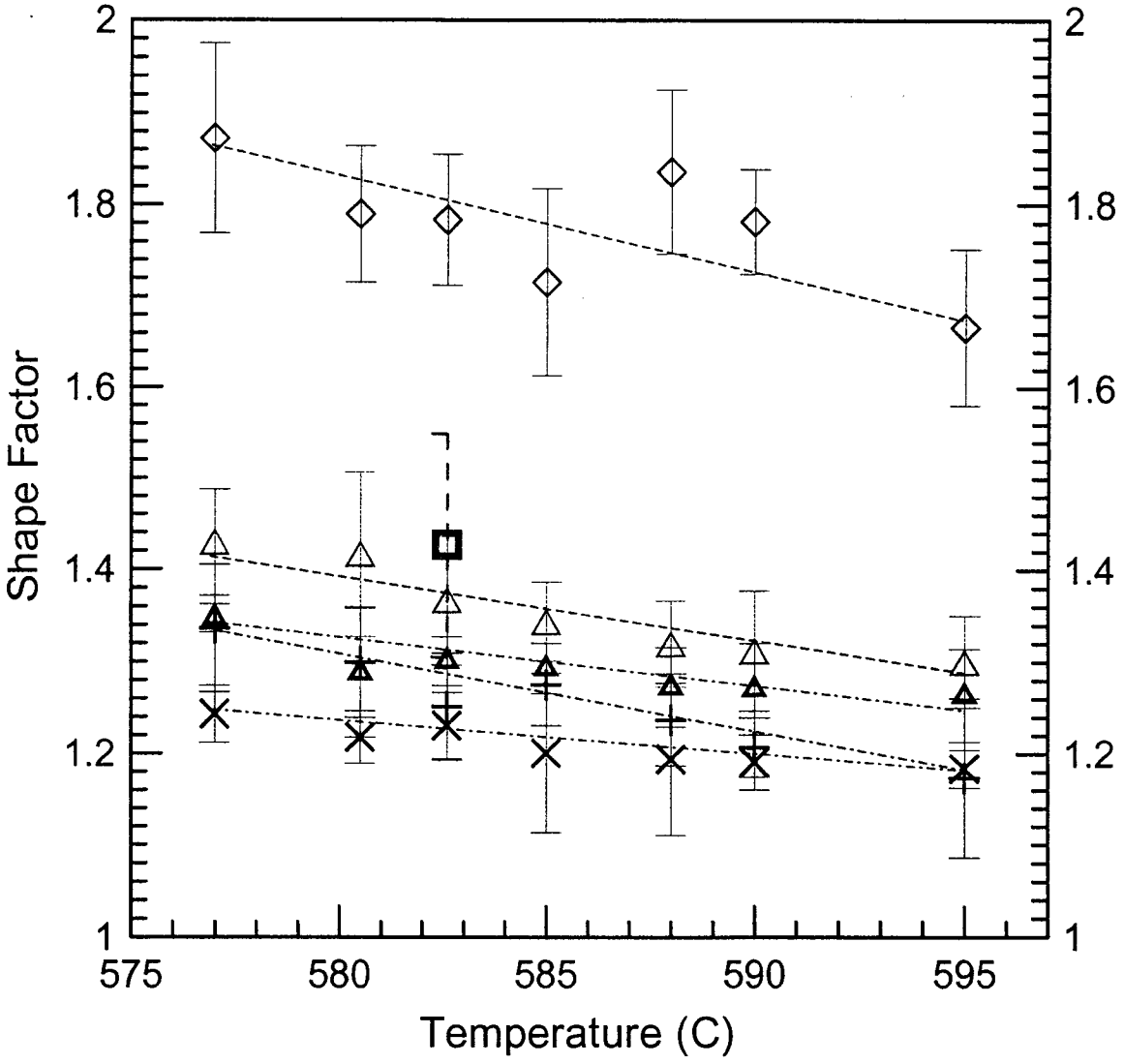

Figure 9: Evolution of shape fator as a function of processing temperature and material genealogy.

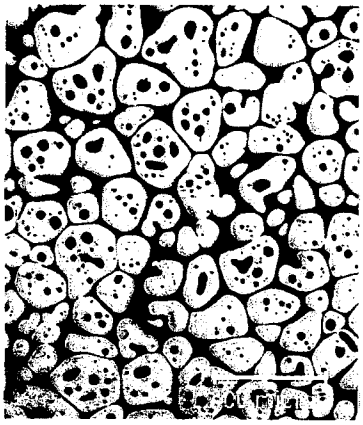

(a) MHD A356

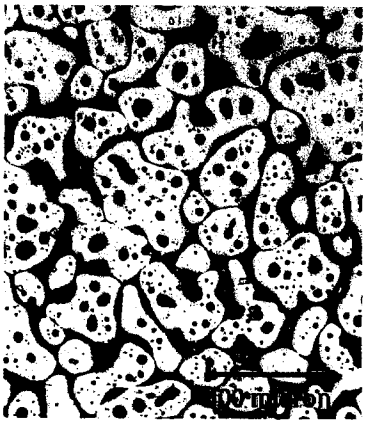

(b) GR A356

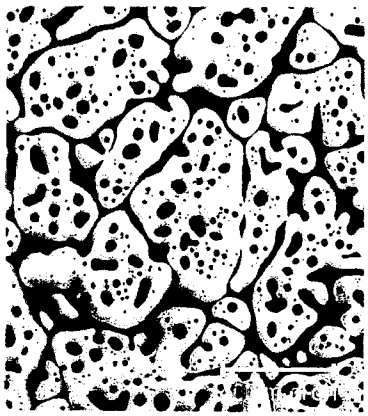

(c) SiBloy

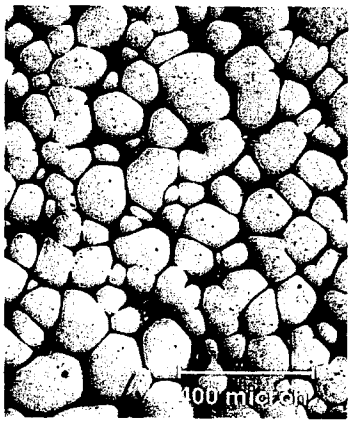

(d) MIT A356

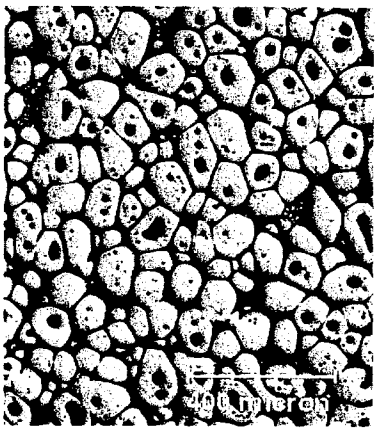

(e) SIMA 357

Figure 10: Semi-solid microstructure of various billets at isothermal holding for 2 minutes at 582°C .

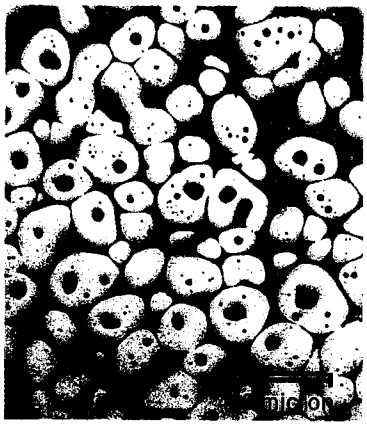

(a) MHD A356

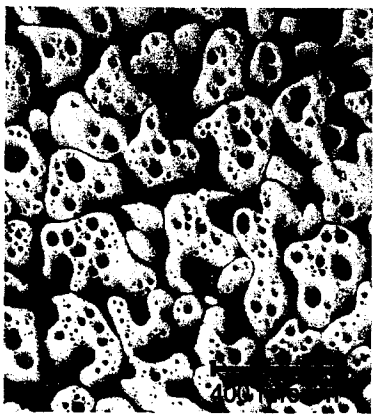

(b) GR A356

(c) SiBloy

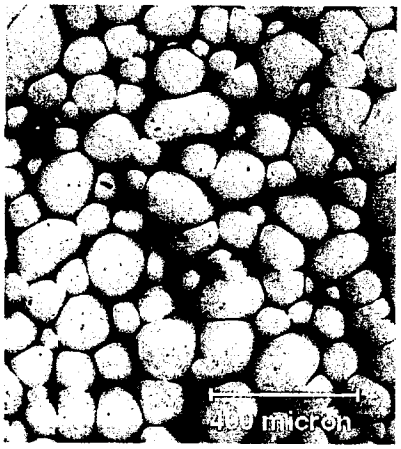

(d) MIT A356

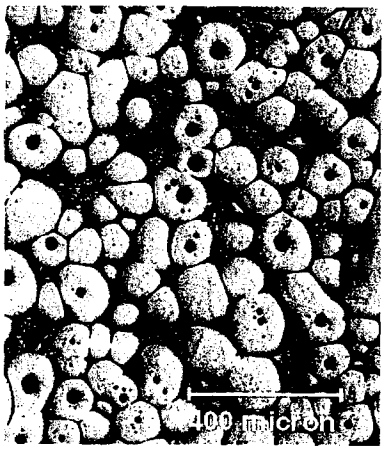

(e) SIMA 357

Figure 11: Semi-solid microstructure of various billets at isothermal holding for 32 minutes at 582°C .

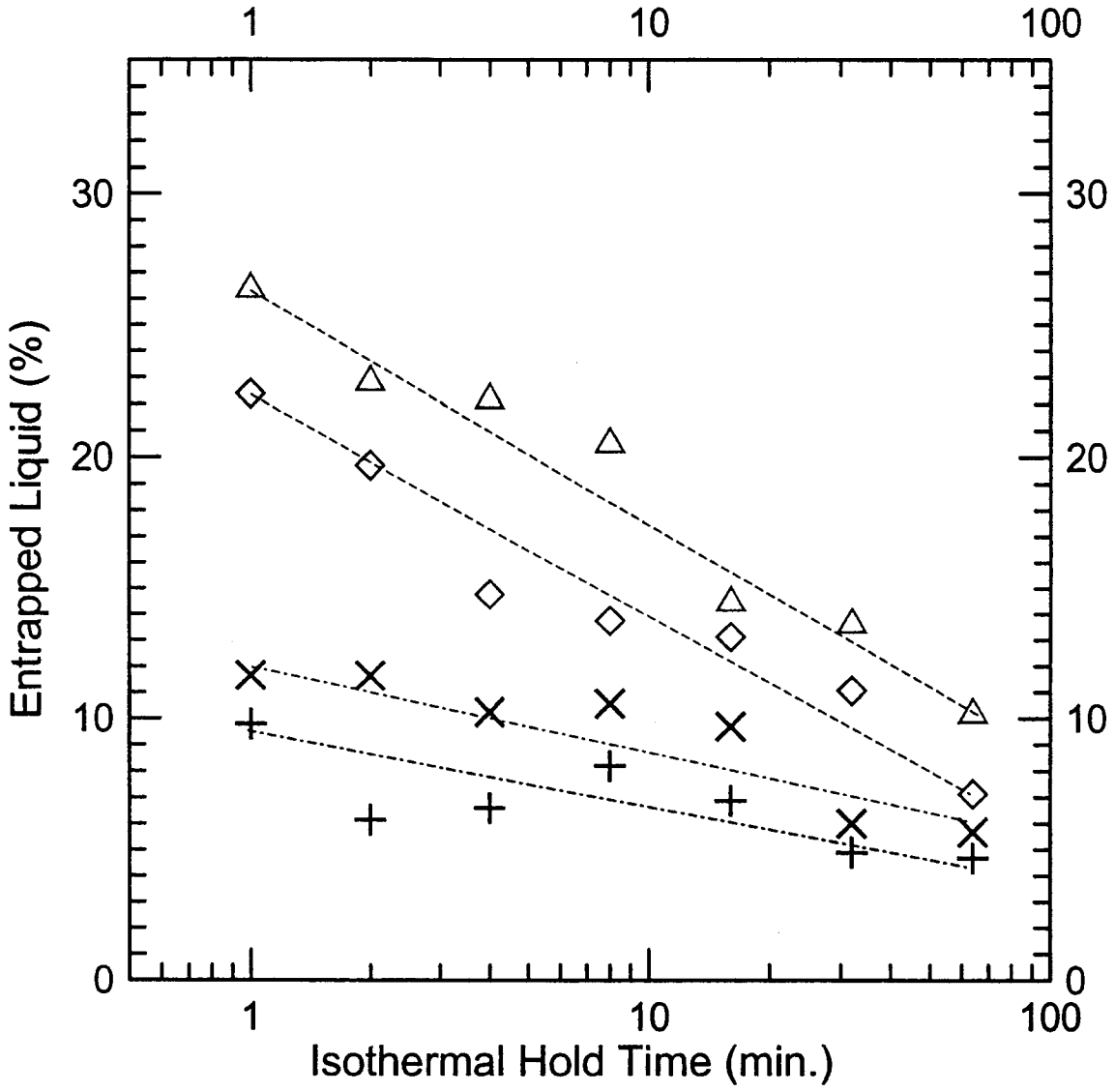

Figure 12: Evolution of entrapped liquid content as a function of material genealogy and isothermal hold time at 582°C.

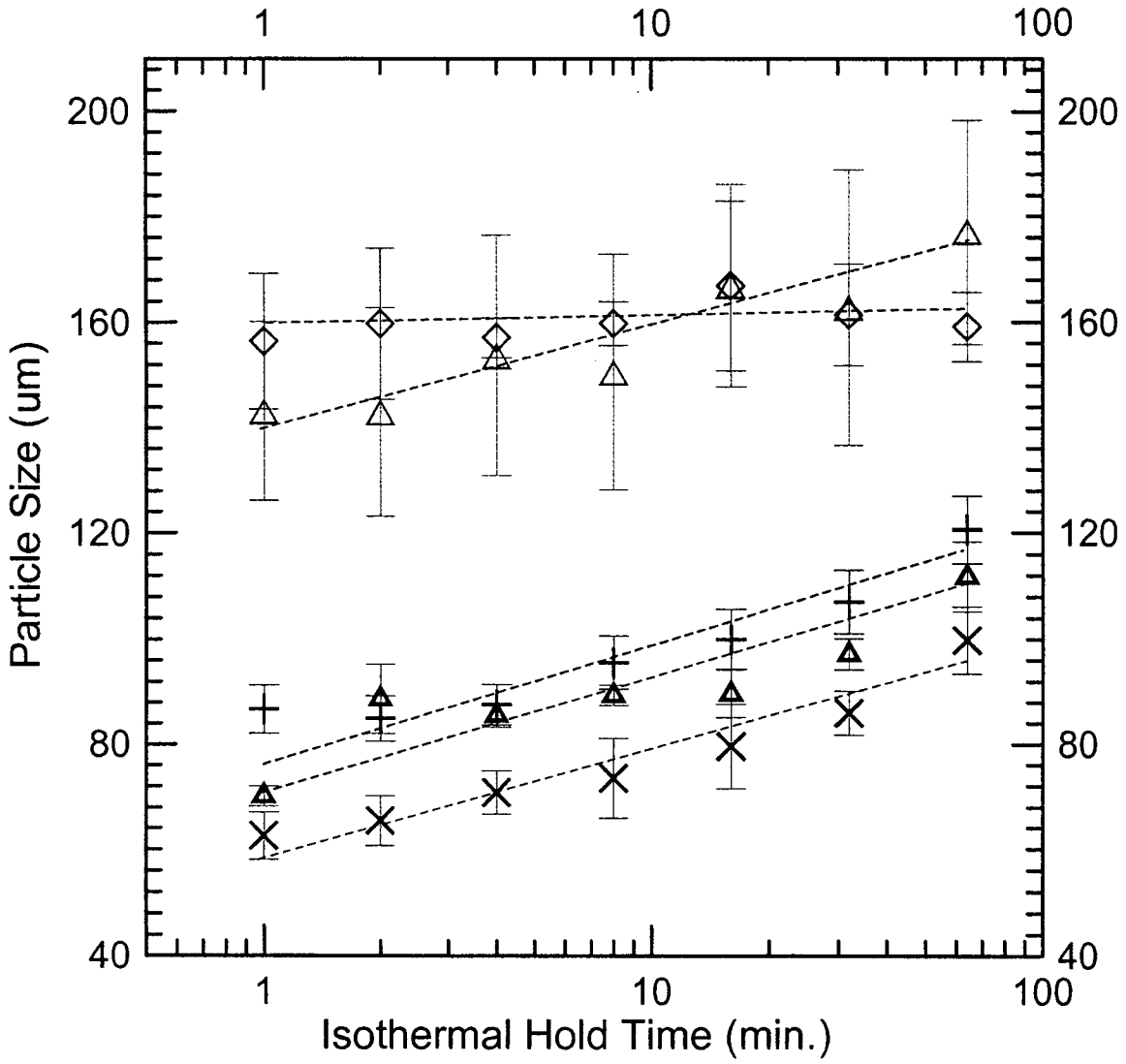

Figure 13: Evolution of particle size as a function of material genealogy and isothermal hold time at 582°C.

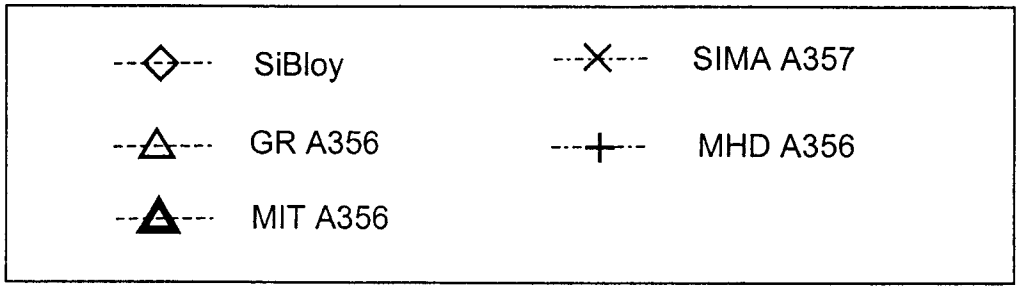

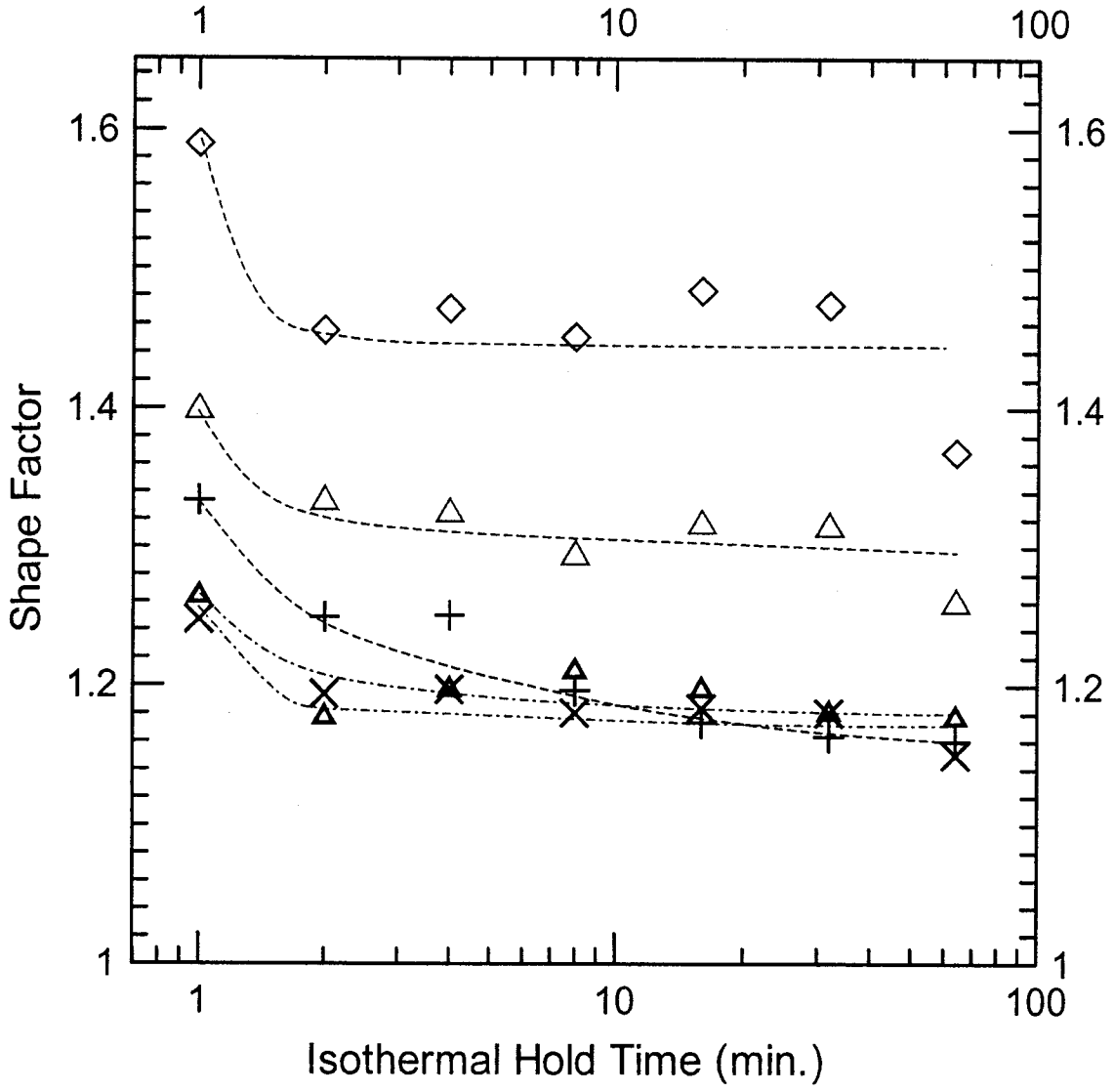

Figure 14: Evolution of shape factor as a function of material genealogy and isothermal hold time at 582°C.

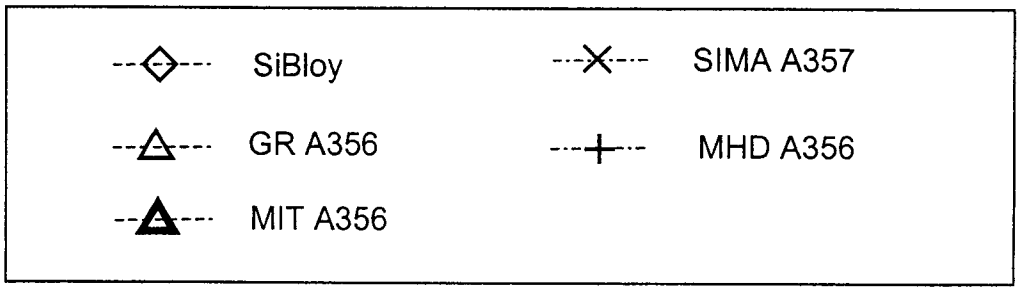

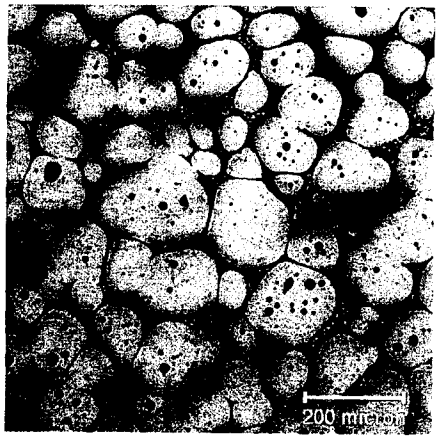

(a) MHD A356 at 578°C

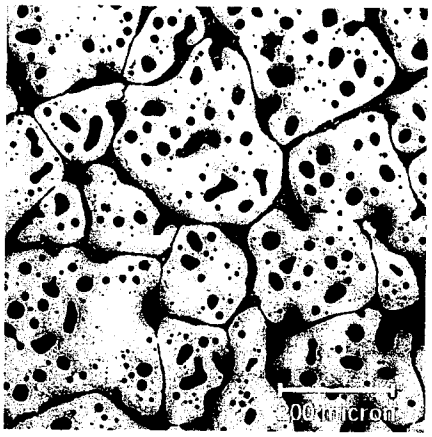

(b) GR A356 at 578°C

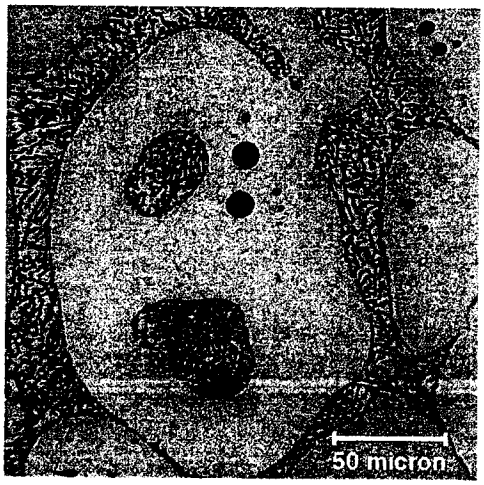

(C) Enlarged view of the entrapped liquid

Figure 15: Different morphologies of the entrapped liquid.

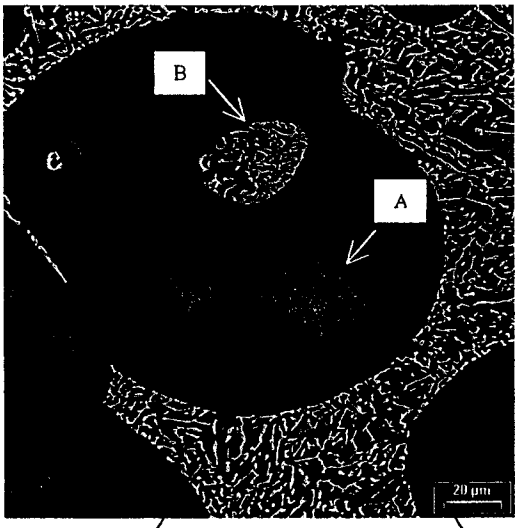

(a) GR A356 at 578°C, Keller's reagent

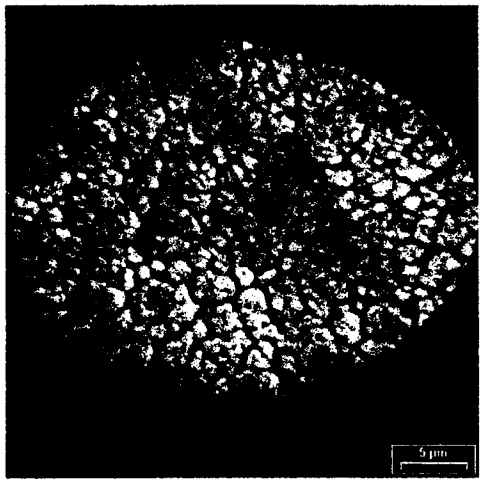

(b) Enlarged view of type A entrapped liquid, Keller's reagent.

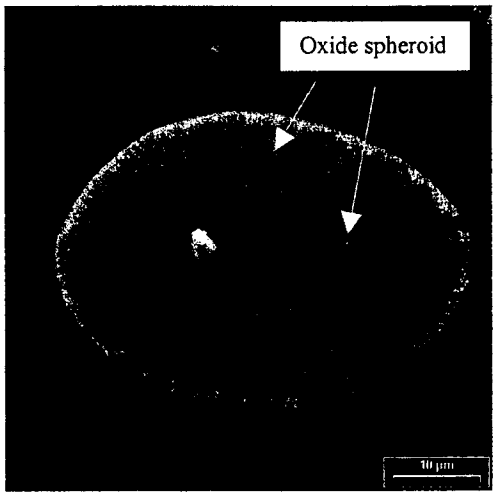

(c) Enlarged view of type A entrapped liquid, electropolishing.

Figure 16: SEM microstructure of the entrapped liquid, showing (a) two types of entrapped liquid in nature; (b) extremely fine eutectic grains, and (c) the nuclei-some oxide spheroids in each eutectic grain.

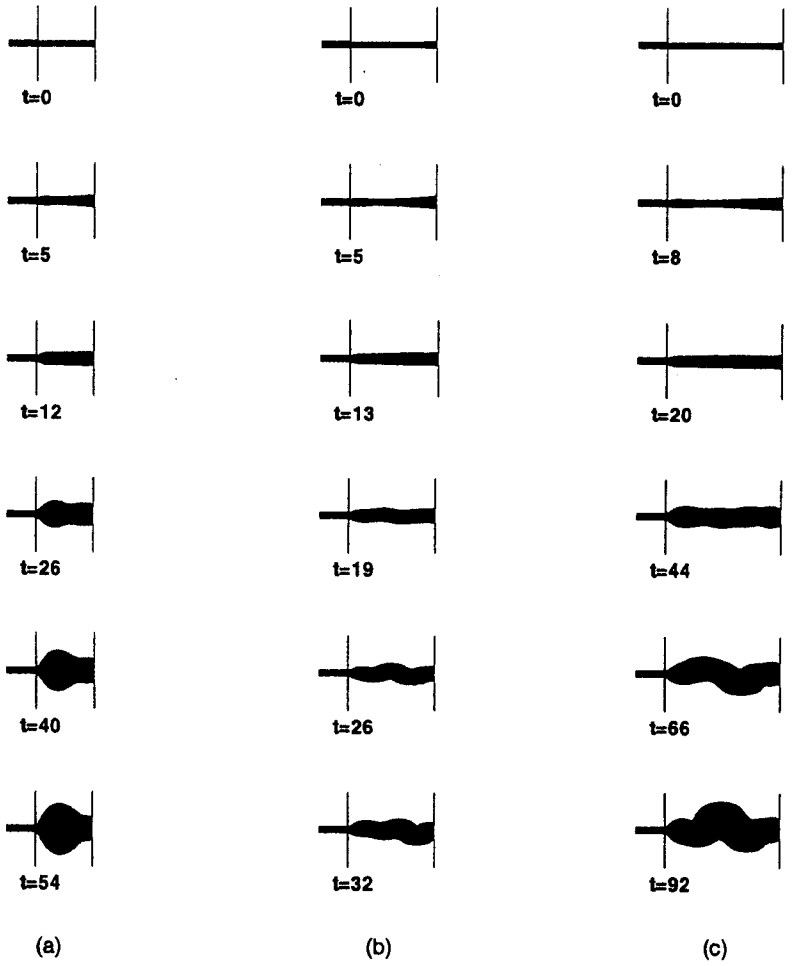

Figure 12: Stability of the flow ($Re = 1, Bi = 0.7$) for three different jet lengths. (a) $L = 10$, (b) $L = 15$, (c) $L = 20$.

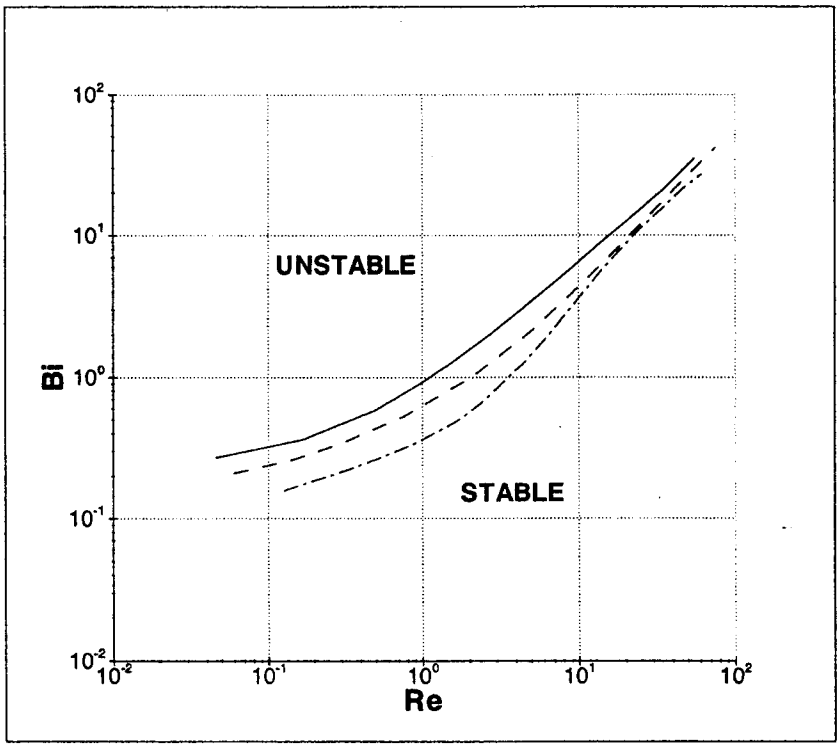

Figure 13: Estimated stability limits for different jet lengths. $L = 10$ (solid line), $L = 15$ (dashed line) and $L = 20$ (dashdotted line).

understanding of microstructure evolution during commercial processing conditions is critical for optimization and control of semi-solid processing.

- In this study, various semi-solid billets including MHD, GR (by addition of Ti-B or Si-B alloys), SIMA, new MIT and UBE processed materials were evaluated. Processing conditions investigated include different processing temperatures during continuous heating, as well as isothermal holding for different time at commercial forming temperatures.
- Image analysis was carried out to quantify the semi-solid microstructure. Three important characteristic parameters--shape factor, particle size of Alpha particles, as well as the amount of entrapped liquid within the Alpha phase were measured in this study.

ACHIEVEMENTS THIS QUARTER

During this quarter, extensive image analysis was carried out to quantify microstructure evolution of various semi-solid billets manufactured by MHD, GR (by addition of Ti-B or Si-B alloys), SIMA, new MIT and UBE processes, respectively. Detailed results are given as follows.

1. The chemically grain refined billets have relatively high entrapped liquid content. During commercial forming conditions, the entrapped liquid content usually accounts for 15-30% of the total liquid phase for grain refined billets, and 8-15% for SIMA and MHD billets.

2. The formation of the entrapped liquid can be attributed to the coalescence of the broken dendrite arms upon reheating. SEM analysis reveals that there are two types of entrapped liquid in nature. One is entrapped in isolation within the Alpha phase, and the other is entrapped in 2D but is connected to the intergranular eutectic in 3D. Specifically, we found that the isolated entrapped liquid consists of extremely fine eutectic grains (in order of several micrometers), and a lot of small oxide spheroids have been identified as the nuclei for the fine eutectic grains.

3. Higher processing temperature tends to decrease shape factor value and entrapped liquid content, however, it also increases the Alpha particle size and the runoff of liquid phase during semi-solid forming. A favorite temperature range for aluminum semi-solid billets is between 580-590°C. For grain refined billets, 585-590°C is recommended.

4. Isothermal holding leads to a speroidization and a coarsening process of Alpha particles. Analysis on quantitative data points out that an optimum

isothermal holding time is between 2-8 minutes. For grain refined billets, the upper limit is recommended.

5. Specifically, both processing temperature and isothermal holding have a significant influence on the entrapped liquid content of GR billets. Increasing processing temperature or isothermal holding time decreases entrapped liquid content of GR billets considerably. However, processing temperature and isothermal holding time show little effect on the entrapped liquid content of SIMA and MHD billets.

Appendix A is a detailed report on the quantitative microstructural characterization of various semi-solid billets.

CHANGES IN PROJECT STATEMENTS

None

WORK PLANNED FOR NEXT QUARTER

This project is completed.

Appendix A

QUANTITATIVE MICROSTRUCTURE CHARACTERIZATION OF COMMERCIAL SEMI-SOLID ALUMINUM ALLOYS

PR-01-#2

Qingyue Pan, and Diran Apelian,

Advanced Casting Research Center (ACRC)
Metal Processing Institute
WPI, Worcester, MA 01609

The rheological properties of semi-solid metal slurries are strongly dependent on their microstructure. Specifically, our previous studies identified that three characteristic microstructural parameters are critical in determining rheological behavior of aluminum semi-solid slurries. They are

1. Particle size of the Alpha phase,
2. Shape factor of the Alpha particles, and
3. Entrapped liquid content within the Alpha particles.

Using the MPI image analyzer, we quantified microstructual evolution of various semi-solid billets during commercial forming conditions. In report PR-01-#1, we presented our results on A356 billets manufactured by both MHD and GR processes. This report presents our recent results on new MIT, SIMA (strain-induced melt activation), SiBloy (grain refined by addition of Si-B alloys) and UBE materials. Specifically, we compared the quantitative data of all these materials during commercial processing conditions, including continuous heating and isothermal holding at a commercial forming temperature. Therefore, this report provides a comprehensive knowledge base in understanding the effect of processing conditions and material genealogy on the microstructure evolution and rheological properties of various semi-solid metal slurries.

1. EXPERIMENTAL

1.1 Materials

The semi-solid billets evaluated include MHD, GR (by addition of Ti-B or Si-B alloys), SIMA, new MIT, as well as UBE processed materials. Table 1 lists alloy designations and composition. Sliced samples with approximately 0.25-inch